A mathematical exploration of principles of collective cell migration and self-organisation

Linus J. Schumacher

Worcester College

University of Oxford

A thesis submitted for the degree of

Doctor of Philosophy

Trinity 2015

Acknowledgements

I am grateful to my supervisors Ruth Baker, Philip Maini and David Kay for all their support, their confidence in me, and their patience. You provided an intellectual home to someone who was, as is the curse of the interdisciplinary scientist, feeling somewhat homeless.

This thesis would have become an entirely different beast had I not had the pleasure of working with experimental collaborators. Many thanks to the members of the Kulesa Lab at the Stowers Institute for Medical Research in Kansas City and the Chuong Lab at the University of Southern California for their generous hospitality during my visits, and for taking the leap to work with us theorists. Thank you especially to Paul Kulesa, Rebecca McLennan, and Jason Morrison, as well as Cheng-Ming Chuong and Mingxing "Mason" Lei for enduring my repeated questions about biology and attempts at explaining my mathematics.

I would like to acknowledge useful discussions with Louise Dyson (whom I also want to thank for access to her code) for the work in Chapter 3; Michael Bentley, Fred Hoffman, Victoria Hore, Allon Klein, and Ben MacArthur for the work in Chapter 4; members of the developmental biology discussion group, Alex Fletcher, and Christoph Weber for the work in Chapter 5; Maria Bruna and Jochen Kursawe for the work in Chapter 6; and Thomas Woolley for what could have been Chapter 0. I would further like to acknowledge the UK Engineering and Physical Sciences Research Council for funding through a studentship at the Life Science Interface Doctoral Training Centre, Worcester College for a Martin Senior scholarship and a lectureship in applied mathematics, and Richard Earl for giving me the opportunity to teach.

Thank you to everyone at the DTC and the (W)CMB, my cohort, colleagues and the staff for making the DPhil experience more fun and manageable. A few people deserve special mention: members of the nerdy book club for extracurricular escapes; my office mates Aaron, Jackie, Jess, Jochen, and Paul for frequent tea breaks; Alex for mentorship at the pub; and Waldemar for helping my attempts to use the MI as a computing cluster, and for coming to the rescue when my computer broke down.

Last but not least, I want to thank my friends from Oxford and from home, and my parents for getting me this far, and for keeping me sane near the end.
So long, and thanks for all the fish.

Abstract

This thesis explores the role of collective cell migration and self-organisation in the development of the embryo and *in vitro* tissue formation through mathematical and computational approaches. We consider how population heterogeneity, microenvironmental signals and cell-cell interactions facilitate cells to collectively organise and navigate, with the aim to work towards uncovering general rules and principles, rather than delving into the microscopic molecular details. To ensure the biological relevance of our results, we collaborate closely with experimental biologists working on two model systems.

First, to understand how neural crest cells obtain directionality, maintain persistence and specialise during their migration, we use computational simulations in parallel with imaging of chick embryos under genetic and surgical perturbations. We show how only a few cells adopting a leader state that enables them to read out chemical signals can lead a population of cells in a follower state over long distances in the embryo. Furthermore, we devise and test an improved mechanism of how cells dynamically switch between leader and follower states in the presence of a chemoattractant gradient. Our computational work guides the choice of new experiments, aids in their interpretation and probes hypotheses in ways the experiments can not.

Secondly, to study the self-organisation of mouse skin cells *in vitro*, we draw on aggregation processes and scaling theory. Dermal and epidermal cells, after being dissociated and mixed, can reconstitute functional (transplantable and hair-growing) skin in culture. Using kinetic aggregation models and scaling analysis we show that the initial clustering of epidermal cells can be described by Smoluchowski coagulation, consistent with the dynamics of the "clustering clusters" universality class. Then, we investigate a potential mechanism for the size-regulation of cell aggregates during the later stages of the skin reconstitution process. Our analysis shows the extent to which this tissue formation follows a single physical process and when the transition to different dynamics occurs, which may be triggered by cellular biochemical changes.

Contents

List of Figures

Chapter 1

Introduction and overview

This thesis was born out of the motivation for doing mathematical biology with results that biologists will care about. To achieve this, it focusses on close collaboration with developmental biologists on specific experiments. In developmental biology, difficult experiments and traditionally qualitative data present an opportunity for modelling on the one hand, while on the other hand increasingly quantitative measurements at multiple spatiotemporal scales create a need for careful data analysis and comparison with theory. The success of dedicated models can guide the search for overarching theories by identifying common principles that have proven relevant in focussed applications. In this spirit, we thus explore three particular themes in the realm of collective cell behaviour, where many cells interact to form emergent patterns and coordinate movement within the constraints of the microenvironment. These themes are population heterogeneity, microenvironmental signals and cell-cell interactions. We generally take a phenomenological approach, considering rules of behaviour and decision making at the cellular level, without including all known microscopic details necessarily. Rather, we aim for minimal models to explain the experimentally observed global behaviour of cell populations as a whole, which can constrain and guide the search for molecular mechanisms.

1.1 Themes of collective behaviour

From the statistical mechanics of gases to agent based models of swarming animals and tissue morphogenesis, there are a great number of ways of studying collective behaviour, with different approaches being suitable to different questions and applications. Rather than entirely committing to expertise in a particular branch of mathematical modelling, this thesis takes a problem-driven approach, meaning we

are interested in certain scientific questions, and use whichever techniques are determined appropriate for the particular problem under consideration.

1.1.1 Population heterogeneity

A key question at the interface of the physical and biological sciences is the role of population heterogeneity in collective behaviour. In fluids and gases, emergent phenomena arise in ensembles of identical particles. In populations of cells and organisms, however, differences from one agent to the next can be common, raising the question of the functional role of such heterogeneity. Presumably, many of the details found can be ignored for most questions, but which details are important will differ on a case by case basis. We explore this theme in Chapter 3.

1.1.2 Cell-environment interactions

In our understanding of cell movement and tissue morphogenesis, microenvironmental signals, that is, chemical, mechanical and electrical signals around the cells, play an important role to determine cell position and identity. The complexity of the multicellular structures observed in biology requires a selective readout in which different cells respond differently to such signals depending on their type, position and dynamics of exposure. In turn, the aforementioned heterogeneities in cell populations, if they are not inherited, will be determined through cell-environment interactions. An example of chemical signals guiding cells as well as inducing changes in their state is featured in Chapter 4.

1.1.3 Cell-cell interactions

In the field of statistical mechanics, different kinds of interactions between agents determine the classes of emergent collective behaviour. This motivates the use of minimal models to reproduce the collective phenomena we observe in nature. These minimal models can then constrain our choice of how much detail and which interactions to include in our mechanistic descriptions. In this spirit we may wonder, what simple interactions between cells are necessary, minimally, for the tissue structure found in complex organisms? Of course, the set of minimal ingredients may be time-dependent, as cells can actively change their interactions in response to perturbations and signals, in turn directing their path through tissue phase space. This we explore in Chapters 5 and 6.

1.2 Focussed experimental applications

Working closely with developmental biologists, we aim to not only contribute to the understanding of a specific biological problem at hand, but also treat these as case studies for the broader theoretical questions that are of interest to us in the long run. This in itself is a model of a fruitful scientific collaboration, in which we work from biological observations, construct models, make predictions, test these experimentally or perform experiments suggested by our models, refine the models based on the experiments, and repeat. Each of these cycles may take anything from months to years, and it is important to acknowledge that different experimental systems are suitable for different studies, hence we do not restrict ourselves to just one fiefdom of biology in this thesis.

1.2.1 Chick cranial neural crest cell migration

The neural crest are a population of cells that migrate over long distances in the vertebrate embryo. As multipotent cells they develop into a wide variety of tissues, such as nerves, muscle and bone. Figuring out the rules of neural crest migration holds the promise for understanding the evolution of vertebrates, treating developmental defects and controlling cancer metastasis. We provide more biological background to this fascinating system in Chapter 2, then analyse leadership in neural crest collective migration, and how this leadership is established in Chapters 3 and 4, respectively.

1.2.2 Mouse skin cell reconstitution

Functional, hair-growing skin can spontaneously form in culture from dissociated skin cells taken from newborn mice. This is a fascinating display of morphogenesis to understand in its own right, but by treating this as a perturbation away from and return to the equilibrium of a fully formed tissue, we can also hope to unravel important principles of homeostasis, development and regeneration. We contribute our piece to this larger endeavour in Chapters 5 and 6.

1.3 Aims of this thesis

There are three aims of this thesis: first, to explore the themes of collective cell migration and self-organisation laid out above in suitable model systems; second, to

contribute to the understanding of the focussed biological applications in a meaningful way; and third, to showcase the successes (and highlight the limitations) of an integrated experimental and theoretical approach in the study of biological systems.

Chapter 2

The neural crest as a model system to study collective cell behaviour

"It's like the cells doing the conga."
Philip Maini, (05.11.2012)

In this chapter we introduce the reader to the biological background of collective cell migration in general, and that of neural crest cells in particular, arguing the case that the neural crest is a fascinating system to study questions of collective cell behaviour. We review computational approaches to study these phenomena, both to provide an overview of the field and to survey approaches found in the literature upon which to build our own efforts.

In the study of collective migration, a remarkable example of long distance, coordinated directed migration of eukaryotic cells is found in the neural crest. The neural crest is a highly migratory and pluripotent cell population that contributes to the formation of many tissues in craniates (hagfish, lampreys and jawed vertebrates) (Hall, 2000). Cells from the neural crest differentiate into a variety of tissue types, such as bone, smooth muscle, pigment and nerve cells, to name but a few. During migration, the neural crest displays rich and dynamic heterogeneities at the level of morphology and gene expression. Neural crest cells originate as part of the neural tube (which goes on to form the spinal cord and brain), from which they delaminate and migrate in separate groups to distribute amongst a diverse array of destinations in the growing embryo. The neural crest thus derives from the ectoderm, though its characteristics are so unique and its role in vertebrate development so important, that it has been dubbed the "fourth germ layer" (Hall, 2000).

The outline of this chapter is as follows: In Section 2.1, we first introduce the reader to the biology of the neural crest model system and place it in the wider con-

text of cell migration in developmental biology in general. We discuss mechanistic hypotheses in the field of neural crest research on how cells obtain and process directional information to navigate to the right places in the embryo. Then, we review several computational frameworks that have been used to model neural crest cell migration, or may be suitable for this purpose, in Section 2.2. We weigh their relative merits for studying our particular research questions, and explain why we have chosen to extend the computational model from McLennan *et al.* (2012).

2.1 Biological background

Why do cells migrate? Cell migration facilitates targeted bulk movement of cells and thus plays a key role in the development and self-repair of multicellular organisms (Haeger *et al.*, 2015). Severe consequences can arise when cell migration is mis-targeted, as in developmental defects, or unregulated, as in metastatic cancer. There are a variety of forms of cell migration and different definitions depending on the field. In this section we provide the mathematically inclined reader with the necessary biological background, focusing on the neural crest as a prominent example, putting this into context in the field of collective cell migration more generally, and highlighting specific details relevant to the work in the following chapters.

2.1.1 Neural crest

Neural crest cells are an important migratory population of cells in vertebrate embryonal development. They emerge and migrate away from the neural tube, a dorsal strip of tissue which develops into the brain and spinal cord. As multipotent cells, neural crest cells contribute to a variety of tissues in different parts of the body, such as the peripheral nervous system, structures in the head, and heart, among many others (Kulesa *et al.*, 2004, 2010). We focus on cranial neural crest cells (in the head), but occasionally compare and contrast the characteristics or mechanisms of migration to other neural crest cell populations, such as those in the gut and trunk.

Let us focus our subject of application even further. Cranial neural crest cells migrate in distinct streams from the segments of the neural tube, called rhombomeres, towards the branchial arches, otherwise also known as pharyngeal arches (Kulesa *et al.*, 2004, 2010). For a schematic illustration and representative microscopy images see Fig. 2.1. For the purposes of our cell migration studies, we are mostly concerned with the migration of cranial neural crest cells from the fourth rhombomere (r4) to

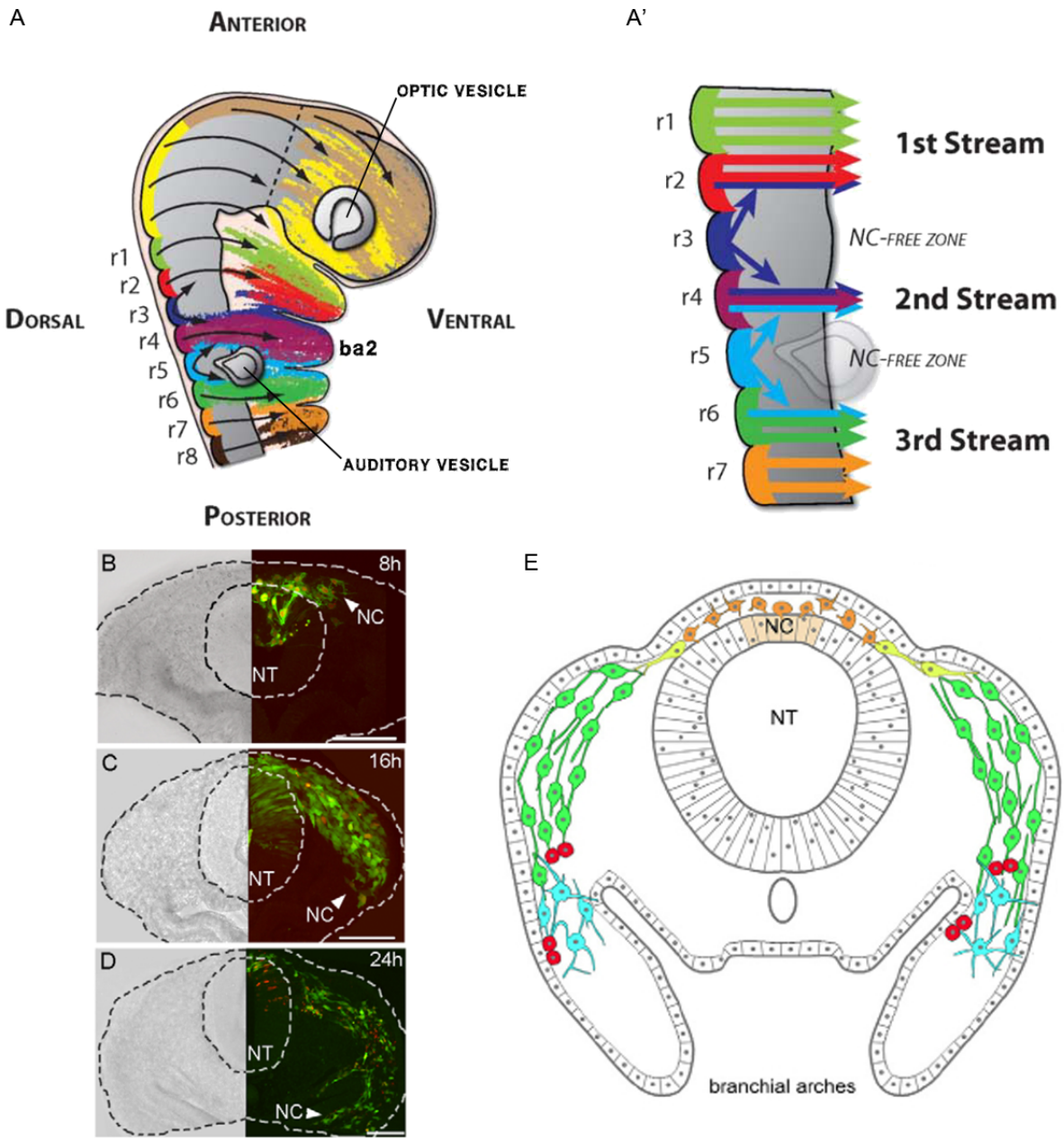

Figure 2.1: (A, A') Schematic of cranial neural crest cell migration from rhombomeres r1-8 to the branchial arches (ba) in distinct streams. Arrows indicate direction of migration and colour represents rhombomere origin of cells. We focus on migration from r4 to ba2. Adapted from Theveneau and Mayor (2011) (with permission from John Wiley and Sons). (B-D) Typical projected confocal images of transverse sections through a chick neural crest (NC) cell migratory stream at 8 (B), 16 (C) and 24 (D) hours after electroporation (migration from the neural tube (NT) starts approximately six hours after electroporation). Scale bars: 100μm. Adapted from McLennan *et al.* (2012) (with permission from the Company of Biologists). (E) Cross-sectional schematic of chick cranial neural crest migration at approximately $t = 24$ hours. Adapted from Kulesa *et al.* (2010) (with permission from Elsevier).

the second branchial arch (ba2) in the chick embryo at developmental stages HH 9 to 15 (Hamburger and Hamilton, 1951). The trajectory of migration lies along and underneath the outside tissue layer, the ectoderm. The cells are in a loose arrangement, with frequent contact through filopodial extensions but non-constant neighbour-relationships (Teddy and Kulesa, 2004). It is important to note that the characteristics of migration differ between neural crest cells in different parts[1] of the chick embryo and also between cranial neural crests in different organisms[2]. Whether there are universal mechanisms underlying this variety is subject to ongoing debate, and unified theories of neural crest migration across organisms remains the subject of future work.

2.1.1.1 Motivation: Developmental defects and cancer

By studying neural crest development, we can learn more about the mechanistic causes of developmental defects and hope to be able to repair these defects eventually. Diseases associated with defects in neural crest cell migration are known as neurocristopathies (Benish, 1975). These arise when neural crest cells fail to migrate to their target tissues or fail to colonise their migratory path, and thus fail to proliferate, or differentiate abnormally. Neurocristopathic malformations include cleft lip, unusual pigmentation, and abnormal ear development (Theveneau and Mayor, 2011) as well as conditions such as Hirschsprung's disease, which is a lack of nerves in part of the gut (Landman *et al.*, 2011). Understanding the mechanisms of neural crest cell motility and guidance, and the factors crucial to successful migration, can thus aid in developing preventative and restorative treatments of neurocristopathies.

The neural crest also provides a potential model system to study cancer metastasis. The neural crest lineage is the origin of the cancers melanoma and neuroblastoma, and their metastatic invasion bears many of the migratory characteristics of embryonic neural crest cells. When metastatic melanoma cells are transplanted into the neural crest microenvironment in the developing chick embryo, they do not form tumours, and some of the transplanted melanoma cells even migrate along the neural crest's path and into the target tissue (Kulesa *et al.*, 2006, Hendrix *et al.*, 2007). Thus, neural crest cell behaviour can not only shed light on the migratory characteristics of the metastatic phenotype of cancer cells, but also the mechanisms underlying its

[1]For example in the trunk, migration is more chain-like (Landman *et al.*, 2011, Wynn *et al.*, 2012).

[2]In *Xenopus*, for example, migration of cranial neural crest cells is more sheet-like (Theveneau *et al.*, 2010, Theveneau and Mayor, 2011).

plasticity, as controlled by the embryonic microenvironment. Understanding these mechanisms holds the potential to develop strategies to revert the metastatic phenotype and reprogram cancer cells (Hendrix *et al.*, 2007, Kasemeier-Kulesa *et al.*, 2008).

2.1.1.2 The spectrum of collective cell migration

Eukaryotic cell migration involves active motion associated with drastic cell shape changes such as protrusion of filopodia. One can distinguish between amoeboid[3], mesenchymal[4] and epithelial[5] cell migration, which differ in their cell density and amount of intercellular contact, as well as in the use of cell adhesion molecules (CAMs) and proteases. There is, however, plasticity between these modes of migration and it is not uncommon for cells to transition between modes during their migration, as, for example, in the epithelial-mesenchymal transition (EMT). For more details, see Friedl (2004) and references therein. Here, we are not concerned with the intracellular causes of cell motility, but the different modes of migration provide important context for the guidance mechanisms that we discuss in Section 2.1.2.

Collective motion of cells is characterised by a display of coordination of movement at the tissue scale. This global organisation often emerges from local interactions at the level of individual cells. Compared to the collective behaviour of groups of animals (Vicsek and Zafeiris, 2012), the self-organisation of eukaryotic cells is restricted to a more limited variety of sensory modalities at a smaller spatial scale. Despite this, collective cell migration manages to facilitate the development, maintenance and repair of whole organisms. In particular, the collective migration of cells during the development of the embryo enables rearrangement of tissue-level organisation even at late stages of development through the targeted placement of specialised cells that were specified in bulk elsewhere. Thus, the study of collective cell migration promises to provide one of the keys to understand the vastly different morphologies observed between closely related vertebrate species.

[3]Amoeboid cell migration of individual cells is associated with irregular, fast shape changes and weak substrate interactions (Friedl, 2004).

[4]The mesenchyme is a type of connective tissue derived from the mesoderm, the middle layer of cells in the early embryo. Mesenchymal cell migration is characterised by loose cell connectivity and generally takes place in three-dimensional substrate, and cells interact with, and potentially modify, the ECM (Friedl, 2004).

[5]An epithelium is a type of tissue that is found on the surfaces (internal and external) of animal bodies. Epithelial cell migration is sheet-like, featuring close cell-cell contacts, and therefore more two-dimensional in its dynamics (Friedl, 2004).

To situate the subject of our study, cranial neural crest migration, on the spectrum of collective cell migration, we need to make a terminological clarification regarding the term *collective cell migration*. Classifications of collective cell migration in the literature (Friedl, 2004) have typically focused on the movement of confluent sheets, persistent chains, and cohesive spheroids. Some migratory groups of cells, for example chick cranial neural crest cells (McLennan *et al.*, 2012), are made up of individuals that autonomously control their motility, yet nevertheless rely on cell-cell contacts for group navigation. This type of migration has been termed *loose* (as opposed to cohesive) collective cell migration (Rørth, 2012) as well as *multicellular streaming* (Friedl *et al.*, 2012). Here, we define this type of less cohesive cell migration as follows:

- Cells autonomously control their cytoskeleta, but their movement is aligned with that of the rest of the population.
- The cells do not move in a cohesive, densely packed group, as they may do in, for example, zebrafish lateral line primordium (Streichan *et al.*, 2011), zebrafish prechordal plate (Dumortier *et al.*, 2012) or *Xenopus* neural crest (Theveneau *et al.*, 2010).
- The cells *can* migrate individually, and may even do so in a directed manner (at least according to our working hypothesis, even if not observed *in vivo*). However, migration in large groups may confer additional advantages (in terms of robustness or efficiency) or arise out of constraints.

It makes sense to consider a wider definition of collective migration that includes the above described phenomenon. As shown by previous work (McLennan *et al.*, 2012), cell-cell interactions are likely to be crucial to the successful migration of chick cranial neural crest cells and their distribution along the migratory path, enabling a large number of cells to migrate together, or potentially making their migration more efficient. We, and others (Rørth, 2012), argue that multicellular streaming can be considered *collective* in the wider sense of collective behaviour of individual agents, as studied in many other systems (Vicsek and Zafeiris, 2012), and should therefore be included in the definition of collective cell migration. The term "multicellular streaming" (Friedl *et al.*, 2012) has the advantage of making a distinction from cohesive collective migration, but the disadvantage of not consistently being classified as collective migration in the literature. Owing to its popularity, we nevertheless adopt this name here. As we will see in Section 2.1.2, the neural crest serves as a model

system particularly to study loose cell migration as well as cell heterogeneity and migratory plasticity, and is thus more generally useful for advancing our understanding of the spectrum of collective cell migration.

2.1.2 Guidance mechanisms

A central question of collective cell migration in developmental biology is how cells navigate through the embryo and what guides them to their target sites. For this there exist several current hypotheses in the field of neural crest cell migration. In a recent review, Kulesa and McLennan (2015) classify important mechanistic aspects of neural crest migration into three themes: (a) persistence and linearity, (b) cohesion and (c) plasticity and heterogeneity. These overlap with our themes of population heterogeneity, cell-environment interactions and cell-cell interactions described in Chapter 1. Whereas the themes of Kulesa and McLennan (2015) classify the biological phenomena to be understood, our themes explore the mechanisms that could give rise to these phenomena. The difference is in perspective (top-down vs bottom-up), but they are complementary approaches.

To outline our review, we roughly follow the break-down of Kulesa and McLennan (2015), who, for the phenomenon of persistence and linearity, discuss three mechanisms, or models (in the conceptual sense): frontal expansion; co-attraction with contact inhibition of locomotion; and the cell-induced gradient model. We introduce these in opposite order, starting with the most relevant for the work in this thesis, so that the busy reader may skip the others (and enjoy reading about them another time).

2.1.2.1 Cell-induced gradient hypothesis

Perhaps the most simple and well-studied guidance mechanism of cell migration is chemotaxis up or down a gradient of an attractive or repulsive cue. In bacterial chemotaxis, for example, this cue might be provided by the naturally occurring distribution of food or toxins. In the development of complex eukaryotic organisms, gradients of chemicals known as morphogens are thought to direct growth, movement and differentiation (for a review, see Rogers and Schier, 2011). Pre-existing morphogen gradients for migration require a mechanism to explain how they are established, and many such mechanisms are known or hypothesised (Müller *et al.*, 2013). An alternative concept is the dynamic interpretation and generation of gradient signals.

In the absence of a pre-established gradient of chemoattractant to guide migration, e.g. if a uniformly distributed cue is observed, an alternative guidance mechanism is provided by the cell-induced (or self-generated) gradient hypothesis (Kulesa *et al.*, 2010, Streichan *et al.*, 2011, McLennan *et al.*, 2012). Here, cells bind and internalise, or otherwise inactivate, the attractive cue. Through this local consumption of chemoattractant, a gradient is created that the cells can follow. If the induced gradient is locally symmetric around a cell, breaking of the symmetry is required to initiate migration. Conceptually, the cell-induced gradient hypothesis is similar to models of cellular aggregation through self-secreted chemoattractants, dating back to Keller and Segel (1970a,b), who first proposed a mathematical mechanism to explain aggregation of slime mould amoebae.

The symmetry in the local chemoattractant gradient can be broken in a number of ways, for example by the initial velocity of the cells (creating a steeper effective gradient in the direction of movement), as is thought to be the case in the zebrafish lateral line primordium (Streichan *et al.*, 2011). Alternatively, as in the case of cranial neural crest cells (Kulesa *et al.*, 2010, McLennan *et al.*, 2012), cells enter on one side of the migratory domain (and do so for the entire process of migration), while consuming chemoattractant faster than it is being produced, so that the chemoattractant concentration is not re-established behind the leading front of cells. In cancer spreading, local gradients created by melanoma cells have been suggested to drive their chemotactic dispersal (Muinonen-Martin *et al.*, 2014).

The cell-induced gradient hypotheses may be invalid in cases where chemoattractant diffusion is fast enough (or chemoattractant consumption low enough) to flatten out the chemoattractant profile before cells can sense and respond to a local gradient. However, modelling efforts and experimental results presented here and elsewhere (Streichan *et al.*, 2011, McLennan *et al.*, 2012) suggest that this is not the case in the biological settings studied. Another alternative to chemotaxis up pre-existing chemoattractant gradients is starvation-driven dispersal, in which cells move randomly but increase their speed when a relevant chemical resource is low. Models of starvation-driven dispersal (Yoon and Kim, 2015) have been shown to give similar results to classic models of chemotaxis (Keller and Segel, 1971a,b). Here, we do not consider this alternative hypothesis, as in chick neural crest cells the differences in cell speeds are not as large as would be required by the starvation-driven dispersal mechanism (Kulesa *et al.*, 2008).

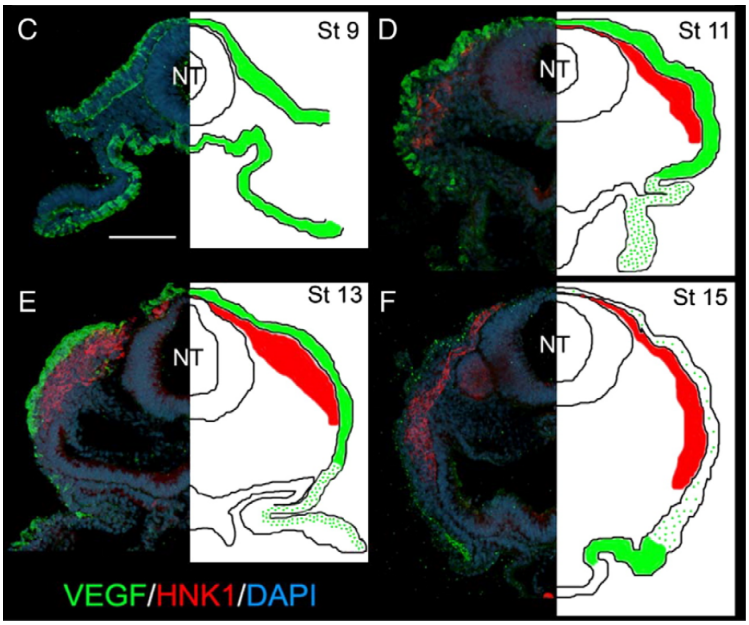

Figure 2.2: Sections of a developing chick embryo and corresponding schematics showing migration of neural crest cells from the neural tube (NT) and expression of neural crest chemoattractant VEGF in the ectoderm at various developmental stages (St). Labelled for VEGF, neural crest cells (HNK1) and DNA (DAPI) (staining cell nuclei). Reproduced from McLennan *et al.* (2010) (with permission from Elsevier).

Evidence for cell-induced gradients of VEGF in the chick embryo

For the remainder of this subsection, we present specific evidence to make the case for the cell-induced gradient model in the chick cranial neural crest. First and foremost, cranial neural crest cells are known to be attracted to Vascular Endothelial Growth Factor (VEGF, more specifically, VEGF-A) *in vitro* and *in vivo*, and VEGF is expressed in the ectoderm of ba2 (McLennan *et al.*, 2010). The expression, i.e., production, of VEGF has been observed to be spatially uniform in the tissue up to the entrance of ba2, and there does not seem to be a pre-existing gradient of growth factor prior to cranial neural crest cell migration (Fig. 2.2). There is emerging evidence that cell-induced migration is also employed by cardiac neural crest cells, where the role of VEGF is instead played by Stromal Cell-Derived Factor 1 (SDF1) (Kulesa and McLennan, 2015).

Evidence for the internalisation of VEGF, which drives the formation of the cell-induced gradient, at the molecular scale comes from biochemical studies. The isoform VEGF-A^{165} interacts with the receptors VEGF receptor 2 (VEGFR2) and Neuropilin-1 (NRP1) (Simons, 2012). NRP1 can act as a co-receptor to VEGFR2, with which it internalises rapidly upon the binding of VEGF (Koch *et al.*, 2014). However,

there is also evidence that NRP1 can bind VEGF independent of VEGFR2, such as in certain cases of axon guidance (Eichmann and Simons, 2012). Thus, NRP1 has been hypothesised to indirectly regulate VEGFR2 signalling through competition for ligands between cells that express both NRP1 and VEGFR2 and cells that only express NRP1 (Koch *et al.*, 2014). The dynamics of the VEGF receptor, including its internalisation, have been studied in more detail using mathematical models related to angiogenesis[6] in cancer (Alarcón and Page, 2007, 2012).

It remains unclear to what extent VEGF diffuses through tissue *in vivo*. In vasculogenesis[7] studies, mathematical modelling suggests that soluble VEGF might be the determining factor for chemotaxis at short range, but has little impact on the overall concentration profile of VEGF. At longer range, ECM-bound VEGF might be the more important guidance factor, detected by filopodial extensions (Vempati *et al.*, 2011). Neither the extent to which VEGF can diffuse in the neural crest microenvironment, nor the distribution of different VEGF isoforms along the migratory path, are known, as they are hard to visualise directly. Hence, it is unclear whether soluble or ECM-bound VEGF, or a combination of both, is guiding neural crest cells. Thus, our theoretical models should be robust to the extent of VEGF diffusion, and for the scope of this thesis we ignore different isoforms.

2.1.2.2 Cell heterogeneity and follow-the-leader migration

In many systems exhibiting collective cell migration, a degree of cell heterogeneity with "a clear division of labour" (Rørth, 2012) into leader and follower states can be observed: Leader cells read out directional information, from environmental signals, or otherwise, while follower cells instead obtain their directional cues from the leader cells, through secreted signals, mechanical sensing, direct pulling or tracks in the ECM, to name just a few possibilities. In principle, these differences between cells could be emerging from intercellular interactions, pre-specified or induced by signals in the tissue environment.

Evidence for leader-follower heterogeneity can be found, for example, in angiogenesis (tip and stalk cells), zebrafish lateral line primordium (Streichan *et al.*, 2011), *Drosophila* border cells (Inaki *et al.*, 2012) and neural crest cells (McLennan *et al.*, 2012). For more details, see Khalil and Friedl (2010), who discuss a range of leader cell morphologies and mechanisms of induction.

[6]The sprouting of new blood vessels from existing ones.
[7]The formation of entirely new blood vessels from precursor cells.

Why cell heterogeneity?

A physicist or mathematician may wonder: "Why do we need leader and follower cells? We know that collective behaviour can arise from identical agents, which is simpler." This is a valid concern. However, nature need not have found the "simplest" (most parsimonious) solution for every instance of collective cell migration, given the strongly path dependent nature of evolution. Furthermore, we need to address with our models the evidence that biologists present to us, and the literature clearly shows clues to functional population heterogeneity.

Still, the observed differences between cell properties and behaviour could be an artefact of finite size systems or a consequence of confinement. For example, Smadbeck and Stumpf (2015) have argued that proliferative "superstars" in front-driven neural crest cell migration necessarily arise through competitive growth in a confined environment. This line of thought would lead us to consider that cells are identical and the observed heterogeneity is really due to responses to local differences in the environment. In our view, this distinction is largely semantic, and the above perspective very much compatible, if not equivalent, with the models we present in Chapters 3 and 4, even if we only use the terms "leaders" and "followers" as useful descriptors.

2.1.2.3 Contact inhibition of locomotion and local attraction

A complementary mechanism to guidance through cell-induced gradients is the combination of contact inhibition of locomotion (CiL) and co-attraction (CoA, Carmona-Fontaine *et al.*, 2011). In this mechanism, group cohesion is provided by the balance of repulsion and attraction between cells. Specifically, repulsion upon contact promotes dispersal, while mutual cell-cell attraction balances the dispersion that would otherwise result from contact inhibition of locomotion alone. In more general terms, this mechanism can be thought of as an effective potential resulting in repulsion at short range, and attraction at intermediate ranges. Overall, it gives rise to the cohesive and potentially persistent but undirected collective motion of a group of actively moving particles or cells. Directionality of the overall migration could then be provided by confinement or directional signals, such as chemoattractant gradients.

Together, CiL and CoA have been suggested as a general mechanism for collective neural crest cell migration. Evidence for this has been found in *Xenopus* and zebrafish, where cranial neural crest cells acquire polarisation through inhibition of membrane protrusions at intercellular contact sites (via N-cadherin), in combination with promotion of protrusions (via Rac1) at free edges (Theveneau *et al.*, 2010). This

polarisation is thought to be stabilised and amplified through the chemokine SDF1, which, in the absence of intercellular contacts, may be insufficient to promote directional migration (Theveneau *et al.*, 2010, Theveneau and Mayor, 2011). In the *Xenopus* system, co-attraction is mediated by the peptide C3a, which is expressed by the neural crest cells (Carmona-Fontaine *et al.*, 2011).

While contact inhibition of locomotion paired with co-attraction creates a mechanism for group cohesion and, once directional symmetry is broken, alignment of motion between cells, it still requires an overall directional signal to enable long-range navigation in the embryo, such as a chemoattractant gradient. It is therefore not mutually exclusive with the cell-induced gradient model (Kulesa and McLennan, 2015). In the context of the cranial neural crest in *Xenopus*, Theveneau *et al.* (2013) propose a "chase-and-run" hypothesis, in which neural crest cells are attracted to placode cells by SDF1, and placode cells are repulsed on contact through planar cell polarity (PCP) and N-cadherin signalling. While this mechanism has yet to be tested further, it has not been investigated in chick, where studies have instead suggested that neural crest cells guide (rather than repel) neuron growth from placodes (Freter *et al.*, 2013), and where placode assembly is independent of interactions with the neural crest (Theveneau *et al.*, 2013).

Whether contact inhibition of locomotion is relevant in the collective migration of avian cranial neural crest remains unclear, as cells are in less close contact (multicellular streaming) and have furthermore been observed to move in the same direction as each other following contact (Teddy and Kulesa, 2004). Local attraction between cells through secreted factors may play a role, but the corresponding molecules have not yet been identified. Further differences in neural crest migratory mechanisms between different organisms are still being discovered. For example, PCP signalling, which is involved in contact inhibition of locomotion, is required for neural crest cell migration in *Xenopus* and zebrafish (Carmona-Fontaine *et al.*, 2008), but not in mice (Pryor *et al.*, 2014), at least for the class of PCP tested. While the prospect of universal guidance mechanisms of neural crest cells for all vertebrates is enticing, we must acknowledge and appreciate the differences between biological model systems.

What is the difference between contact inhibition and volume exclusion? In the definition of CiL, we can consider a spectrum from repulsive to (volume) excluding interactions. Repulsive CiL implies adopting a direction of movement away from the point of contact with another cell, while excluding CiL simply biases the

movement toward any space unoccupied by other cells. In the case where the direction of movement after a cell-cell encounter is chosen uniformly from the unoccupied space, excluding CiL may become indistinguishable (at the population scale) from the physical phenomenon of volume exclusion (even if mechanistically distinct). The importance of volume exclusion in cell migration has been studied in deriving continuum descriptions of moving cell populations (Dyson and Baker, 2015), including the different effects of particular types, or implementations, of volume exclusion (Dyson *et al.*, 2012).

The difference in outcome between repulsive CiL and volume exclusion has been studied in simulations of haemocyte dispersal (Davis *et al.*, 2012), where volume exclusion fails to produce the periodic patterning that results from dispersal through repulsive CiL. Similar computational experiments have not been carried out in models of neural crest cell directed migration. This presents a promising avenue for future work to generalise complementary descriptions of the process in different model organisms (such as chick, *Xenopus* and zebrafish), and to investigate whether we can even tell the difference between CiL and volume exclusion from current data on neural crest cell migration *in vivo*.

2.1.2.4 Front-driven migration

As an alternative mechanism to directed migration, colonisation of tissue by neural crest cells can also be driven through frontal expansion, i.e., increased division of cells at the free edge of the cell population. Thus, cells fill in the free space adjacent to the population not through directed motion, but preferential division. Together with spatial confinement, frontal expansion can provide a direction and thus facilitate invasive migration.

Evidence for front-driven migration is found, for example, in the mouse gut, where enteric[8] neural crest cells at the migrating front have higher proliferation rates than the rest of the population, which is thought to be due to the proximity of uninvaded tissue (Simpson *et al.*, 2007). This localised proliferation is hypothesised to be a major driving factor of migration in the absence of long-range directional cues, such as a chemoattractant gradient (Landman *et al.*, 2011).

Interestingly, Cheeseman *et al.* (2014) have found evidence for cell heterogeneity in experiments and simulations of front-driven neural crest migration in the form of more proliferative cells, dubbed "superstars". Smadbeck and Stumpf (2015), however,

[8]Relating to, or taking place in, the intestines.

have argued that one will necessarily discover overrepresented lineages in scenarios of competitive growth under confinement, raising the possibility that cell heterogeneity in this context is an artefact resulting from a selection processes on a population of identical dividing cells.

Although there is evidence for increased proliferation in the front portion of the migrating stream of chick cranial neural crest cells (Kulesa *et al.*, 2008), more recent evidence suggests that proliferation may not be relevant until cells reach their target site, the branchial arches (Ridenour *et al.*, 2014). We cannot rule out a contribution of proliferation to chick cranial neural crest cell migration, but we expect it to be a minor effect and so do not investigate it further in this thesis.

2.2 A review of computational frameworks for studying neural crest cell migration

In this section, we review existing computational frameworks that have been used to study cell migration and which might be suitable for some of the questions we aim to address in this thesis. To conduct model experiments computationally, we need a framework that can represent the key aspects of our current working hypothesis (a cell-induced gradient with leader and follower cell states): cell movement and sensing; a dynamic chemoattractant concentration profile; different cell states; cell-cell communication and tissue growth. These are key elements of our working hypothesis. Other aspects, such as mechanical interaction with the extracellular matrix (ECM), cannot be ruled out, but for now we focus on phenomena for which data are available *in vivo*.

Based on the relative merits of the existing computational frameworks, and on the extensions that would be necessary to make each one suitable to our needs, we choose to base our work on the framework used in McLennan *et al.* (2012). The other computational models reviewed may provide useful aspects to incorporate into a computational framework in future work and we point these out as we go along.

2.2.1 Models of follow-the-leader migration

McLennan *et al.* (2012) used a combination of computational and *in vivo* experiments to establish that chick cranial neural crest cell migration may be driven by chemosensitive leader cells and a larger group of followers, moving in a chain-like manner. This process is modelled as an off-lattice 2D position jump process on a growing domain.

The evolution of chemoattractant concentration is described by a reaction-diffusion equation (RDE) in which the cells act as Gaussian-shaped sinks and uniform tissue growth as a dilution term. Cells sense chemoattractant at the end of a single, long filopodium (thrust out in a randomly chosen direction) and compare it to the concentration at the centre of the cell body. Leader cells move in the chosen direction if the concentration is higher at the end of the filopodium and no other cells are in the way. In contrast to this, follower cells search randomly with their filopodia for another cell and move towards that cell if it is a leader or a follower connected (through any number of followers) to a leader. In this way, chains of migrating cells form (Fig. 2.3). Without this leader-follower behaviour, i.e. with leader cells only, migration is found to be unsuccessful (Fig. 2.3), as trailing cells get stuck in a region of depleted chemoattractant (for the values of chemoattractant diffusion and production used). For this proof-of-principle result, the contingent of leaders makes up the front 30% of the stream. Importantly, this model also demonstrated that random movement (at the speeds measured *in vivo*), is insufficiently fast for invasion of the tissue on the relevant timescales, as cells would not migrate very far, even on a growing domain.

In a different collaboration by some of the same authors, enteric neural crest cell chain migration is simulated with an agent-based model on a square lattice (Wynn *et al.*, 2012). Different behaviours for leader and follower cells are taken into account, as is the creation of permissible paths in the ECM by leader cells (modelled as open and closed lattice sites). The authors explore the parameter sensitivity of chain stability. Directional cues are implemented through a directional bias, but this is found not to be sufficient to drive chain migration by itself. This work was extended to model stream (rather than chain) migration (Wynn *et al.*, 2013), to investigate, in comparison with tissue transplantation experiments, how cell contact dynamics and interactions with the ECM determine stream versus chain migration (Fig. 2.4). For example, a reduced ability to break down ECM was predicted to promote chain migration, which could be tested by loss of function, or by microinjection of collagen or fibronectin to increase ECM density. Another promoting factor of chain migration was found to be filopodial contact-induced attraction between cells, a notion that is confirmed by previous experiments that disrupt chain migration (Rupp and Kulesa, 2007). Unlike in the previous work on chain migration, a dedicated sensitivity measure was not used, and such a metric for stream migration in on-lattice models is yet to be developed.

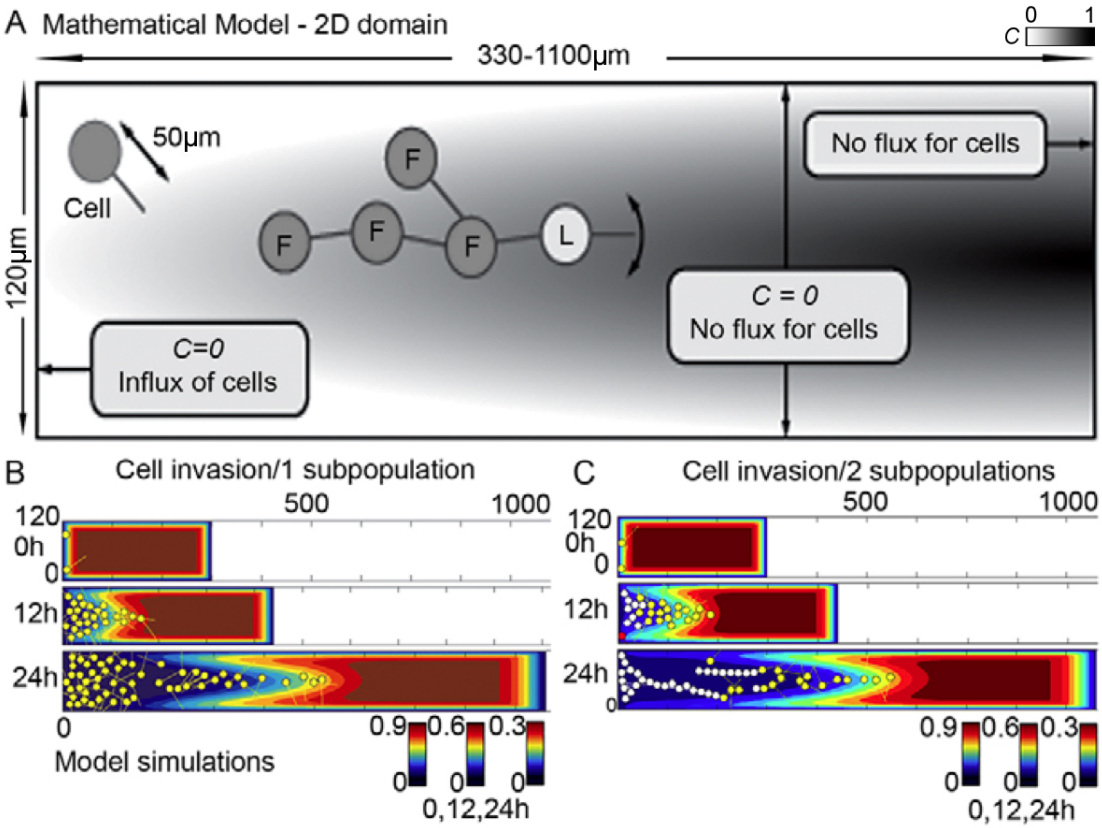

Figure 2.3: Previous computational model of neural crest cell migration. A: Schematic showing domain geometry, cells and chemoattractant boundary conditions. B: Realisation with all cells as leaders (yellow). C: Realisation with leaders and followers (white). Grayscale and colourbars show chemoattractant concentration. Reproduced from McLennan *et al.* (2012) (with permission from the Company of Biologists).

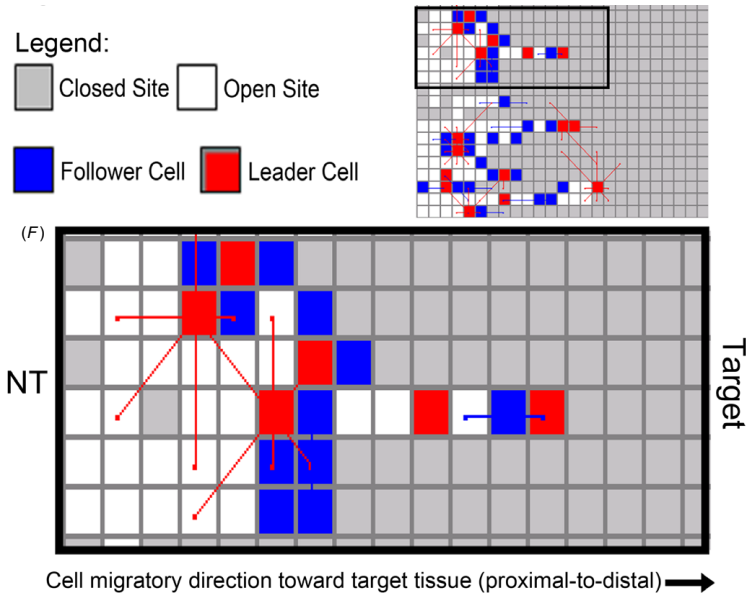

Figure 2.4: Previous lattice-based model of neural crest cell migration. Reproduced from Wynn *et al.* (2013) (with permission from IOP Publishing).

2.2.2 Models of cell-induced gradients

In addition to the aforementioned work by McLennan *et al.* (2012), a number of other mathematical approaches to study cell-induced gradient migration have been developed. Séguis *et al.* (2012) take a mathematically sophisticated approach to modelling the chemotaxis of finite sized cells on a growing domain. The uptake of chemoattractant through the cell membrane and the resulting flux into and around the cells is modelled explicitly with an advection-reaction-diffusion equation, i.e., the cells sit within the attractant medium and boundary conditions are imposed on their membranes (Fig. 2.5). This computational framework models the diffusion of chemoattractant and its internalisation by cells more rigorously than the computational model in McLennan *et al.* (2012). Séguis *et al.* (2012) assumed that the actual cell shapes are fixed and elliptical, whereas in our application the cells have complex and dynamic shapes (which we approximate as Gaussian sinks in lieu of representing the dynamics of cell shape changes). Furthermore, explicitly representing chemoattractant displacement by cells seems more appropriate in a fully three-dimensional model. In a two-dimensional representation, we may want to keep the possibility of chemoattractant being "under" or "on top of" cells, i.e., in the same place. In addition, extending the computational advances of (Séguis *et al.*, 2012) for our needs would require substantial further methodological changes. We cannot currently motivate this effort, given the available data on chemoattractant distribution and diffusivity

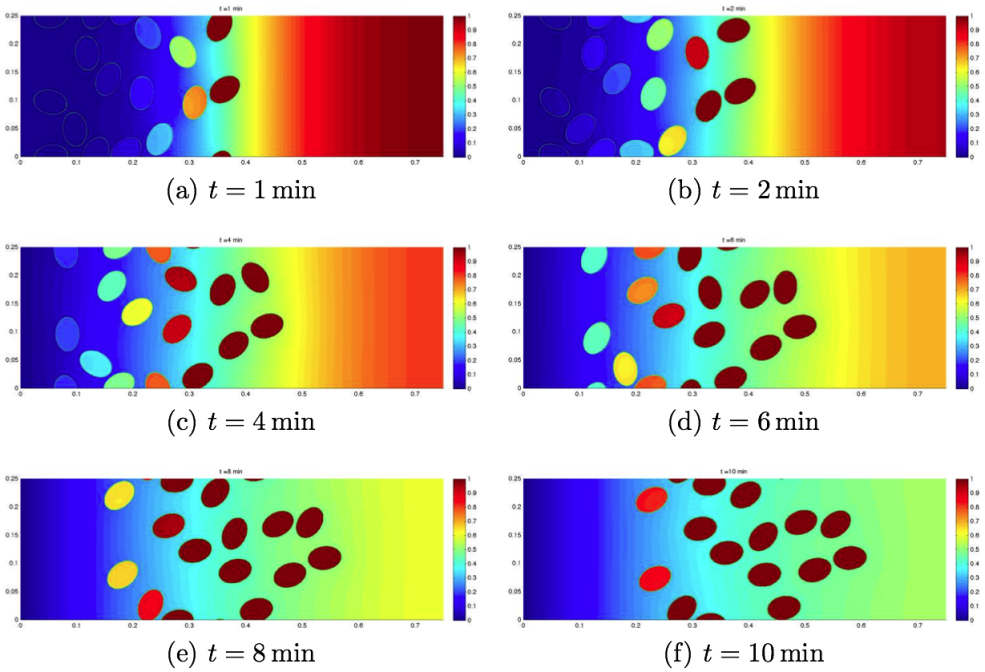

(a) $t = 1\,\text{min}$ (b) $t = 2\,\text{min}$

(c) $t = 4\,\text{min}$ (d) $t = 6\,\text{min}$

(e) $t = 8\,\text{min}$ (f) $t = 10\,\text{min}$

Figure 2.5: Simulation of chemotacting cells. Colour shows chemoattractant concentration outside cells, and total chemoattractant absorbed inside cells. Reproduced from Séguis *et al.* (2012) (publicly available online).

in relevant *in vivo* systems are scarce. As an alternative, we intend to verify that our models are robust, and not sensitive, to variations in the parameter values of chemoattractant diffusion and uptake. We only aim to capture the phenomenology of the cell-induced gradients, and hence do not take the approach of accurately describing the displacement of chemoattractant by cells.

A well-established example of cell-induced gradient formation is found in the migration of the zebrafish lateral line primordium (Donà *et al.*, 2013). In an earlier study, the authors mathematically modelled the lateral line primordium as a rod-shaped cell collective actively moving along a one-dimensional line of chemoattractant (Streichan *et al.*, 2011). The chemoattractant concentration is described by a RDE, with degradation rates defined piecewise with respect to the position of the rod of cells, whose movement, in turn, depends on the gradient of chemoattractant. In an extension of the model, cell clusters are deposited behind the moving rod, which is compensated for by cell division. While this differential equation model is attractive for its analytical tractability, the representation of the cell collective as a continuous rod seems more suitable to the particular geometry and cell arrangement of their experimental application, and less so for questions concerning interactions between and mixing of

different subpopulations of neural crest cells, which are the focus of our study.

2.2.3 Models of contact inhibition of locomotion

Apart from the simulations of haemocyte dispersal (Davis *et al.*, 2012) mentioned earlier, the role of CiL has been explored in computational models of *Xenopus* neural crest cell migration. Woods *et al.* (2014) built a model to implement the CiL with CoA mechanism (Fig. 2.6), extending their earlier developments (Carmona-Fontaine *et al.*, 2011). A static chemoattractant profile from individual cell sources adds up to give higher attraction in the centre of a group of cells. Thus, the co-attraction mechanism implemented is not between cells in a pairwise manner, but between individual cells and the overall population. The authors conclude from their model that directed collective migration can arise from cell interactions without external directional signals, yet it seems this is a consequence of confinement through restrictive regions that are implemented as fixed repulsive gradients.

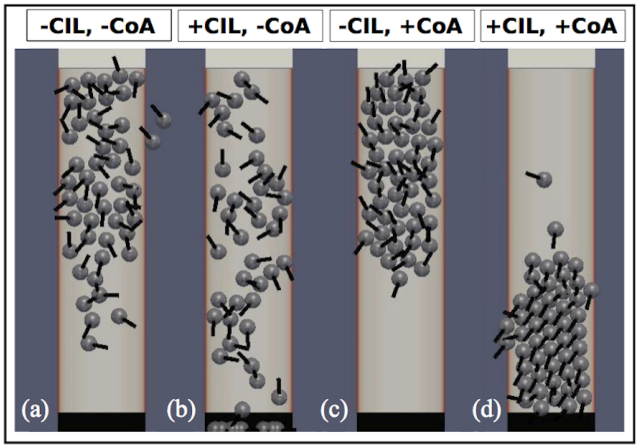

Figure 2.6: Computational model of *Xenopus* neural crest migration, showing (a) dispersal, (b) migration with CiL, (c) aggregation through CoA, and (d) cohesive migration with CiL and CoA. Reproduced from Woods *et al.* (2014) (Creative Commons Attribution License).

In the force-based model by Woods *et al.* (2014), cell interactions are modelled as rigid body collisions with an additional re-polarisation force. To resolve forces between cells on the timescale of membrane dynamics, the authors choose a time-step on the order of milliseconds and run the model on high performance computing facilities. For our purposes, the necessity for such a high temporal resolution is not evident: Cell contact has not been observed to mediate repulsion during cell encounters in chick (Teddy and Kulesa, 2004), and the mechanical parameters and rates needed to

implement a similar model are experimentally unknown. In light of this, we opt for a computationally less expensive approach, and choose to focus on scales that can be readily probed *in vivo*. Of course, it might turn out that a full mechanical model will, in the long run, indeed be necessary to fully describe neural crest migration, and it is valuable for us, as a research community, to create complementary simulation frameworks at different levels of spatiotemporal resolution.

2.2.4 Models of frontal expansion

A number of cellular automata studies have investigated neural crest invasion through proliferation. We already mentioned the work by Cheeseman *et al.* (2014) to identify proliferative "superstars". Previously, some of these authors also studied the interaction of enteric neural crest cells with growing axons (Landman *et al.*, 2011). On a 2D hexagonal lattice, the authors simulated the proliferative expansion of the neural crest population together with the growth of axons, to test whether axon growth follows the neural crest cells' migration or *vice versa*. The network structure of cells and axons resulting from the stochastic simulations is analysed to compare the two hypotheses. As this study addresses enteric neural crest cell migration via frontal expansion, it does not need to implement a directional cue. Tissue invasion happens in an undirected manner, driven by increased proliferation at the front. On-lattice models such as this may be inappropriate to model streaming migration and distinguish it from chain migration, which is an important difference in morphology between neural crest populations in different parts of the organism that is likely to be controlled by the microenvironment (Kulesa and Fraser, 1998, Wynn *et al.*, 2013).

In this chapter, we have introduced biological background on neural crest migration, discussed some of the existing hypotheses for guidance mechanisms of migratory neural crest cell populations, and argued that the neural crest is a suitable model system to study the spectrum of collective cell migration, since it exhibits a range of migratory morphologies and guidance mechanisms. We then reviewed a range of computational frameworks that have been used to study neural crest cell migration in several settings and under different hypotheses.

In Chapter 3 we will critique and extend the model by McLennan *et al.* (2012) to explore the question of which cells take on leading roles in cranial neural crest migration, how many cells do so, and why the number of leaders matters.

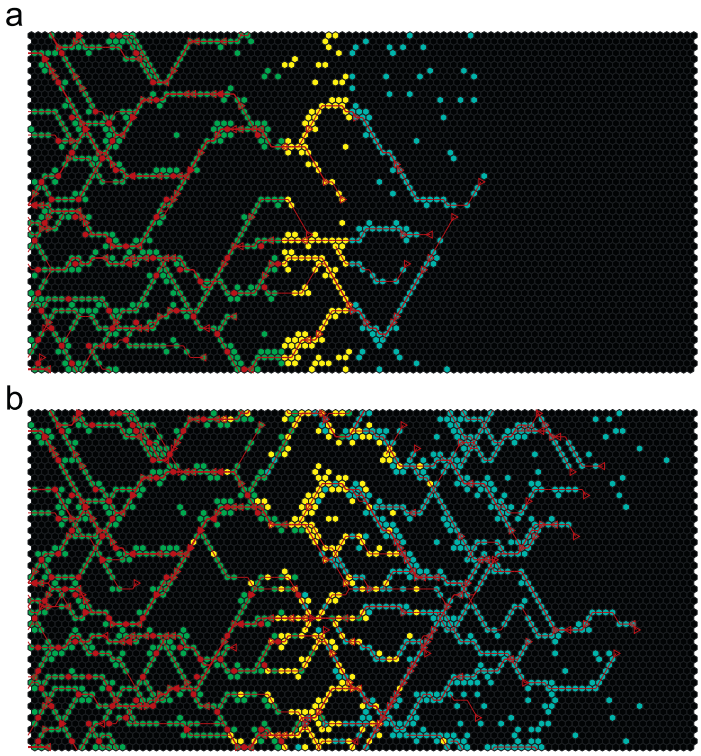

Figure 2.7: Computational model of enteric neural crest cells (green, yellow and blue lattice sites) and axon growth (red lattice sites), showing (a) an initially labelled population of cells and (b) colonisation outcome, driven by expansion of the frontal population. Reproduced from Landman *et al.* (2011) (with permission from Elsevier).

Chapter 3

Oligarchy in neural crest cell migration

In this chapter we explore the effects of population heterogeneity on the collective migration of cells. We choose the neural crest as a model system and focus on experiments in the chick cranial[1] neural crest, and on specific differences in cell characteristics that have clear implications for their migratory behaviour: leader and follower states. Given biological evidence for and computational proof-of-principle of leader and follower behaviour in the chick cranial neural crest, our aim is to determine what proportion of cells in a migrating population are in a leader state, what effect a change in the size of the leader fraction has, and what implications this may have for the efficiency and robustness of invasive migration.

To answer these questions, we use the model identified from our review in Chapter 2 (McLennan *et al.*, 2012) as most suitable and make necessary adjustments and extensions to it. Details of our model modifications and development are outlined in Section 3.1. In Section 3.2, we use our computational model in conjunction with *in vivo* experiments to show that chick cranial neural crest cells could be guided by just a few cells at the invasive frontlines of the population.

Within this chapter, we do not address the induction or dynamics of the heterogeneity, i.e., we ignore phenotypic plasticity and switching between leader and follower cell states for the time being, and will treat this in Chapter 4. Since we want to investigate the effect of changes in the proportion of cells that are in a leader state, we are required to be able to control (in our computational model) the cell state directly. Changing the number of cells in a leader state while phenotypic plasticity is enabled would require first an understanding of what determines the cell state and a

[1] *cranial*: Relating to, or, in this context, taking place in, the *cranium*, an anatomical term for the head of a vertebrate animal.

robust implementation of the switching mechanism, which we will address in Chapter 4. We will let our work in that chapter be guided by the results in this chapter. By identifying how many cells are leaders, we can hope to learn which aspects of the heterogeneity between neural crest cells may be attributed to a different navigational state, which then in turn may enable us to observe different cell states through their molecular profile and control cell state transitions.

Comment on originality Work in this chapter draws on the following publication by the author and collaborators:

R. McLennan*, L. J. Schumacher*, J. A. Morrison, J. M. Teddy, D. Ridenour, A. Box, C. Semerad, H. Li, W. McDowell, D. Kay, P. K. Maini, R. E. Baker and P. M. Kulesa. Neural crest migration is driven by a few trailblazer cells with a unique molecular signature narrowly confined to the invasive front. *Development* (2015) 142, 2014-2025. doi:10.1242/dev.117507
*these authors contributed equally to the work

Author contributions The author of this thesis performed all computational modelling and co-wrote the above manuscript.

3.1 An extended computational model of multicellular streaming migration

In the last chapter we reviewed the relevant literature and considered several computational frameworks. We chose the framework used in McLennan *et al.* (2012) as the most appropriate to build upon. However, there are adjustments and improvements to the model that we need to address. These are outlined below. Methodological details of our implementation and parameterisation are described in Sections 3.1.2-3.1.4, and the parameter sensitivity is tested in Section 3.1.5. For a brief overview, the basic model components are illustrated in Fig. 3.1.

The basic computational model, as described by McLennan *et al.* (2012), comprises individually represented cells undergoing an off-lattice position jump process, coupled with a reaction-diffusion description of chemoattractant on a growing domain. This hybrid model was used to show that migration of a cell population consisting of both leaders and followers could be more invasive than migration of a population of only leaders, which would result in cells getting lost in regions of depleted chemoattractant,

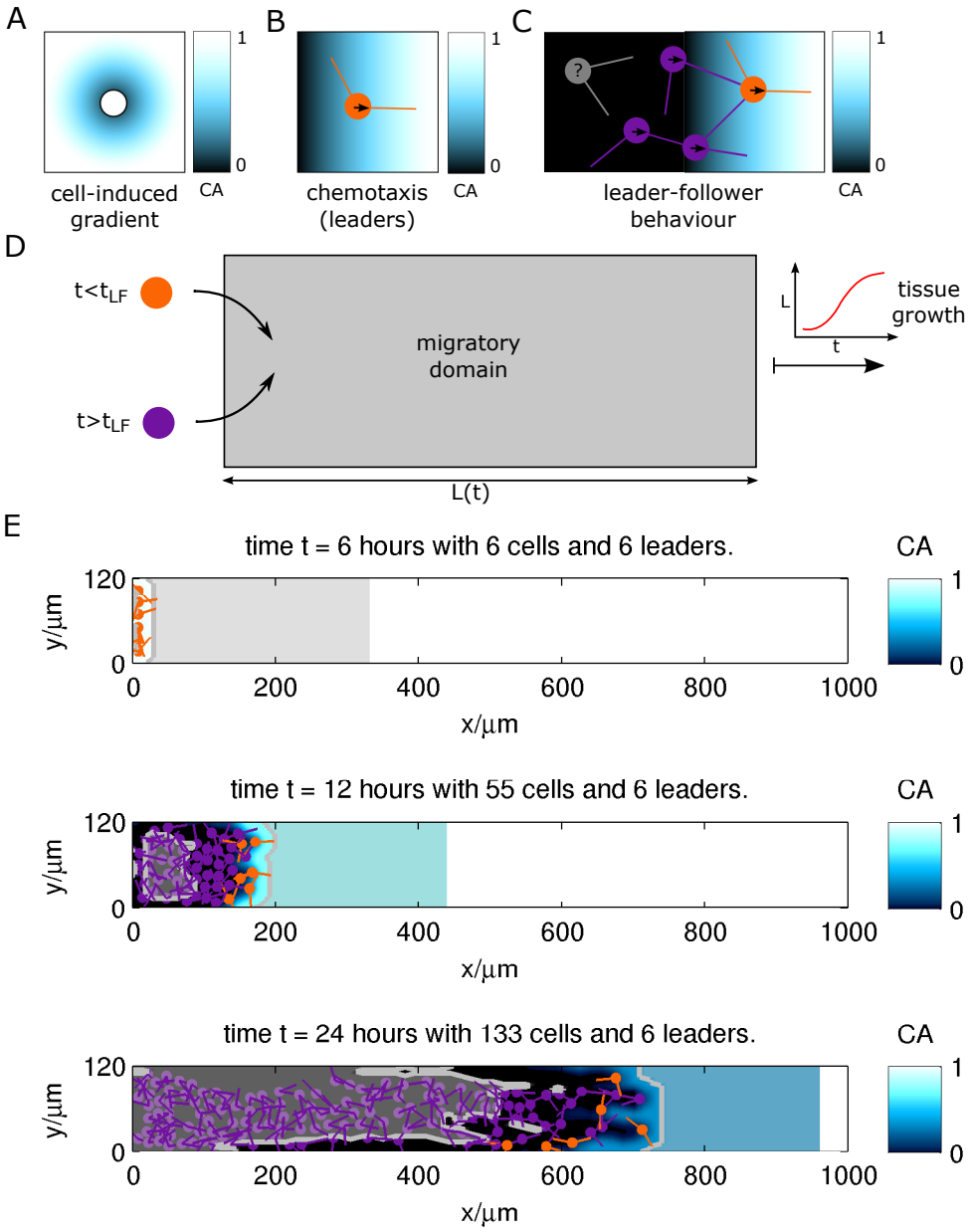

Figure 3.1: The basic components of our computational framework are: (A) Cell-induced gradient - Cells internalise chemoattractant near them. (B) Chemotaxis - Leader cells (orange) randomly sample directions and move up the chemoattractant gradient. (C) Leader-follower behaviour - Follower cells (purple) randomly search for other cells and, if within reach, adopt their direction of movement. (D) Migratory domain - Cells are inserted into the origin of the domain ($x = 0\,\mu$m) throughout the simulation, but only if there is sufficient space, so that cells do not overlap. The domain stretches over time, representing tissue growth, diluting chemoattractant and contributing to cell movement. (E) Sample simulation at three time-points. The grey contour represents regions in which the chemoattractant gradient is too shallow to be sensed.

blocking the space for further influx of cells into the domain. In tandem with gene profiling of the front and back portions of the neural crest cell stream, this served as a proof of concept of follow-the-leader migration in a cell-induced gradient. However, the computational model behaviour needed to be characterised further to demonstrate in more detail the dependence of the simulation results on the choice of parameters. Then, to advance this work further, we also refine those model features that, in the light of advanced knowledge of the biological system, were deemed less appropriate than originally thought.

3.1.1 Model criticism and modifications

In what follows, we describe the changes we made to the computational model (McLennan *et al.*, 2012) in light of the above discussion. In addition to addressing these issues, we have made improvements to the computational efficiency of the code and the visualisation of the simulation results, which we do not describe here[2].

First, we found the previous model displayed a variability in outcome of migration that was greater than is observed *in vivo*. To address this, the sensing rate (implemented through the number of directions sampled per time-step) has been increased to give cells more chance of finding each other or a favourable chemoattractant gradient (and thus reducing the variance of migration outcome). At the same time, the sensing distance has been shortened to more closely mirror the length of typical filopodia *in vivo* (see Table 3.1). The number of directions sampled per time-step is not necessarily the same as the number of filopodia, as the "computational filopodia" can sample faster than actual filopodia, as was also the case in McLennan *et al.* (2012). To represent the range of filopodial lengths measured *in vivo*, the model now allows a range of distances between cells that are in contact, stretching beyond the basic sensing radius to a maximum distance before cells lose contact. This also increases robustness, where previously the stream could easily break up due to stochastic effects, such as in which order cells move.

Secondly, the simulated migration was very chain-like, which in chick is seen in neural crest cells at the r7 axial level (post-otic[3]), but not at r4 (pre-otic[4]), where the migration is more stream-like (Kulesa and Fraser, 1998, Wynn *et al.*, 2013). To alter the morphology seen in the simulations, we have changed the mechanism of how cells follow each other. Upon contact with a leader, followers now adopt their leader's

[2]Access to the github repository may be given upon request.
[3]behind the ear, i.e., on the tail-side of the ear.
[4]before the ear, i.e., on the head-side of the ear.

direction of movement, rather than moving towards the leader. This is consistent with experimental evidence and prevents cell chains from moving to the vertical centre of the domain, therefore making the cell stream more spread out. In addition, followers attach to the edge of another cell, rather than its centre, which makes it easier for followers to find other cells and more realistically represents the contact between cells and its distance constraints.

Thirdly, the chemoattractant gradient was not fully cell-induced. In the previous model, the chemoattractant concentrations were set to zero at the boundary of the domain to represent inhibitory zones on either side of the migratory route (which are observed *in vivo*). This established a pre-existing chemoattractant gradient towards the domain centre. We have found such zero boundary conditions not to be necessary, as the inhibitory zones can be represented by not allowing cells to move beyond the edge of the domain. The previous fixed boundary (Dirichlet) conditions for the chemoattractant were also problematic as they could cause (presumably) biologically unrealistic flow of chemoattractant out of the domain, causing loss from the system. The chemoattractant reaction-diffusion-equation (RDE) now has zero-flux boundary conditions with constant initial conditions at the boundary, rather than being fixed to zero. These new boundary conditions also allow for a wider, more representative stream profile.

As a consequence of a more realistic stream morphology (compare Fig. 3.1E and Fig. 2.3C), the number of cells in typical simulations also increased, since more cells could move into the domain. This allows us to make predictions about the required fraction of leaders at meaningful, realistic cell densities. Cranial neural crest cells enter the migratory path at a rate of about 45 per hour (Kulesa and McLennan, personal communication), so that after 18 hours of migration, there should be around 800 cells, assuming the rate of cell entry is constant. Our computational model, however, is a two-dimensional representation. Since the stream of migrating cells is about 4-5 cells high (Kulesa, personal communication), the model should have cell entry rate of about 10 per hour, or 180 cells in the stream after 18 hours of migration. This is just a rough estimate, and the cell numbers *in vivo* have yet to be determined more accurately, but we obtain the right order of magnitude in our simulations. This increase in cell numbers was achieved in part through the altered stream morphology and in part by making the migration, particularly that of follower cells, more efficient through the increased sensing rate, so that cells migrate away from the insertion side of the domain quickly enough to make room for new cells to enter (as they do *in vivo*).

Lastly, in the original model cells could sense gradients in the chemoattractant as low as machine precision, which we consider to be unrealistic. Basic biophysical arguments, such as those by Berg and Purcell (1977) and various extensions of their work (Endres and Wingreen, 2008, Kaizu *et al.*, 2014), suggest a limit to the accuracy with which cells can sense molecular gradients. We introduced a finite sensing accuracy, i.e., a threshold level of relative chemoattractant gradient that must be exceeded for a cell to be able to obtain directional information. Further details of the derivation, implementation and parameterisation of the sensing accuracy in our model can be found in Sections 3.1.2.1, 3.1.3 and 3.1.4.2, respectively. A finite sensing accuracy of cells may be one of the fundamental limitations that makes the division of labour into leaders and followers necessary for a cell population that needs to migrate in a cell-induced chemoattractant gradient. By explicitly including a sensing accuracy, we have made the model less dependent on the numerical accuracy of any particular implementation, and thereby more intellectually rigorous.

3.1.1.1 Lengthscales and dimensionality

As the migration of cranial neural crest cells *in vivo* takes place in the three-dimensional mesenchyme of the embryo, the question arises whether it is appropriate to study this using a two-dimensional model, as was the case for the model in McLennan *et al.* (2012) (Fig. 2.3), and indeed for all of the existing models of collective cell migration reviewed in Section 2.2. A two-dimensional approximation is often used for migration of epithelial sheets or cells on a flat substrate *in vitro*, where the lengthscale in the vertical dimension is much smaller that in the horizontal dimensions. In the chick cranial neural crest, migration occurs in streams (Fig. 2.1, 3.4) that are much thinner than they are long. Naïvely, this would suggest a one-dimensional approximation may be appropriate. However, one-dimensional models cannot allow for cells moving around each other, and would lead to cells blocking each other more frequently. Another pertinent characteristic of chick cranial neural crest migration is that it occurs along the two-dimensional ectoderm, which is also the source of the chemoattractant VEGF (Fig. 2.1, 2.2). Thus, the two-dimensional model discussed here can be considered to represent the layer of cells closest to the ectoderm. *In vivo*, the stream of cells migrating from r4 is about six cells wide and four to five cells high (Kulesa, personal communication), so there would be additional cells adjacent to the layer represented in the model. Unfortunately, we are unaware of any data quantifying how the VEGF distribution varies or the extent to which cells change position along the transverse

direction, i.e., the radial direction in the embryo. As long as the constraints from relevant data are this loose, we may learn very little from three-dimensional extensions to the discussed computational frameworks. Therefore, we will proceed with the two-dimensional representation, but revisit the role of dimensionality when discussing avenues for further work in Chapter 7.

Having motivated and outlined the extension to the computational framework, we now state the model equations, pseudocode and comment on the parameterisation and sensitivity, so that the interested reader may reproduce our simulations.

3.1.2 Model equations

The model equations for tissue growth and reaction-diffusion of the chemoattractant are as previously described in McLennan *et al.* (2012), with a minor correction in the scaling of chemoattractant internalisation with domain length (see Eq. (3.2), where the factor of L_x^2 in the exponential function was missing in McLennan *et al.*, 2012).

Domain growth Tissue growth was modelled as uniform, with the length of the migratory domain at any time between $t = 0$ and $t = 24$ hours given by the logistic equation

$$L_x(t) = L_0 \left(\frac{L_\infty e^{a(t-t_s)L_\infty}}{L_\infty - 1 + e^{a(t-t_s)L_\infty}} + 1 - \frac{L_\infty e^{a(-t_s)L_\infty}}{L_\infty - 1 + e^{a(-t_s)L_\infty}} \right), \tag{3.1}$$

with parameters $L_0 = 300\mu\text{m}, a = 0.08\text{h}^{-1}\mu\text{m}^{-1}, t_s = 16$ hours, $L_\infty = 870$, determined by least-squares fitting to experimental domain length measurements (McLennan *et al.*, 2012).

Chemoattractant reaction-diffusion To model the change in chemoattractant concentration on a growing domain with $(x, y) \in [0, L_x(t)] \times [0, L_y]$, we rescale the growing domain to a stationary domain of unit length in x. To maintain numerical accuracy as the effective lattice spacing increases due to the rescaling, we use a solver with automatic grid refinement (`d03ra` from the Numerical Algorithms Group (NAG)), as was done is studies using the previous model (McLennan *et al.*, 2012, Dyson, 2013). Omitting the explicit time dependence of L_x, the change of chemoattractant concentration at a point $(x, y) \in [0, 1] \times [0, L_y]$ of the stationary domain is

given by the RDE

$$\frac{\partial c}{\partial t} = D\left(\frac{1}{L_x^2}\frac{\partial^2 c}{\partial x^2} + \frac{\partial^2 c}{\partial y^2}\right) - c\sum_{i=1}^{N(t)} \frac{\lambda}{2\pi R^2} \exp\left[-\frac{L_x^2(x-x_i)^2 + (y-y_i)^2}{2R^2}\right] + \chi c(1-c) - \frac{\dot{L}_x}{L_x}c, \tag{3.2}$$

where the terms on the right-hand side describe diffusion, internalisation, production and dilution (by tissue growth, the dot denoting time derivative), respectively. Scaling factors of L_x are introduced by rescaling to a stationary domain to solve numerically on a grid of unit length (McLennan *et al.*, 2012). Parameter names and values are given in Table 1.

3.1.2.1 Chemotaxis sensing accuracy

Berg and Purcell (1977) derive a fundamental biophysical limit to the accuracy with which a cell can sense a chemical gradient. We briefly outline their derivation here before commenting on parameterisation. For a more detailed derivation, see the original work (Berg and Purcell, 1977).

The fundamental limit in the accuracy of concentration measurements is due to fluctuations in the numbers of molecules, and is derived by Berg and Purcell (1977) for the case of a perfect sensor that counts molecules in a given volume. The sensing accuracy is in fact different for a perfect sensor and a perfect absorber that counts molecules absorbed on a given surface. The latter might be deemed more realistic for a chemosensing cell, but the difference is only a numerical factor of about two (Endres and Wingreen, 2008). However, Endres and Wingreen (2008) show that this factor is larger when a sensor is measuring a gradient instead of a concentration. We consider cells sensing the concentrations of a chemoattractant at the cell body and the tip of a protrusion. Thus the gradient is determined from two individual concentration measurements, and the sensing limit for the concentration, rather than gradient, is of interest to us.

The fluctuations in particle number, N, are proportional to $\sqrt{N}$. This statement is reasonable despite our continuum treatment of the chemoattractant, in the sense that we can consider the behaviour of the mean and fluctuations around the mean separately in an approximation of the overall system. If particle numbers (and hence concentrations) are very high, then this would simply drive the sensing accuracy to very small values, as fluctuations in particle number go to zero. If one was to assume a complete lack of fluctuations, cells could sense arbitrarily small concentrations, and

therefore gradients, of chemoattractant, which corresponds to the limiting case of $N \to \infty$. Additional noise in measurement may also come from the intracellular machinery downstream of the receptor (ten Wolde *et al.*, 2015).

To proceed with the derivation, consider a perfect sensor counting N molecules in a volume V with background (or average) concentration $\bar{c}$. The inaccuracy in a single concentration measurement is

$$\frac{\Delta c}{\bar{c}} \approx \frac{1}{\sqrt{N}} = \frac{1}{\sqrt{V\bar{c}}}, \tag{3.3}$$

in three dimensions, or $1/\sqrt{A\bar{c}}$ in two dimensions, where A is the measurement area. The count of molecules can be improved by repeated measurements. A sensor counting molecules in a volume can make $n = TD/V^{2/3}$ independent measurements in a time T, based on the timescale of a molecule diffusing through the measurement volume V. This improves the (root mean square) measurement error by $1/\sqrt{n}$ (Berg and Purcell, 1977). Thus, with $V \sim R^3$, the measurement uncertainty reduces to

$$\frac{\Delta c}{\bar{c}} \approx \frac{1}{\sqrt{DT\bar{c}R}} =: \zeta, \tag{3.4}$$

in three dimensions, or $\Delta c/\bar{c} \approx 1/\sqrt{DT\bar{c}}$ in two dimensions. Here we have introduced the dimensionless parameter ζ, which depends on the background concentration, c. To account for the dynamically changing background concentration, we explicitly scale ζ in simulations by the current relative concentration, i.e., $\sqrt{c_0/c}$, where c_0 is the starting background concentration (see Section 3.1.3 for pseudocode). The exact derivation of the sensing accuracy introduces a numerical factor of order unity, but since we can only parameterise the sensing accuracy to orders of magnitude (see Section 3.1.4.2), we ignore this.

Kaizu *et al.* (2014) revisit the Berg-Purcell limit and derive corrections to the sensing limit by considering diffusive ligand transport as well as receptor binding kinetics. Since we assume our reactions to be diffusion limited, these corrections do not apply. Similarly, one can correct for movement of the cell relative to the medium to derive the apparent gradient seen by the cell and its detection limit (Dusenbery, 1987), but we assume this to be negligible. The use of different sensing strategies, signalling networks and energy expenditure to achieve and improve upon fundamental sensing limits is a subject of ongoing research (ten Wolde *et al.*, 2015). While this is a fascinating topic in its on right, we simply do not have knowledge of the molecular parameters in our application at the required level of detail to consider the many, subtly different sensing models.

A different threshold-based movement model has been used to model zebrafish lateral line migration by Dalle Nogare *et al.* (2014), but without biophysical motivation.

3.1.3 Pseudocode

For model simulations, this code was implemented in Mathwork's MATLAB, and the chemoattractant profile was solved using the Numerical Algorithms Group's (NAG) `d03ra` (see appendix to this chapter), as in McLennan *et al.* (2012) and Dyson (2013). In the interest of reproducibility, rather than just repeatability, we give the pseudocode to be implemented in the reader's programming language of choice.

main function

initialise model parameters and any cells already in the domain ▷ see Table 3.1
for $t = 6$ to 24 **do**
    if $t =$ insertion time **then**
        if there is space to insert a cell **then**
            insert a new cell at start of domain
        end if
    end if
    solve chemoattractant profile ▷ see Eq. (3.2)
    grow domain, update cell positions ▷ see Eq. (3.1)
    move cells
end for

move cells

for $i = 1$ to number of cells **do**
    pick a cell at random without replacement
    pick n_{filo} random directions
    if cell is a leader **then**
        measure chemoattractant concentration at cell position,

$$c_{\text{old}} = \int c(x, y) \exp\left[-\frac{x^2 + y^2}{2R^2}\right] \mathrm{d}x\, \mathrm{d}y$$

        measure chemoattractant concentration in random direction(s) at distance l_{filo} away (pick highest), c_{new}
        if $\frac{c_{\text{new}} - c_{\text{old}}}{c_{\text{old}}} \geq \zeta \sqrt{\frac{c_0}{c_{\text{old}}}}$ **then** ▷ gradient is above (scaled) sensing accuracy

8: move in chosen direction
9: **else** ▷ cell has not found a favourable chemoattractant gradient
10: move in random direction
11: **end if**
12: **else if** the cell is attached **then** ▷ cell is following another cell
13: **if** other cell is within l_{filo} **then**
14: move in same direction as other cell
15: **else** ▷ other cell is out of reach
16: detach cell
17: **end if**
18: **else** ▷ the cell is a detached follower
19: check if there is another cell in random direction(s) at distance l_{filo} (pick closest)
20: **if** a cell was found and is a leader (or part of a chain in contact with a leader) **then**
21: move in same direction as other cell
22: **else**
23: move in a random direction
24: **end if**
25: **end if**
26: **end for**

Note on volume exclusion: Any attempted movement is aborted if it would lead to overlap with another cell or the domain boundary.

3.1.4 Parameterisation

See Table 3.1 for values of parameters used in model simulations, and below for explanations of selected parameters.

3.1.4.1 Notes and further references

Experimental time Cell migration is assumed to start approximately six hours after electroporation ($t = 0$).

Directions sampled per time-step, n_{filo} This cannot be directly related to the number of filopodia, which are greater in number, but sample at a lower speed (McLennan *et al.*, 2012).

Table 3.1: **Model parameters**
Parameter values listed were used as a default, unless otherwise stated. Where a range is given, the model gives qualitatively similar results within that range, and the value in parentheses is the one used as a default. The chemoattractant concentration is implemented in relative units, such that the starting value $c_0 = 1$.

	Description	Value	Reference
n_{filo}	directions sampled per time-step	2	n/a, Section 3.1.4.1
Δt	simulation time-step	1 min	n/a
R	cell radius (nuclear)	$7.5\,\mu$m	McLennan and Kulesa (2010)
v_{lead}	cell speed (leader cells)	$41.6\,\mu$m/h	Kulesa *et al.* (2008)
v_{follow}	cell speed (follower cells)	$49.9\,\mu$m/h	Kulesa *et al.* (2008)
L_y	height of domain	$120\,\mu$m	McLennan *et al.* (2012)
L_x	length of domain (grows, Eq. (3.1))	300 to $1100\,\mu$m	McLennan *et al.* (2012)
l_{filo}	sensing radius	$27.5\,\mu$m	Section 3.1.4.1
$l_{\text{filo}}^{\max}$	max. separation of cells in contact	45μm	Section 3.1.4.1
D	diffusivity of chemoattractant	0.1 to $10^5\mu\text{m}^2$/h (0.1)	Section 3.1.4.1
χ	production rate of chemoattractant	10^{-8} to 1/h (10^{-4})	Section 3.1.4.1
λ	chemoattractant internalisation rate	10^2 to 10^4 (10^3) μm^2/h	Section 3.1.4.1
k_{in}	rate at which cells enter the domain	10/h	Section 3.1.4.1
ζ	sensing accuracy	0.001 to 0.25 (0.1)	Section 3.1.2.1

Sensing radius, l_{filo} This was calculated as the sum of the cell radius ($7.5\,\mu$m) and the mean filopodial length (which was directly measured from the cell body (Fig. 3.2B) to be $9\,\mu$m and estimated from total cell size (Fig. 3.2A) to be circa $20\,\mu$m). Since we have only implemented contact between filopodium and cell body, but not between two filopodia, which does occur *in vivo* (Teddy and Kulesa, 2004), we allow for a greater effective length.

Maximum cell separation before contact is lost, $l_{\text{filo}}^{\max}$ The maximum cell size including filopodia was measured to be $86.3\,\mu$m (Fig. 3.2A), half of which gives an estimate of maximum cell separation of $43.15\,\mu$m. Independent measurements of filopodial lengths gave a maximum of $30.4\,\mu$m (from the cell body, Fig. 3.2B), which, together with the cell radius $R = 7.5\mu$m and the average filopodial length (allowing for interfilopodial contact) of $9\,\mu$m, gives an estimate of $46.5\,\mu$m.

Diffusion coefficient of chemoattractant, D The primary identified chemoattractant in chick cranial neural crest migration is VEGF^{165} (McLennan *et al.*, 2010). Its related isoform VEGF^{164} is known to bind to ECM, and studies in angiogenesis estimate as little as 1% may be freely diffusing, the rest bound to ECM and

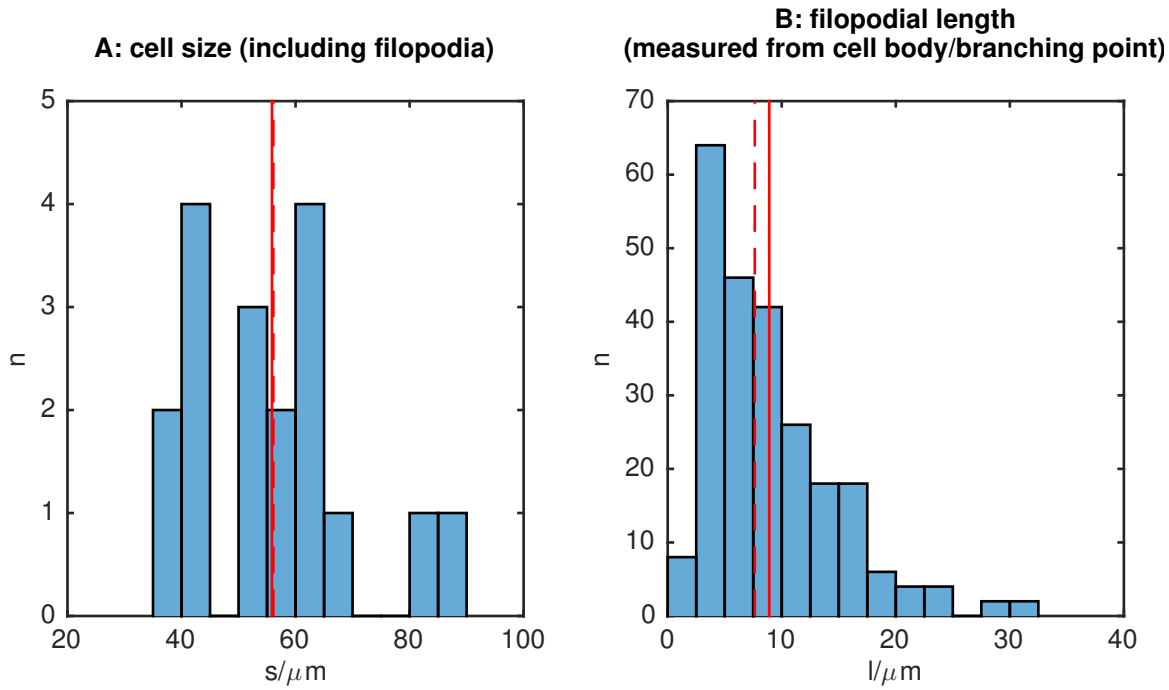

Figure 3.2: Histograms of cell size and filopodial length measurements. Solid lines show mean, dashed lines show the median (overlapping in A). Cell sizes were taken from the greater of the two side lengths of the smallest bounding box containing the cell and its filopodia. Data were provided by Jessica M. Teddy from the Kulesa Lab.

cellular receptors (Mac Gabhann *et al.*, 2006). Hence, we choose a low effective diffusivity. For freely diffusing VEGF *in vivo*, angiogenesis modelling studies have used much higher values of $0.36\,\mathrm{mm}^2/\mathrm{h} = 3.6 \cdot 10^5\,\mu\mathrm{m}^2/\mathrm{h}$ (Jain and Jackson, 2013) and $104\,\mu\mathrm{m}^2/\mathrm{s} \approx 3.7 \cdot 10^5\,\mu\mathrm{m}^2/\mathrm{h}$ (Mac Gabhann *et al.*, 2006). However, with diffusivities of that order of magnitude our model simulations still give qualitatively similar results (Section 3.1.5).

There are different isoforms of VEGF, and they have different solubility, ECM binding affinity (with longer isoforms being more strongly bound) and degradation rates (Vempati *et al.*, 2011). They can be expressed differentially, but longer isoforms can also be cleaved into shorter ones by matrix metalloproteinases (MMPs). Chemoattraction of neural crest cells has mainly been studied for isoform VEGF-A^{165} (McLennan *et al.*, 2010), but it is unclear whether longer isoforms and cleavage through MMPs, which neural crest cells express, play a role.

Production rate of chemottractant, χ In other tissues, VEGF production, or estimates thereof, range from 0.01-0.20 molecules/cell/s (Yen *et al.*, 2011), or 4.39-$5.27{\cdot}10^{-5}$ molecules/μm$^-2$/s (Vempati *et al.*, 2011) to $0.25 \cdot 10^{-17}\,\mathrm{pmol}/\mu\mathrm{m}^2/\mathrm{s}$(Mac Gabhann *et al.*, 2006). In our system, the rate of VEGF production is unknown and difficult to measure (McLennan, personal communication). However, it is outweighed by internalisation through migrating neural crest cells, as VEGF is not seen to be replenished in trailing portions of the stream (McLennan *et al.*, 2010). Thus, we assume χ to be low.

Chemoattractant internalisation rate, λ To our knowledge, no estimates or measurements of VEGF internalisation rate of chick cranial neural crest exist. Angiogenesis studies have used values of $k_{\mathrm{VEGFR2}} = O(10^{-4})/\mathrm{s}$ per receptor (Mac Gabhann and Popel, 2005, Yen *et al.*, 2011). Berg and Purcell (1977) estimate the number of receptors needed for a near-optimal sensing accuracy as $N_R = R/s$, where R is the cell radius and s the receptor size. With $s = O(\mathrm{nm})$, we can estimate the near-optimal number of receptors to be $N_R \geq 10^4$. If receptor internalisation rates are comparable to other tissues, a lower bound for the total internalisation rate would be given by $k_{\mathrm{VEGFR2}} N_R \geq 1/\mathrm{s}$ (per cell). From this we estimate the chemoattractant consumption, as defined in (3.2), to be $\lambda \geq O(10^3)\mu\mathrm{m}^2/\mathrm{h}$. However, the concentration of VEGF in our system is unknown, and hence the units of c, and therefore λ, in our model are arbitrary. We assume a high λ to ensure quick consumption of chemoattractant by cells (see also sensitivity analysis in Section 3.1.5).

Rate at which cells enter the domain, k_{in} This is the rate of attempted cell insertions, and not the effective rate seen *in vivo*. In a typical simulation, on the order of 10% of insertions are unsuccessful. Greater values of the insertion rate thus result in equal or only slightly increased cell numbers. It should be noted here again that our simulations are a two-dimensional abstraction of the three-dimensional migratory stream, which may contain 4-5 times as many cells *in vivo* in the transverse (z) direction. Thus, cell numbers in (unperturbed) simulations are approximately correct for a section of the migratory stream, to within the accuracy that total cell numbers are known *in vivo*.

3.1.4.2 Parameterisation of the sensing accuracy

Most of the variables upon which the sensing accuracy depends are underdetermined in the case of chick cranial neural crest migration, such as VEGF diffusivity, D, VEGF background concentration, $\bar{c}$, and the sensing time, T. Nevertheless, we can proceed to estimate order of magnitudes, which can serve as bounds for our model simulations.

Background concentration, $\bar{C}$ The concentration of VEGF used in *in vitro* experiments is $1\,\mu$g/ml (McLennan *et al.*, 2010), which, at a molecular weight of $19.2\,$kDa ≈ 20kg/mol, leads us to estimate $\bar{c} \approx 3 \cdot 10^7/\mu\text{m}^3$ (50mM).

Sensing time, T The time-step of our simulations is $\Delta t = 1$ minute, and we assume that a cell takes up only a fraction of this time with sensing, and most of it with movement. We could therefore estimate $T \leq 0.1 \cdot \Delta t = 0.1$ minutes. If we relax our assumptions, this estimate might change by an order of magnitude. This would only change the sensing accuracy by a factor of roughly 1/3, which gives qualitatively similar results in typical model simulations.

Lower bounds on gradient measurement accuracy For the measurement of a gradient, i.e., the difference between two concentration measurements, the Berg-Purcell limit (3.4) increases by a factor of $\sqrt{2}$ (Goodhill and Urbach, 1999). With the estimates for $\bar{c}$ and T as above, and the parameter values $D = 0.1\,\mu\text{m}^2/\text{h}$ and $R = 7.5\,\mu$m (Table 3.1), we obtain an estimate of the sensing accuracy (3.4) of $\zeta_{d=3} \approx 0.002$ in three dimensions, or $\zeta_{d=2} \approx 0.01$ in two dimensions. These can be taken as a lower bound for the (order of magnitude of) sensing accuracy of neural crest cells in our model. Note that the sensing accuracy rescales with changing background

concentration, which has to be taken care of in the computational implementation (see Section 3.1.3).

3.1.5 Parameter sensitivity

In this section we characterise the model behaviour, in particular exploring the parameter sensitivities of basic model results and discussing uncertainties in constraints from experimental data.

3.1.5.1 Robustness of follow-the-leader advantage

One of the key results in McLennan *et al.* (2012), who were using a previous version of the model described here, was the proof of principle that multicellular streaming migration in a cell-induced chemoattractant gradient is more invasive, in terms of how far cells migrate as a cohesive group, when the front 30% of cells are undergoing chemotaxis, and the back 70% undergo follow-the-leader migration, compared to a population where every cell is undergoing chemotaxis. This result was not shown to have been tested for robustness with respect to the model parameters, some of which are not well constrained by experimental results. Here we address this issue and test the sensitivity of the follow-the-leader advantage (over all-leader migration) to perturbations of individual parameters in the reference set of parameters (Table 3.1).

The biologically relevant outcome of the migration of cranial neural crest cells for the development of the organism is the invasion of the target areas and colonisation of the migratory route (Kulesa *et al.*, 2010, Dyson, 2013). Migration profiles (histograms of cell number vs distance migrated) are a useful measure to assess migration outcome quantitatively and compare in detail different cases (see Section 3.2). For the purpose of practicality we want to further reduce the dimensionality of our summary statistics, so here we simplify to the combination of two numbers: the furthest distance migrated and total number of cells at the typical simulation end-point ($t = 24$ hours experimental time or $t = 18$ hours after the start of migration).

To test robustness of the follow-the-leader advantage, we compare the extreme cases of migration with only leader cells to the case where only the front row of cells adopts leader behaviour. For each case, we run repeated simulations ($n = 20$) and visualise the qualitative difference in migration outcome, as well as its variability, using our two-dimensional summary statistic (see Fig. 3.3). We address a number of under-constrained parameters and modelling choices in turn, perturb the reference parameter set and repeat the model simulations. Joint perturbations of multiple

parameters simultaneously are beyond the scope of this thesis, as the combinatorial complexity to exhaustively test all combinations or parameters is too great to allow for the necessary simulations on practical timescales.

3.1.5.2 Model insensitive parameters

The main advantage of follow-the-leader migration, found in this work and previous studies (McLennan *et al.*, 2012), is an increase in the number of cells entering the domain, with only a slight increase in distance migrated (Fig. 3.3). The latter can be explained by volume exclusion: The more cells fill the domain and occupy space, the fewer chances there are for a cell to move backwards into empty space should it not find a favourable chemoattractant gradient. Overall follow-the-leader migration has a more variable, but better, outcome than all-leader migration (Fig. 3.3).

Chemoattractant production, χ The outcome of our model simulations remain qualitatively similar when increasing background chemoattractant production, $\chi = 0.0001/h$ by a factor of 10^4 to $1/h$, with a slight reduction in the follow-the-leader advantage (Fig. 3.3), which can be explained by the increased availability of chemoattractant to form gradients and guide leader cells into the domain. Decreasing the chemoattractant production by a factor of 10^4 to 10^{-8}/h has little effect on the migration, indicating that the default parameter value is in a regime where the chemoattractant consumption is strong enough to reduce the concentration to near zero. In addition to varying the strength of the chemoattractant production parameter, χ, we could also vary the functional form of the production term, such as constant production or $\Theta(1-c)$ (where Θ is the Heaviside step function), to keep the concentration finite. Such a structural sensitivity analysis may move the bounds of feasibility in our parameter space, but this may be of little use in the absence of further quantitative constraints on the production, diffusion and degradation parameters from experimental measurements. The important phenomenology, as far as we can tell, is that there is a uniform VEGF distribution in the chick before migration, and little or none once the bulk of cells has migrated past (McLennan *et al.*, 2010).

Sensing accuracy, ζ A similar outcome to increasing the chemoattractant production is seen when improving the sensing accuracy, $\zeta = 0.1$ by a factor of 100 to $\zeta = 0.001$ (Fig. 3.3). Increasing the sensing accuracy threshold, i.e., making sensing less accurate, slightly improves the distance migrated in leader-only simulations

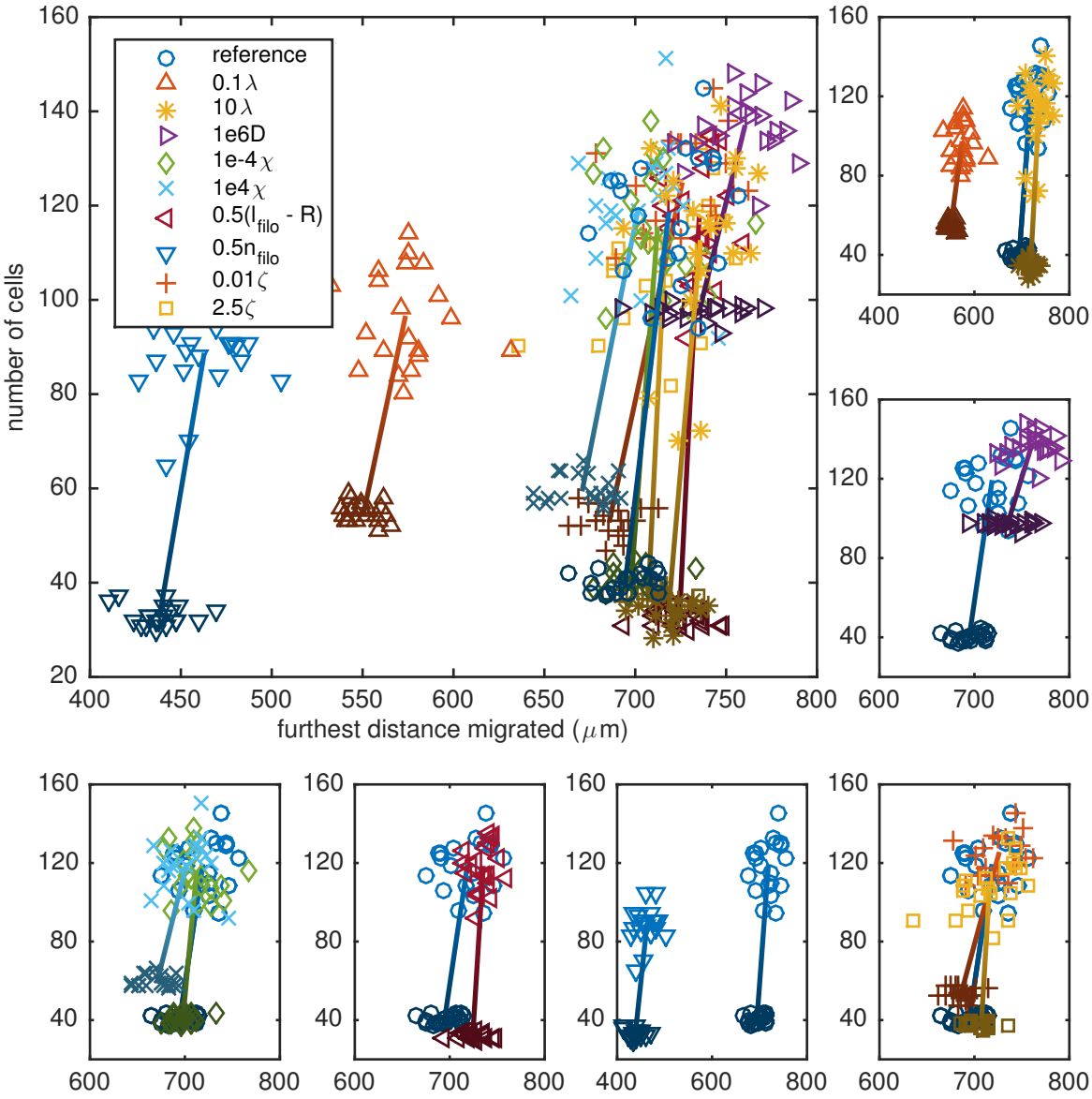

Figure 3.3: Comparison of migration outcome, measured in furthest distance migrated and total number of cells (at $t = 24$ hours), for migration with leaders only (dark colours) and only the first six cells being leaders (light colours). Straight dark-to-light lines connect the mean simulation outcomes, their length quantifies the advantage of leader-follower migration over individual chemotaxis. Scattered points are individual simulation outcomes ($n = 20$) for the reference simulation (using default parameters) and various parameter perturbations (see legend). The spread of points visualises the variability of migration outcome. Panels show individual parameter permutations in isolation.

(as cells only follow steeper gradients, which tend to be in the relevant direction of migration), but does not reduce the follow-the-leader advantage.

Sensing radius, l_{filo} To implicitly implement inter-filopodial contact we have chosen the effective filopodial length, $l_{\text{filo}} - R = 2 \times 10\mu\text{m}$ (where R is the cell radius) to be approximately twice the average measured filopodial length (Fig. 3.2). Relaxing this assumption, and reducing the sensing radius to $R + 10\mu\text{m}$, we find that migration in our model is barely affected. In fact, follow-the-leader migration does slightly better, whereas a population of only leaders migrates further than with the reference parameter value, but with a slight decrease in cell number (Fig. 3.3).

3.1.5.3 Model sensitive parameters

Number of directions sampled, n_{filo} Chemotaxis is a crucial part of our model of cell migration, thus it is expected that reducing the rate of directional sampling decreases the distance migrated, as fewer randomly sampled directions per time-step, n_{filo}, mean fewer chances to find a favourable chemoattractant gradient. This is confirmed in our parameter perturbation study (Fig. 3.3).

Chemoattractant consumption, λ When the rate of chemoattractant consumption by cells, $\lambda = 1000\mu\text{m}^2/\text{h}$, is increased by a factor of 10, the result is a slight increase in the distance migrated. When this rate is decreased by a factor of 10, the distance migrated is reduced, as is the advantage of follow-the-leader migration (reducing the number of cells for follow-the-leader migration, while slightly increasing the number of cells for the leader-only simulations, Fig. 3.3). Bearing in mind that this is a large perturbation compared to the change in outcome, i.e., a low elasticity[5], the model is not highly sensitive to this parameter. This result also suggests it is not worthwhile investigating differences in chemoattractant consumption between leader and follower cells.

[5]The elasticity, ϵ, of a simulation output (or summary statistic), Y, with respect to a parameter, p, can be calculated from the reference set, Y_0, p_0, and the perturbations, $Y_\pm, p_\pm$, as

$$\epsilon = \frac{Y/Y0}{p/p_0} = \frac{(Y_+ - Y_-)/Y_0}{(p_+ - p_-)/p_0}.$$

Chemoattractant diffusivity, D We recognise that a high chemoattractant consumption together with a low diffusivity and production rate characterise the cell-induced gradient regime, and that we do not have good experimental estimates for these parameters for the chick cranial tissue. As argued in Section 3.1.4, there is clear evidence for a cell-induced gradient *in vivo* (McLennan *et al.*, 2010), so it makes sense to restrict the model usage to this regime. However, as we are ignorant of the diffusivity, D, of chemoattractant VEGF *in vivo*, it is interesting to investigate how the migration outcome depends on it. A high diffusivity results in a shallower chemoattractant gradient that is spread out over a larger distance, so as long as the relative magnitude of this gradient is above the sensing accuracy threshold, we would expect a high diffusivity to improve chemotaxis and thus reduce the advantage of follow-the-leader migration over the all-leader case. This is what we see when increasing $D = 0.1\,\mu\text{m}^2$ by a factor of 10^6 (Fig. 3.3). Note that even with high diffusivity there is still an advantage of follow-the-leader migration. We suspect this to be due to the fact than when every cell is undergoing chemotaxis, more cells sample unfavourable directions in the chemoattractant gradient, and as a result more cells move undirectedly part of the time. This illustrates a potentially general trade-off between efficiency and robustness, as more cells adopting a leader state may cause an increase in robustness (each cell is independent, lower chance of stream break-up), while fewer leaders increase migration efficiency.

3.1.5.4 Other parameters

Parameters that are experimentally well determined for our chosen model system of chick cranial neural crest migration were not systematically tested for their model sensitivity, such as cell size, speed, domain height and length and rate of cells entering the domain.

3.2 Neural crest migration is led by just a few cells in the invasive front.

In this section we use our extended computational model to revisit a key biological question that has so far only been answered incompletely (McLennan *et al.*, 2012): What is the size of the subpopulation of cells in a leader state that we hypothesise to drive cranial neural crest migration in the chick embryo? In other words, how many cells need to read out directional information, under realistic conditions, to guide the whole population?

3.2.1 How many leaders?

Previous evidence makes a clear case for the existence of multiple behavioural and morphological phenotypes within a group of migrating neural crest cells in the vertebrate embryo. For example, imaging studies show difference in cell motility, proliferation and morphology in chick (Kulesa and Fraser, 1998, Teddy and Kulesa, 2004, Kulesa *et al.*, 2008, 2010, McKinney *et al.*, 2011, Ridenour *et al.*, 2014) and mouse neural crest (Young *et al.*, 2014). More specifically, follow-the-leader behaviour has been observed in chain migration of neural crest cells in the chick gut (Wynn *et al.*, 2012) and stream migration of cranial neural crest cells (Kulesa *et al.*, 2010, McLennan *et al.*, 2012). In the cranial neural crest, cells at the migratory front have more membrane protrusions and are less polarised. Gene profiling has shown statistical differences in the expression of a range of genes between cells at the front and back of the migrating stream (McLennan *et al.*, 2012), and computational modelling of neural crest cell migration has demonstrated the advantage of collective follow-the-leader migration in the cell-induced gradient setting (McLennan *et al.*, 2012). What has remained unclear from these studies is at what scale of the population these heterogeneities in gene expression and migratory characteristics are functionally relevant, whether there are further subpopulations to be identified, and how the population heterogeneity changes intrinsically over time or with the microenvironment the cells are passing through. The work in this section addresses how the size of a leader subpopulation affects the overall migration. The dynamical induction of this subpopulation by microenvironmental signals will be addressed in Chapter 4.

3.2.1.1 Regional differences in gene expression *in vivo*

Evidence for heterogeneity of the neural crest cell population at a scale smaller than previously measured is provided by a new set of experiments. The stream of neural crest cells was dissected into eight[6] subdivisions and the expression of 77 genes was analysed semi-quantitatively using real-time quantitative polymerase chain reaction (RT-qPCR) (for methodological details see McLennan *et al.*, 2015a), showing heterogeneity throughout the stream at the scale of individual segments (Fig. 3.4), with different patterns of expression for different genes. For selected genes, the spatial distributions of gene expression were visualised using fluorescent multiplex *in situ* hybridisation (McLennan *et al.*, 2015a) in tissue sections spanning the whole length of a neural crest stream. These results indicate that there is more heterogeneity in the neural crest than was previously known.

These results served as motivation for our computational experiments. To explore the functional relevance of the heterogeneity, we conducted computational simulations varying the number of leader cells. The aim was to predict whether cells adopting a leader state should be found in the first two or three dissected segments of the stream, only the first one, or if even finer subdivisions should be considered, in the case that leaders make up only part of the first experimentally isolated subdivision, or are distributed in a broader, more complex pattern throughout the stream. It was hitherto unclear how the number of leader cells in a population of followers affects the overall migration outcome. This is a parameter currently impossible to control *in vivo*, as we have only begun to identify potential markers for leader cells and genes controlling their behaviour in the course of this study, for which the computational experiments were useful to narrow down candidates of genes that mark a leader state and verify their functional role. The ability to conduct impossible experiments computationally – *de facto* an extension of the thought experiment to more complex and complicated settings – is a key advantage of modelling that is highlighted when done in close integration with experimental work.

3.2.1.2 Computational experiments to vary the number of leader cells

To test aspects of our hypothesis that are difficult to probe experimentally *in vivo*, we use our extended computational framework. Specifically, we ask whether the number of lead cells that can detect spatial gradients in the chemoattractant is a crucial factor for the success of neural crest cell migration. Should this be the case, then

[6]The number of subregions was chosen based on what could be reproducibly laser-dissected.

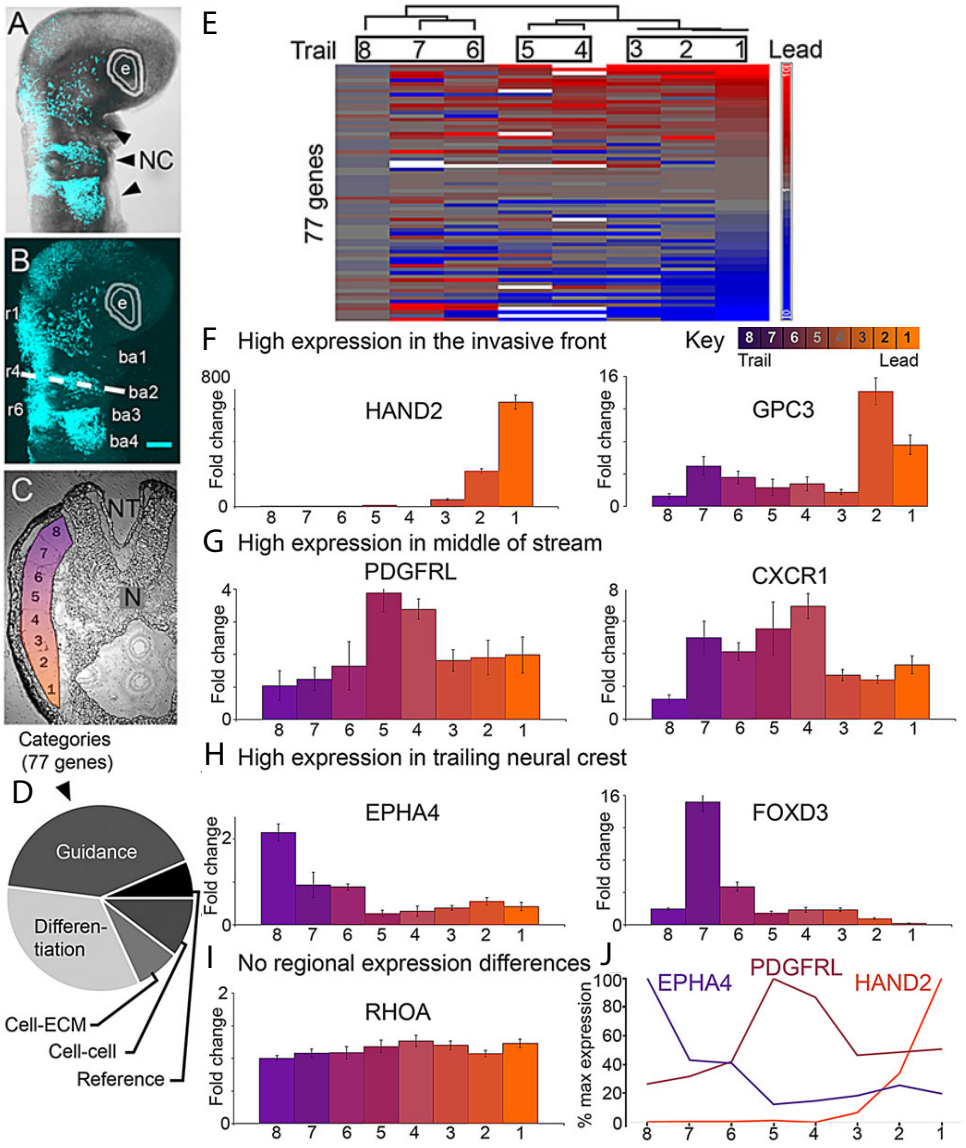

Figure 3.4: Regional differences in gene expression within the chick cranial neural crest. (A-D) Schematic of the gene profiling experiment. (D) Hierarchical clustering of the expression from the eight dissected subregions. (F-J) Patterns of expression for selected subset genes. Error bars show standard error of the mean. Adapted from (McLennan *et al.*, 2015a) (with permission from the Company of Biologists).

the gene expression patterns detailed *in vivo* (Fig. 3.4, and McLennan *et al.*, 2015a) would be consistent with this constraint. To test the effect of varying the number of leaders, we restricted the model simulations (in this section, and in McLennan *et al.*, 2015a) to only include non-plastic cell behaviours, such that individual cells that begin migration as leaders (or followers) could not switch from being a leader to a follower (or *vice versa*). To change the fraction of all migrating cells that are leaders, we varied the time, t_{LF}, at which new cells entering the domain are prescribed followers instead of leaders (Fig. 3.5A): all cells that entered the migratory domain up to time t_{LF} were specified as leaders, and cells that entered after that were specified as followers.

Our simulations reveal that the median distance migrated and the stream density both increase with decreasing leader fraction (Fig. 3.5). While the furthest distance migrated does not change noticeably, it is the movement of cells away from the entrance to the migratory domain (corresponding to near the dorsal neural tube) that proves crucial for the successful migration pattern (Fig. 3.5). This prevents jamming near the domain entrance and enables a higher number of cells to distribute more evenly along the migratory pathway (Fig. 3.5). Thus, our computational model predicts that a small number of lead cells can efficiently guide the migration of the entire neural crest cell migratory stream.

This trend of "fewer leaders is better" cannot be extrapolated to zero leaders, in which case the followers move in a random, undirected manner and stay close to the entrance of the domain. Directed migration with a single leader cell is possible in our model, but is less robust to stream break-up (Fig. 3.8).

Another limitation to note is that, the way our model is set up, we cannot control the fraction of leader cells directly. As the success of cell insertion depends on available space, which in turn depends on stochastic cell movement, the final number of cells cannot be fixed. Therefore, the actual leader fraction for a given parameter combination over multiple realisations is variable. We give the full results in Fig. 3.9, but the conclusion remains the same.

In summary, results from our computational simulations show that migration with fewer leaders can be more efficient, suggesting that only a few cells confined to the narrow front of the neural crest stream need to adopt the invasive leader state to achieve overall directional migration.

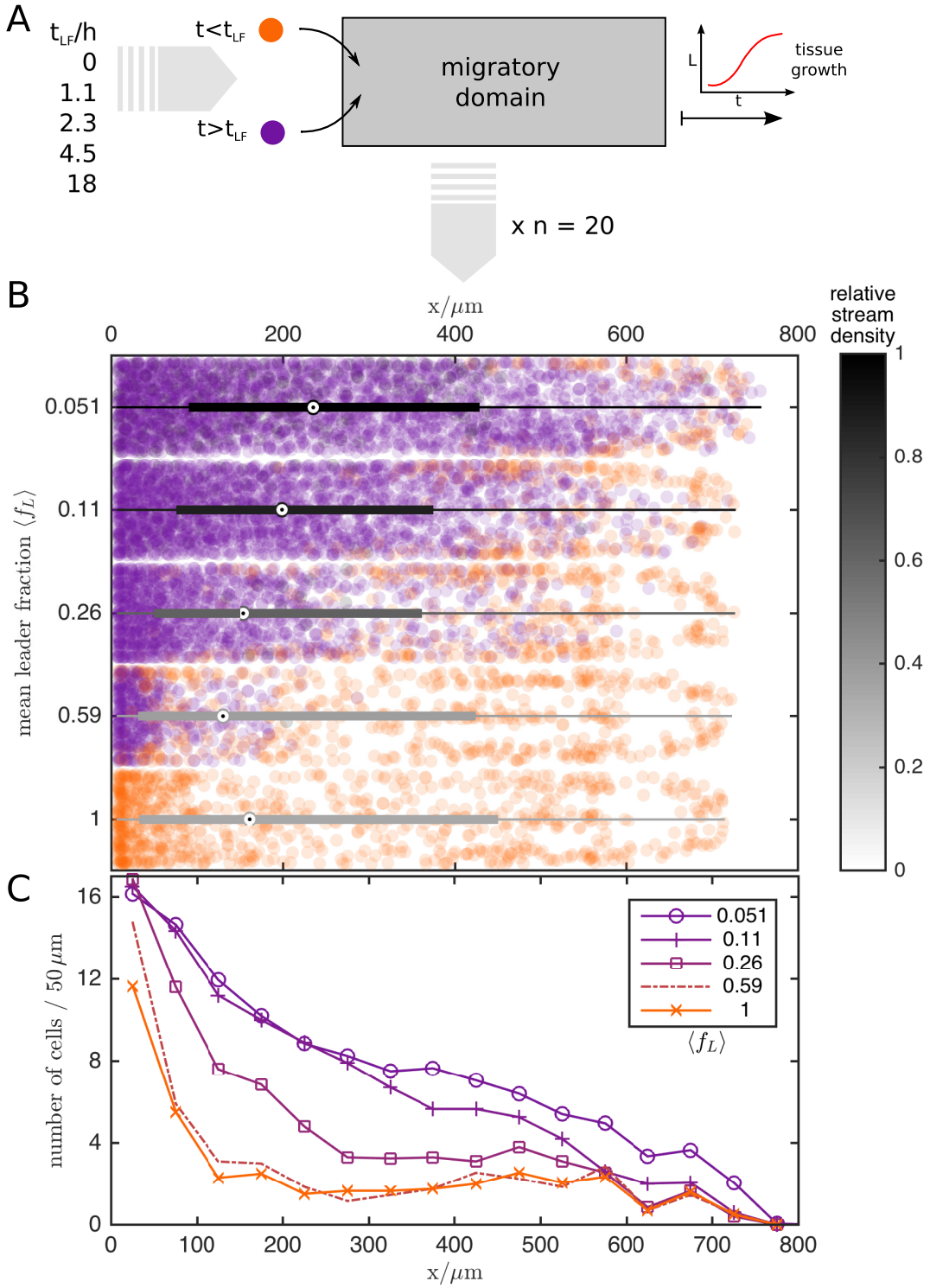

Figure 3.5: Computational experiment that varies the leader fraction predicts stream migration is more efficient with fewer leaders. (A) Schematic of computational experiment. (B) Final cell positions from $n = 20$ simulations at five different average leader fractions, $\langle f_L \rangle$. Greyscale box plots of distance migrated are overlaid, the colour of each box showing the relative stream density. (C) Cell counts versus distance migrated. Adapted from McLennan *et al.* (2015a) (with permission from the Company of Biologists).

3.2.1.3 Evidence for single cell scale heterogeneity: Molecular profile of trailblazers

Motivated by the above results, our collaborators isolated single cells from the most distal stream (that had no other cells in front of them), dubbed "trailblazers" (McLennan *et al.*, 2015a), and compared their gene expression over time and relative to single cells from four subdivisions (quartiles) of the migratory stream. From this, a set of genes was identified as differentially expressed between trailblazers and the cells from the rest of the stream. Two transcription factors, *HAND2* and *TFAP2A*, that are highly expressed in the front three subregions of the stream and regulate the genes identified as the "trailblazer molecular profile" (McLennan *et al.*, 2015a) were then functionally tested through knock-down and overexpression and the resulting effect on migration outcome.

3.2.2 Perturbing cell states in computational and *in vivo* experiments

Based on the hypothesis that the genes expressed uniquely by trailblazer cells are important to their migratory behaviour and that trailblazers act as leaders for trailing cells, two transcription factors regulating these genes were knocked down (using morpholinos[7]). While loss of *HAND2* mostly changed cell morphology, loss of *TFAP2A* function reduced the number of cells distributed along the stream as well as the distance migrated and area covered at later stages (HH stage 15) of migration.

It was also tested whether overexpression of the same transcription factors would affect the migration pattern. While *TFAP2A* overexpression had little effect on the distribution of cells along the migratory route, *HAND2* overexpression caused a loss in the number of cells, but no reduction of the distance migrated (Fig. 3.6).

To mimic the overexpression of a trailblazer gene signature within the trailing subpopulation, we modified the model parameters to convert 50% of trailing cells into leaders. This represents the transfection of 50% of the neural crest cells within the trailing subpopulation with overexpression of the transcription factors of the trailblazer signature[8]. When we forced trailing cells to display a lead cell phenotype in simulations, we found that cells remain near the entrance of the migratory domain (Fig. 3.7). This migratory pattern is similar to the model simulations scenario that

[7]Morpholinos are short pieces of DNA-like molecules that can be used to block gene expression.

[8]At the time of writing, transgenic chicks are difficult to create and not commonly used. Instead, genetic constructs are injected and electroporated into the cells, which does not achieve 100% efficiency in terms of transfecting every cell.

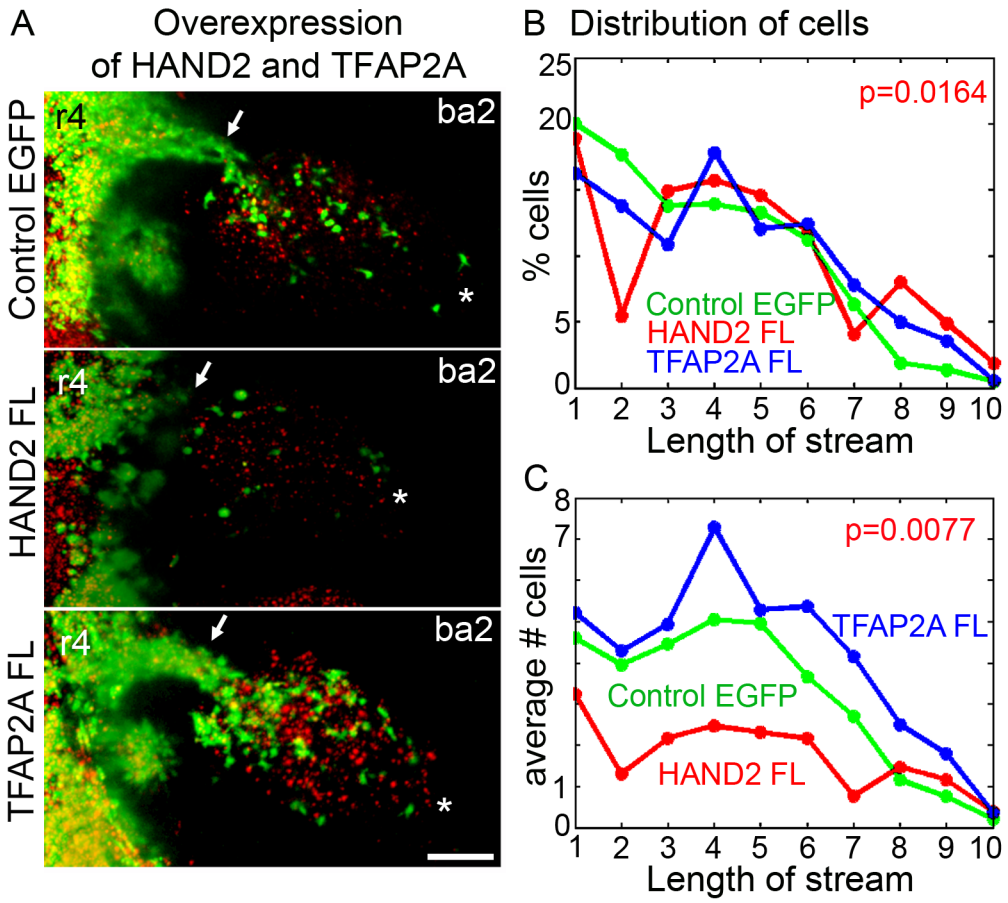

Figure 3.6: Upregulation of transcription factors alters neural crest migration pattern. (A) Trailing neural crest cells transfected with control EGFP ($n = 20$), *HAND2* ($n = 13$) or *TFAP2A* ($n = 14$) overexpression constructs (green) and DiI (red). Asterisks mark the position of the migratory front and arrows point to the thinnest portion of the stream. (B) Distribution of the percentage of transfected cells and (C) average number of cells along the stream. Adapted from McLennan *et al.* (2015a) (with permission from the Company of Biologists).

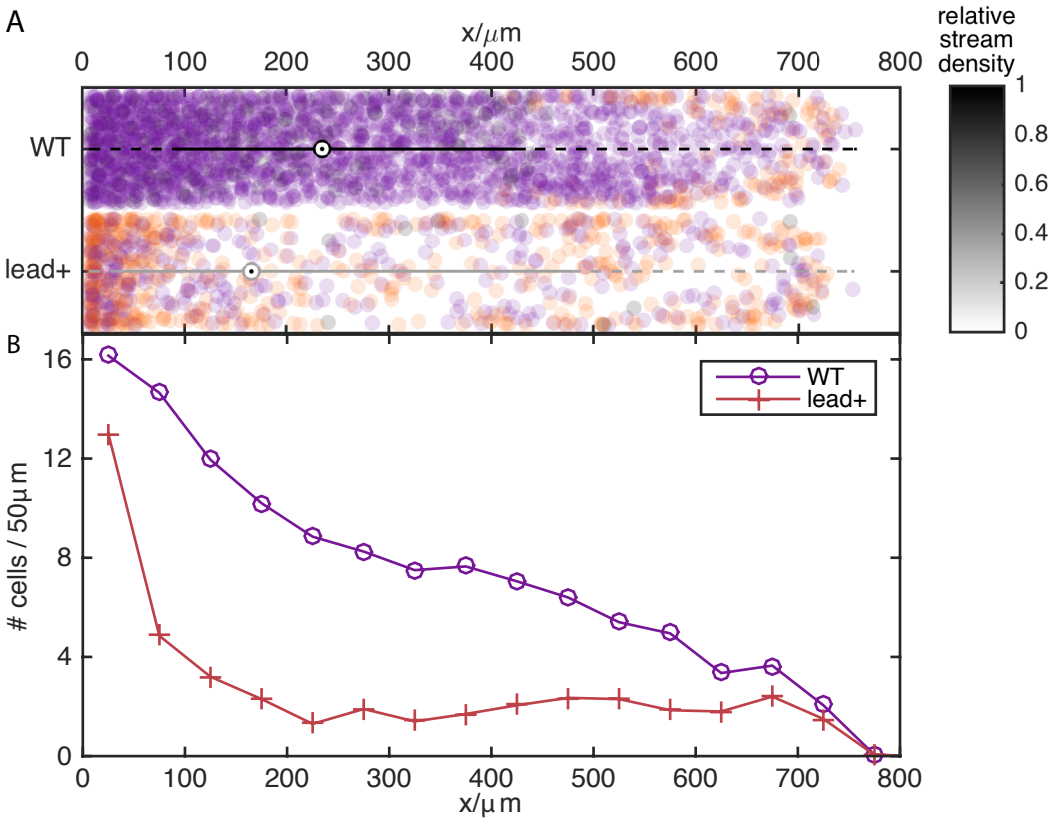

Figure 3.7: Forcing leader behaviour in trailing cells disrupts model migration. (A,B) Model simulations of the upregulation of a leader-like behaviour in the trailing cells. After time t_{LF}, every other cell inserted into the domain is a leader (orange) rather than a follower (purple). (A) Overlay of final cell positions from $n = 20$ individual realisations of control (WT) and perturbed (lead+) simulations. Greyscale box plots show distance migrated, and their colour gives the relative stream density (as in Fig. 3.5). (B) Cell counts versus distance for control and perturbed simulations. Adapted from McLennan *et al.* (2015a) (with permission from the Company of Biologists).

introduced higher lead cell fractions (Fig. 3.5). Thus, forcing a lead cell behaviour within the trailing subpopulation in model simulations predicts disruption to neural crest cell migration that would be observed as cell crowding near the dorsal neural tube exit.

One limitation of our study is that we cannot rule out other effects of the knockdown and overexpression perturbations, such as delamination defects, and thus cannot claim direct equivalence between our model simulations with perturbed leader fraction and the overexpression of a single transcription factor from the trailblazer gene profile.

To summarise, we have varied not just the number, but also the distribution of leader cells along the migratory path in our computational simulations, and observed

similar outcomes to the overexpression experiments. This further demonstrates consistency of the experimental results with our hypotheses that the molecular profile of trailblazer cells is associated with leader-like migratory behaviour.

3.2.3 Discussion

Motivated by the evidence from gene expression analysis for heterogeneity at small scales within the neural crest cell population, we used our extended computational model to predict that this population can be guided by just a few leader cells reading out directional information from the chemoattractant gradient. In fact, migration was found to be more efficient, under the conditions studied, with fewer leader cells rather than more. This, in turn, motivated single cell gene profiling experiments, which led to the identification of a "trailblazer molecular signature" (McLennan *et al.*, 2015a), including two transcription factors hypothesized to control leader behaviour. To test this hypothesis, the expression of these transcription factors was perturbed, resulting in alterations to the migration pattern. These were qualitatively similar to the results from our computational experiment in which we forced a subset of trailing cells to be in a leader state, mimicking the (hypothesised) experimental perturbation. Together the results from this integrated experimental-computational study show further consistency of observed chick cranial neural crest cell stream dynamics with the model of follow-the-leader migration under the cell-induced gradient hypothesis.

There is known plasticity of the leader-like state, which we have thus far ignored. To theoretically test the effect of the number of lead cells in driving multicellular stream migration we had to restrict our computational experiments to the case of non-plastic lead and trailing cell behaviours. We did this even though previous tissue transplantation experiments showed chick cranial neural crest cells alter their gene expression profile depending on cell position within a stream. Here, we disabled phenotype switching in our computational model simulations, for otherwise we would have only been able to change the leader fraction transiently, before phenotype switching restored it towards the unperturbed case. Alternatively, we could have set up the computational model simulations with varying initial lead cell fractions and, given appropriate microenvironmental parameters, observe what leader fraction emerges naturally from phenotype switching. However, this would require at least a phenomenologically correct implementation of switching, which, in turn, ought to be verified experimentally. This investigation was outside the scope of this chapter, but will be addressed in Chapter 4.

In summary, we have successfully narrowed down the functional role of leader-follower heterogeneity in collective cranial neural crest cell migration. In the course of this study, richer and more complex heterogeneities have been discovered at the gene expression level. Before this can be explored using mechanistic models, functional perturbation experiments, through spatiotemporally targeted knock-down and overexpression of genes, must lead the way to generate hypotheses for further interrogation. This lies outside the scope of this thesis. Instead, we turn our attention to the plasticity and dynamics of the leader-follower heterogeneity by studying its control through interactions with the embryonic microenvironment in Chapter 4.

Chapter appendix

Numerical solver for chemoattractant PDE

The partial differential equations (PDE) for the evolution of the chemoattractant profile (3.2) was solved using `d03ra` from the NAG MATLAB toolbox. The function `d03ra` solves parabolic[9] PDEs on a two-dimensional rectangular grid using the method of lines. The method of lines reduces the PDE to a system of ordinary differential equations, which are then solved using a backwards differentiation formula method. This particular solver is only recommended for non-zero diffusion constants, as the PDE ceases to be parabolic when the diffusion coefficient is zero, but has been reported to work well in practice even with the low values of diffusivity ($D = 0.1\,\mu\text{m}^2\text{h}^{-1}$) used in Dyson (2013), with solutions changing gradually for decreasing values of the diffusivity. A key feature of `d03ra` that makes it suitable for solving PDEs on a growing domain is automatic mesh refinement. Thus, we can map Eq. (3.2) to a stationary domain of unit length by scaling the rates of reactions and diffusion with length and let `d03ra` take care of inserting more mesh points as needed. Further details about the algorithm can be found in the official documentation see `http://www.nag.co.uk/numeric/MB/manual64_24_1/html/D03/d03raf.html` and references therein.

[9] A second-order PDE of the form

$$A\frac{\partial^2 f}{\partial x^2} + 2B\frac{\partial^2 f}{\partial x \partial y} + C\frac{\partial^2 f}{\partial y^2} + D\frac{\partial f}{\partial x} + E\frac{\partial f}{\partial y} + F = 0,$$

where A, B, C, D and E are constants, is called "parabolic" when $B^2 - AC = 0$.

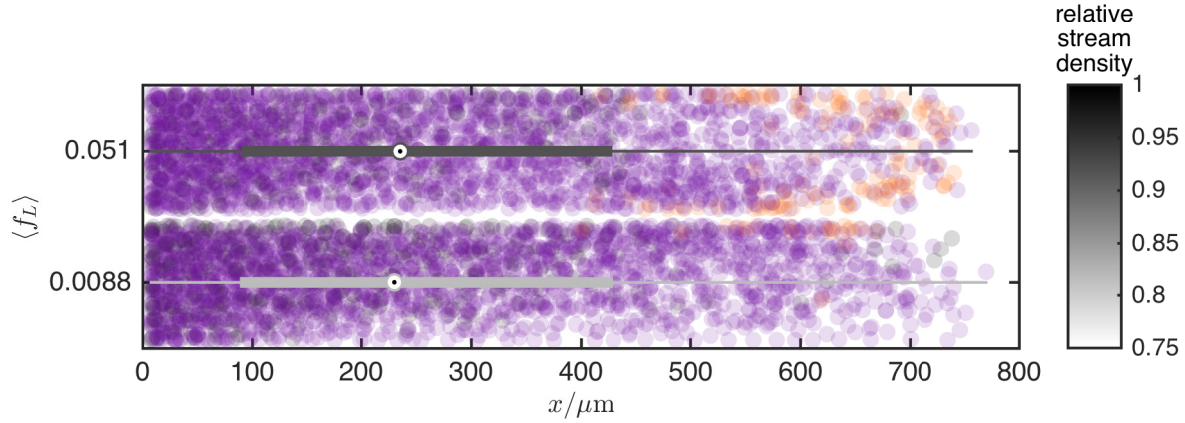

Figure 3.8: Final cell positions for a reference simulation (top) and one with only a single leader cell (bottom), overlaid for $n = 20$ realisations each. Leader cells in orange, follower in purple and followers that have lost contact in grey. Greyscale boxplots show distance migrated, and their colour gives the relative stream density.

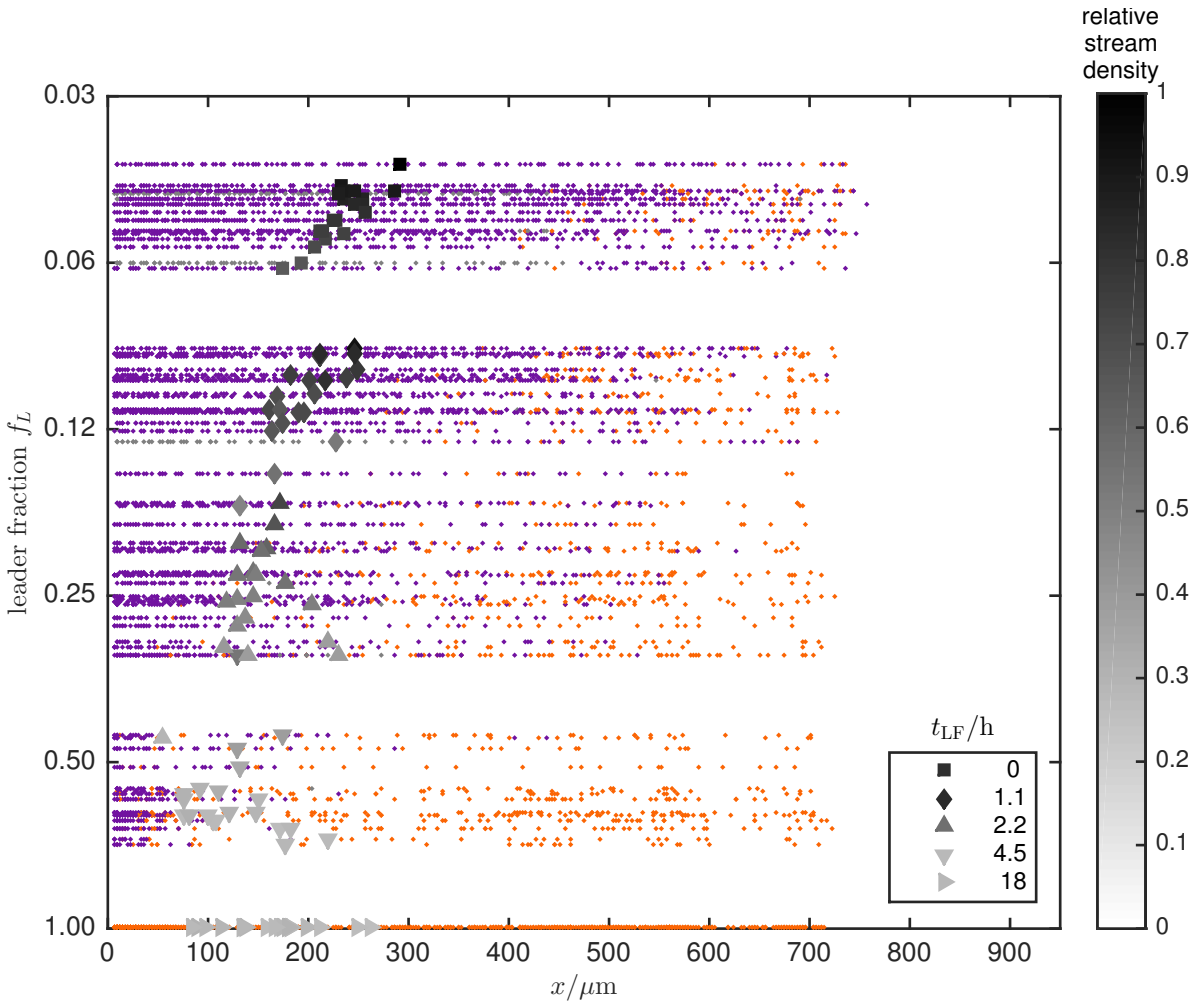

Figure 3.9: Computational experiment that varies the leader fraction, as in Fig. 3.5, showing the final distance migrated (at $t = 24$ hours) for every cell in each individual realisation. Leader cells are shown in orange, followers in purple. Positions of cells in the y-direction have been ignored for this visualisation. Different symbols show different parameter values for the follower start-time, t_{LF} (see legend, note that for $t_{\mathrm{LF}} = 0$ only the first six cells initialised at the start of each simulation are leaders), and their position indicates the median distance migrated, while their colour gives the relative stream density. As can be seen, there is a spread of leader fractions resulting from each parameter value, but little overlap between the range of outcomes from simulations with different parameter values.

Chapter 4

Dynamics of leader-follower transitions

"Leader and follower cells should be considered as different cell states and not different cell types."
Rørth (2012)

In the previous chapter, we showed that collective migration of neural crest cells in the cell-induced gradient model could be guided optimally by just a few leader cells. This was confirmed by gene expression analysis, which identified a molecular profile of "trailblazer cells" at the most distal, narrow front of the migrating stream (McLennan *et al.*, 2015a). When forcing overexpression of a transcription factor associated with this trailblazer profile, migration was disrupted in a qualitatively similar way to simulating migration with cells in a leader state within the trailing portion of the stream.

In this chapter, we extend our computational model further to explore how cell heterogeneity during neural crest collective migration is controlled by microenvironmental signals. Given the observational evidence for plasticity between leader and follower states (McLennan *et al.*, 2012, 2015b), we want to test how much a cell's gene expression, and resulting migratory behaviour, are controlled by the main chemoattractant, VEGF, and on what timescale.

First, we introduce the reader to the evidence for plasticity of cell behaviour and gene expression in the neural crest cell population. To put our work into context, we briefly describe and critique previous attempts to incorporate this plasticity into computational models of neural crest migration. On this basis we motivate our hypothesis for a minimal model of leader-follower transitions controlled by VEGF, which we then test through a combination of simulations and experiments.

Comment on originality Work in this chapter draws on the following publication by the author and collaborators:

R. McLennan*, L. J. Schumacher*, J. A. Morrison, J. M. Teddy, D. Ridenour, A. Box, C. Semerad, H. Li, W. McDowell, D. Kay, P. K. Maini, R. E. Baker and P. M. Kulesa. VEGF signals induce trailblazer cell identity that drives neural crest migration. *Developmental Biology* (2015) 301, 227?39. doi:10.1016/j.ydbio.2006.08.019
*these authors contributed equally to the work

Author contributions The author of this thesis performed all computational modelling, contributed to planning and analysis of the time-course gene expression experiment, and co-wrote the above manuscript.

4.1 Biological background: Plasticity of cell behaviour and gene expression

In the previous chapter we presented evidence in chick cranial neural crest cell migration for the distinction of cells as leaders and followers. This raises the question as to whether these cell states are pre-specified before the start of migration, dynamically determined by signals in the microenvironment, or spontaneously emerge from cellular interactions. This is part of a larger, long-standing debate in the neural crest research community as to whether cell fate is predetermined or a result of position, i.e., local information, at the end of migration. Though we focus on differences in migratory behaviour, observations from the study of cell fate are important to put our work into context. For example, Lee *et al.* (2013) have found differences in the time of delamination from the neural tube between neural and non-neural ectoderm, suggesting a signature of pre-specification. In contrast to this, McKinney *et al.* (2013) have found that cells from different dorsoventral levels of the neural tube contribute equally to neural crest-derived tissues, and that exit position and time are uncorrelated to initial cell position in the neural tube. On shorter timescales, transplanting neural crest cells to different positions in the r4-stream has been demonstrated to result in behavioural and gene-expressions response to the microenvironment (McLennan *et al.*, 2012, 2015b). Furthermore, transplantation between different streams (along the anterior-posterior axis) has been found to change whether cells migrate in chains versus streams (Wynn *et al.*, 2013). Thus, even though there is conflicting evidence regarding the specification of cell fate, there is a clear functional plasticity to migration.

More specific evidence for plasticity between leader and follower states comes from the outcome of tissue transplantation and ablation experiments (McLennan *et al.*, 2012). In these experiments, trailing cells adopted leader-like behaviour and gene expression when transplanted to the front of the migrating stream. This suggests that the migratory state of a cell is controlled by signals in the microenvironment. A candidate for such a signal is VEGF, a known chemoattractant for migrating neural crest cells (McLennan *et al.*, 2010). This is corroborated by the observation that inhibiting neuropilin-1, a VEGF co-receptor, causes failure to reach and invade the branchial arch target site (McLennan and Kulesa, 2007). Thus, the hypothesis was formed that the presence of a directional signal in the form of a VEGF gradient determines the leader state of migrating neural crest cells (McLennan *et al.*, 2012).

4.1.1 Previous implementations of cell state plasticity

The hypothesis that the VEGF gradient induces cells to be in a leader state was explored computationally by McLennan *et al.* (2012), and the tissue transplantation experiments were reproduced qualitatively with simulations. Crucially, the computational experiments explained why leader cells transplanted to the back of the stream did not migrate along with the rest of the stream, as the surrounding tissue that was transplanted with them has a high concentration of VEGF, causing transplanted cells to stay as leaders within their local microenvironment. In this model, phenotypic plasticity was implemented such that cells would switch state depending on the fraction of directions around the cell that showed an increasing gradient in chemoattractant. Despite the model's success at enabling interpretation of the experimental observations, it is difficult to imagine a parsimonious intracellular mechanism to compute the fraction of directions in which the chemoattractant gradient is favourable.

Subsequent work instead indicated support for a mechanism in which cells switch state based on the time of exposure to increasing gradients (Dyson, 2013). However, we found this implementation to be: (a) not robust, as cells frequently switched back and forth between states; (b) unrepresentative, as simulations with plasticity did not reproduce typical stream morphologies; and (c) unrealistic, as cells would lose any memory of the time of exposure to VEGF upon seeing a decreasing gradient for just one time-step.

Here, we extend the time-of-exposure mechanism in our version of the computational framework from Chapter 3. First, we recognise that cells may have a decaying memory of the directional signal sensed, which makes state switching more realistic

and more robust (as argued above) than in previous model implementations (McLennan *et al.*, 2012, Dyson, 2013). Secondly, we allow the rates of switching to a leader state from a follower state and to a follower state from a leader state to be different. This is the integrate-and-switch mechanism described in Section 4.2. The rates of switching between migratory states are hitherto unknown, i.e., it is unclear for how long a cell needs be exposed to a gradient in the directional signal (or lack thereof) before it becomes a leader (or a follower). In order to parameterise our model, we helped to design an experiment in which neural crest cells were exposed to VEGF *in vitro*, and changes in gene expression in response to removal and readdition of this factor were measured over time. This experiment and the analysis of the results are discussed in Section 4.3. We then tested our hypothesis of VEGF-induced switching of migratory states *in vivo* and computationally by manipulating the chemoattractant distribution through introducing ectopic sources to induce a leader state in trailing cells and divert their migration, which is described in Section 4.4. In Section 4.5, we make further predictions, based on our new implementation of phenotypic plasticity, of how the emerging leader fraction depends on cell density and overall population size. We conclude this chapter with a discussion of the various results in Section 4.6.

4.2 Integrate-and-switch mechanism

By taking into account the biological evidence and limitations of previous modelling efforts, we aim to build a model for leader-follower plasticity that operates on a non-instantaneous timescale (or more generally, two separate timescales), and includes hysteresis, which should ensure robustness against small, local fluctuations in the chemoattractant profile. We can motivate this approach by imagining an intracellular biochemical switch, i.e., a bistable system that is driven to one fixed point (the leader state) in the presence of a signal, and a second fixed point (the follower state) in the absence of a signal. For the sake of simplicity, and due to the lack of knowledge about the intracellular signalling pathways involved, we utilise a minimal description of this phenomenon.

We introduce a variable that records for how long each cell has been exposed to the presence of a chemoattractant. This variable increases at a fixed rate when a chemoattractant gradient above the sensing accuracy threshold is sensed, and decreases otherwise at another fixed rate. These rates are inversely proportional to the parameters 'leader-to-follower switching time', τ_{LF}, and 'follower-to-leader switching time', τ_{FL}, respectively (Fig. 4.1). Thus, this variable effectively integrates the time

spent in a chemoattractant gradient (with a decaying "memory"), though this could be easily modified to instead record the magnitude of the gradient or absolute value of the concentration.

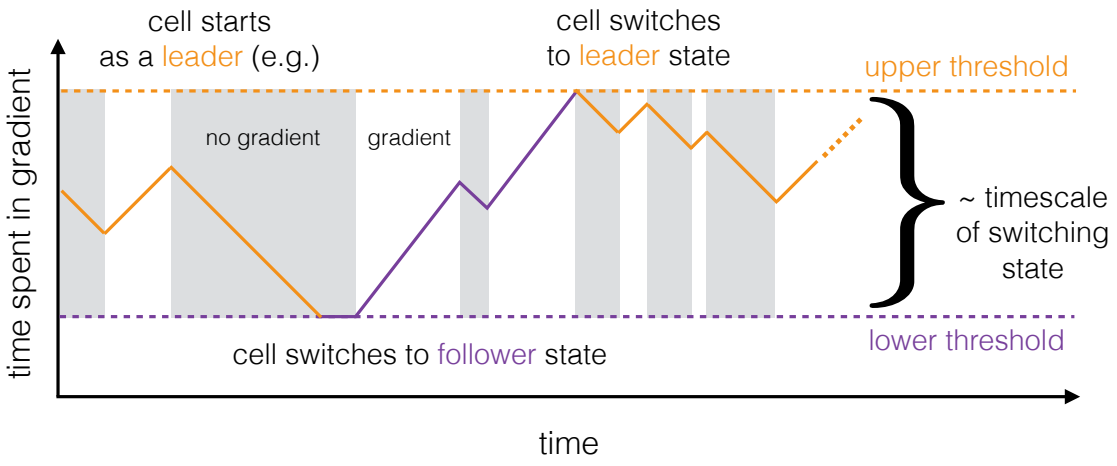

Figure 4.1: Schematic of the integrate-and-switch mechanism.

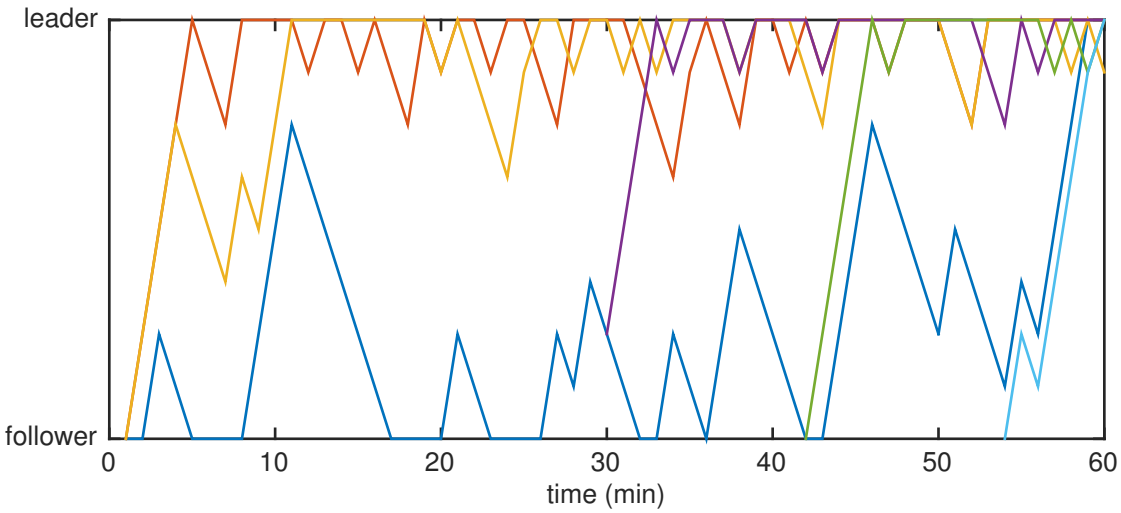

Figure 4.2: Integrate-and-switch traces for every other cell in the first hour of a randomly selected simulation in which cells start as followers and switch states with leader-to-follower switching time $\tau_{\mathrm{LF}} = 4$ minutes and follower-to-leader switching time $\tau_{\mathrm{FL}} = 8$ minutes. Other simulation parameters were used as stated in Table 3.1.

Once the net time spent in a chemoattractant gradient (with time in the absence of an increasing gradient counting negatively) reaches a threshold, follower cells switch state to adopt leader behaviour, i.e., begin to undergo chemotaxis. Once cells are in a leader state and remain in a positive chemotaxis gradient, they do not increase their signal sensed further, that is, they do not become further entrained to stay

in leader state, which would increase the time taken to switch back to a follower state in the absence of the gradient (see Fig. 4.2 for example cell states vs time from a typical simulation). Similarly, the intracellular signal decays with time spent in the absence of a positive gradient, until it becomes low enough for cells to switch to a follower state, and then does not decrease further (unless a gradient is found again). As a consequence, cells that have just switched state cannot switch back immediately, as long as the directional signal is lost/gained on timescales shorter than the switching time. Thus, through the combination of signal memory with state-switching thresholds, we have implemented a plasticity mechanism that operates at a non-zero timescale with hysteresis, which is what we aimed for.

4.2.1 Updated pseudocode

Pseudocode from Chapter 3 is reproduced here, with updates from this chapter highlighted in italics. For further implementation details of the computational framework, see Section 3.1.3.

main function

initialise model parameters and first cells ▷ see Table 3.1
for $t = 6$ to 24 **do**
    if $t =$ insertion time **then**
        if there is space to insert a cell **then**
            insert a new cell at start of domain
        end if
    end if
    solve chemoattractant profile ▷ see Eq. (3.2)
    grow domain, update cell positions ▷ see Eq. (3.1)
    move cells
    integrate-and-switch
end for

move cells

as in Section 3.1.3

integrate-and-switch

1: increase signal sensed for cells that have sensed a chemoattractant gradient (but not beyond the upper threshold)
2: decrease signal sensed for cells that have not sensed a chemoattractant gradient (but not below the lower threshold)
3: followers whose signal sensed is at the upper threshold switch to become leaders
4: leaders whose signal sensed is at the lower threshold switch to become followers

4.2.2 Migration outcome depends on the ratio of switching times

To explore how the behaviour of our computational model depends on the rates of switching between leader and follower states, as it is implemented in the integrate-and-switch mechanism (Fig. 4.1), we analysed migration efficiency for a range of switching timescales. We calculated the average number of cells in the domain at $t = 24$ hours, relative to the non-switching case (as in Section 3.2), for different combinations of leader-to-follower and follower-to-leader switching times (Fig. 4.3). Quantified in this way[1], migration efficiency was higher when switching times were similar to each other, which is illustrated clearly by replotting the data against the ratio of switching times (Fig. 4.4). Outcome variability, measured as the coefficient of variation of cell number, was also lower for equal switching times (Fig. 4.4). Interestingly, this suggests the model could be simplified by setting $\tau = \tau_{\mathrm{LF}} = \tau_{\mathrm{FL}}$ and still represent the optimal migration outcome.

Overall, migration was least efficient for unequal switching times (Fig. 4.3). In the context of our hypothesis that cell state plasticity is controlled by VEGF, this suggests a quick response to a VEGF signal requires an equally quick response to the loss of VEGF signal to maintain high migration efficiency and low variability. This represents an important constraint on the parameterisation of our model, which we will consider again when interpreting the experimental results of changes in gene expression over time in response to VEGF addition and removal.

[1]For an alternative visualisation, see full histograms for cell number vs distance migrated (Fig. 4.11) in the appendix to this chapter.

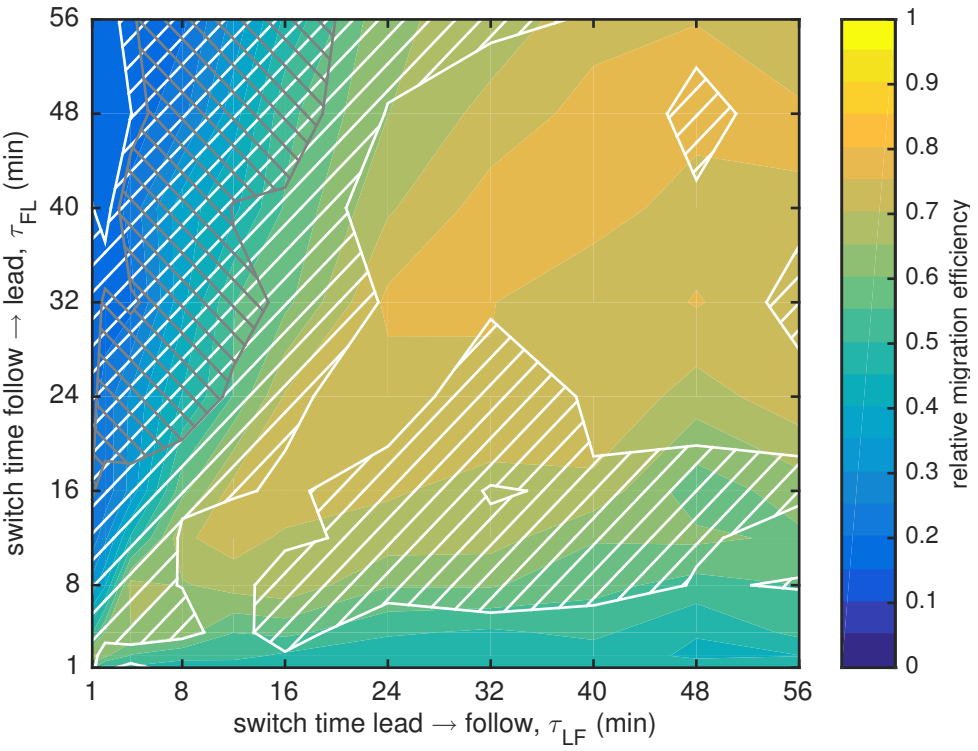

Figure 4.3: Effect of varying leader-follower switching times on model migration efficiency (average number of cells after t=24 hours over n=20 simulations), relative to the maximum for the non-switching case (as in Chapter 3.1). White hatched region shows greater than 20% coefficient of variation, grey hatched region greater than 30%.

4.3 Time-course gene expression analysis

Having implemented the integrate-and-switch mechanism in our computational framework for multicellular neural crest cell migration, we are now in a position to address how quickly neural crest cells change their migratory role. In the previous section, we investigated the effect of varying the switching time on migration outcome in the model. After this, we are still left with a free timescale parameter that needs to be constrained by experiments. Previously, it has been shown that neural crest cells have changed their gene expression 12 hours after transplantation (McLennan *et al.*, 2012), but prior to this study it was unknown how quickly the first response in change of gene expression occurred to changing environmental signals.

To answer this question and parameterise our model, we designed a series of timed experiments in which cultured neural crest cells were initially exposed to VEGF for 2 hours (Fig. 4.5), assuming this to be long enough for their gene profile to reach a steady state. VEGF was then removed by changing the medium and after 90 minutes

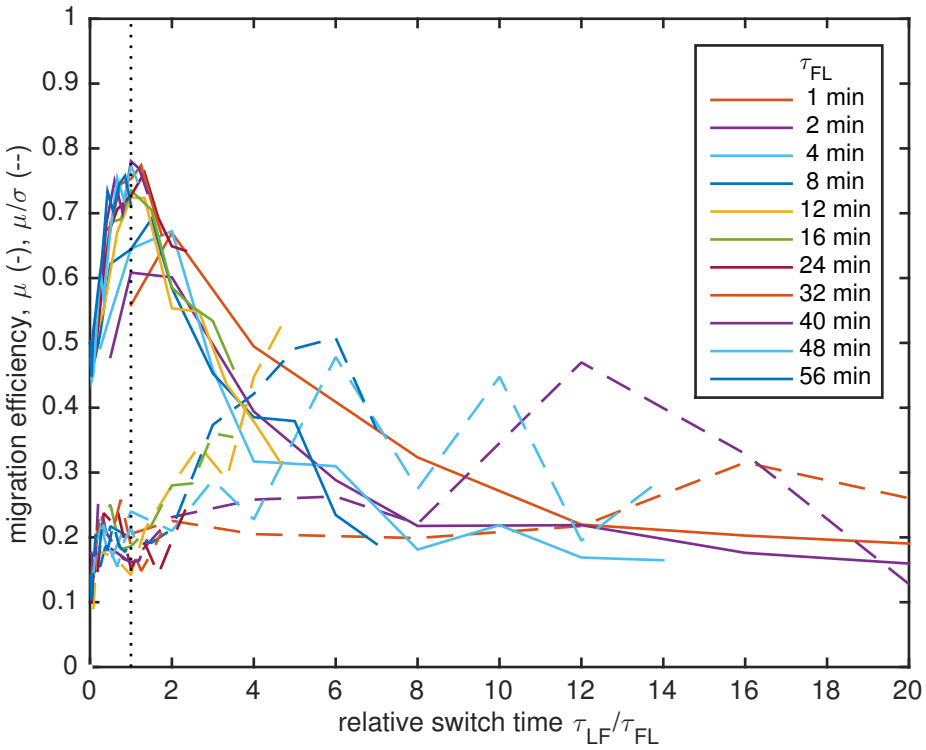

Figure 4.4: Migration efficiency (mean number of cells, μ; solid lines) and coefficient of variation (μ divided by standard deviation, σ; dashed lines) as a function of the ratio of switching times. The dotted line indicates $\tau_{\mathrm{LF}} = \tau_{\mathrm{FL}}$.

was re-applied (Fig. 4.5). We expected gene expression changes to occur within 90 min of changing the culture medium since *in vivo* observations showed trailing neural crest cells to divert to ectopic VEGF sources within one hour (McLennan *et al.*, 2015b). Cells were then taken from cultures for gene expression analysis at a set of time-points. Since we had no further prior knowledge of the timescale of gene expression, we spaced these time-points semi-logarithmically (rather than linearly) within the 90 minute interval. The non-linear spacing of measurement time-points turned out to be a crucial element of the experimental design without which we would have missed the surprisingly fast changes in gene expression (Fig. 4.6, 4.7).

Despite its name, quantitative gene expression data can be notoriously variable, even after normalising[2], as is common practice, for variability between samples based on stably expressed reference genes. Thus, we need to decide between signal and noise, for example by using statistical tests under a null model of no changes in expression. To combat the variability inherent within this biological system, our collaborators

[2]RT-qPCR data were normalised using three reference genes chosen from at least six candidates and analysed with Biogazelle's qBASE software (Hellemans *et al.*, 2007).

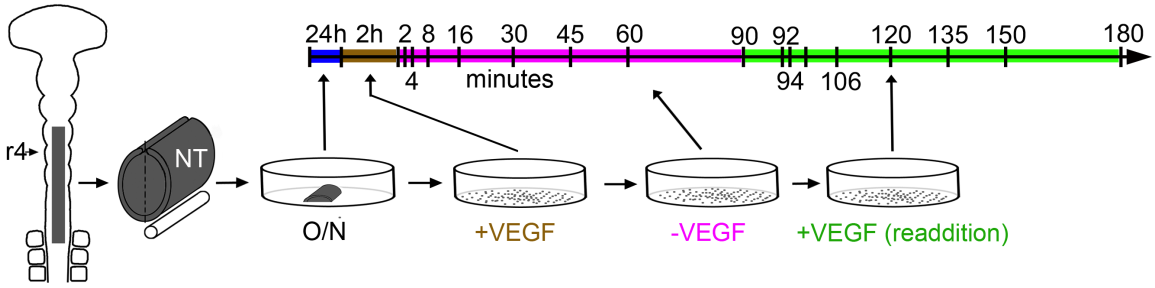

Figure 4.5: Schematic of experimental time-course to measure response of gene expression to removal and readdition of VEGF. Neural tube (NT) was explanted from chick embryo (left), and the neural crest cells cultured in medium containing VEGF. The medium was then changed after 2 hours to remove VEGF and again after 90 min to reintroduce VEGF, while cells were collected for gene expression analysis at the times indicated (time-axis not to scale). Reproduced from McLennan *et al.* (2015b) (with permission from Elsevier).

define genes to be differentially expressed using a t-test[3] at $p < 0.1$, choosing to include more potential genes of interest (than at the common threshold of $p < 0.05$). In lieu of multiple testing correction[4] to eliminate potential false positives, we focused on genes that were implicated consistently after both removal and readdition of VEGF (Fig. 4.6).

Of the 96 genes examined, 25 showed a change in expression after both removal and readdition of VEGF (Fig. 4.7), though the response times of individual genes varied within the 0 to 90 minute interval (Figs. 4.6, 4.7). The majority of those genes (17 out of 25) changed expression within four minutes of VEGF removal, while response to VEGF readdition was more broadly distributed (Fig. 4.7). Taken together, only six genes responded within 4 mins of both removal and readdition of VEGF.

[3]Using a Kolmogorov-Smirnov test (significance level $p < 0.1$) it was first verified that the replicates of the majority of genes was normally distributed, as required by the t-test. However, due to the limited number of replicates (between one and three per gene), the use of statistical tests for normality is limited. If one strongly questions the normality assumption, non-parametric tests could be used to determine differentially expressed genes. For consistency with the published work, we use the t-test here and provide alternative analysis in the appendix to this chapter.

[4]An alternative approach would be analysis of variance (ANOVA) for all genes to identify differentially expressed genes, followed by identifying samples (time-points) that are different from the baseline for each differentially expressed gene. These results can be found in the appendix to this chapter (Fig. 4.12, 4.13). While the exact set of genes identified is different (highlighting the dependence of results on appropriate statistical methods, and the subjective definition of significance), the overall conclusions about the timescales of first response in gene expression to changing VEGF conditions remain the same.

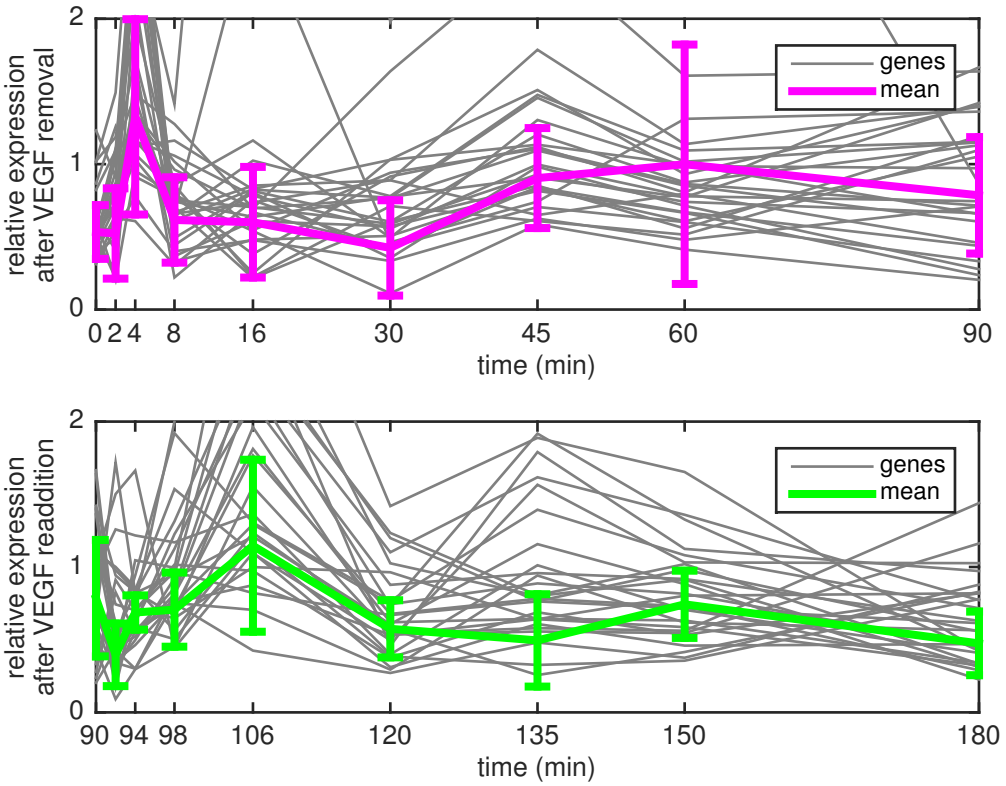

Figure 4.6: Transient response of all genes (grey lines, error bars omitted for clarity) that were differentially expressed ($p < 0.1$, t-test) at any time after *both* removal and readdition of VEGF, and their weighted mean (thick coloured lines), weighted by $1/\sigma_g$, where σ_g is the error in the mean of each gene (obtained from multiple replicates, and imputed for samples with only one replicate). Error bars show the weighted standard deviation of the (weighted) mean. Expression is relative to reference genes (see Hellemans *et al.*, 2007, for normalisation procedure).

The time-course signature of individual genes is consistent with the weighted average of all repeatedly differentially expressed genes, which shows a quick, transient response to a change in VEGF signal (Fig. 4.6). The transient nature of the response makes sense considering the step-change in culture conditions. Since the predominant response seems to be transient, one would not expect to see the same genes differentially expressed after the initial two-hour exposure to VEGF (no measurements were taken at finer temporal resolution within the first two hours). Furthermore, it is unclear what state explanted cells are in after being cultured for 24 hours, before being primed by two hours of exposure to VEGF. Thus, one would not necessarily expect the initial change in expression to be meaningful if the reference is not either. However, when considering this third constraint, i.e., taking genes that initially changed their expression, and did so again under removal and readdition of VEGF,

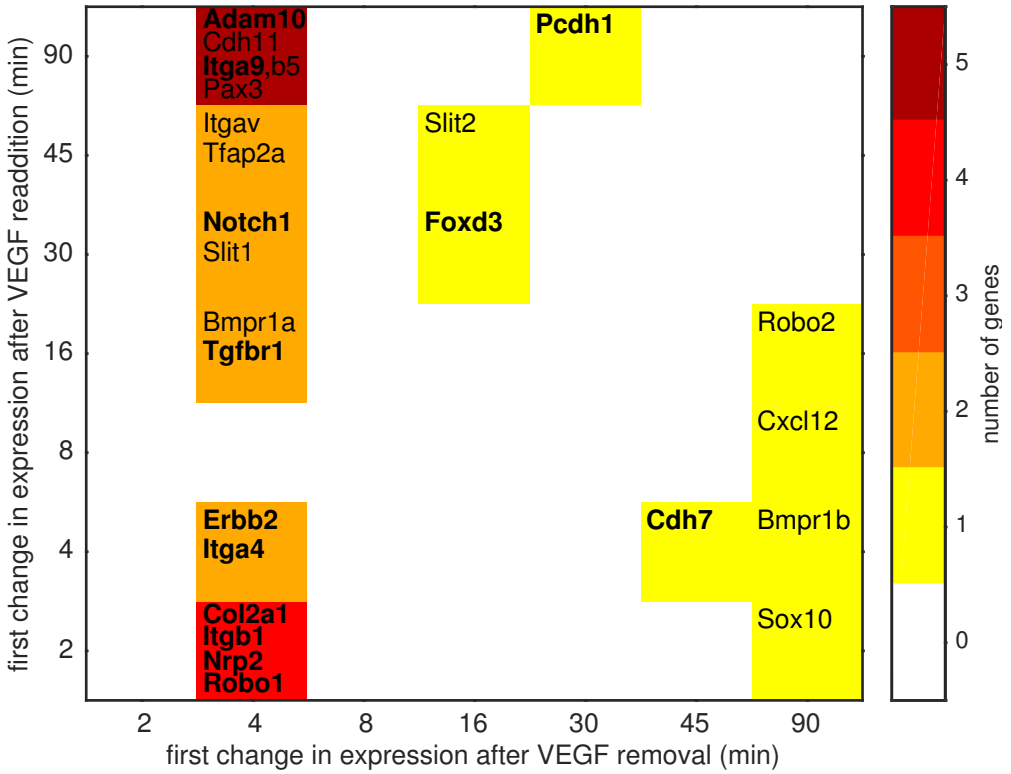

Figure 4.7: Summary of first response times of genes that showed differential expression (at any time-point) after removal (x-axis) as well as readdition (y-axis) of VEGF ($n = 25$ genes). Shown in bold are genes that also showed a change in expression after 2 hours of initial exposure to VEGF.

all six genes that respond within four minutes under both culture change conditions are still included (Fig. 4.7).

Instead of binning the first response times of individual genes, one might expect a profile of genes, e.g., a linear combination, to give a meaningful summary of the timescale of gene expression in response to VEGF. When we performed principal component analysis (Fig. 4.14, chapter appendix), with the suitable statistical tests for what trivial correlations are to be expected from a small data set (Fig. 4.15, chapter appendix), we again detected the rapid response times, but gained little insight that was different from the response of the mean of genes (as in Fig. 4.6).

The keen reader will have noted that in this *in vitro* experiment, differentially expressed genes downregulate in response to VEGF removal and upregulate after its readdition. This stands in contrast with the set of genes identified as a trailblazer molecular profile (Section 3.2.1.3), which were expressed more highly in single cells at the migratory front. The are two reasons for this apparent contradiction. First, this may come down to the differences between transient (*in vitro*) and steady-state

(*in vivo*) responses. This may be resolved by live-imaging expression of the identified genes. Secondly, we know that the two sets of genes are overlapping but non-identical (McLennan *et al.*, 2015b). This is to be expected, as there may be microenvironmental factors other than VEGF that are responsible for the trailblazer signature. However, it also highlights the limitation of culture experiments in a system like the neural crest where the complex native signals play a major role. Nevertheless, the experiment presented here should still give us sensible bounds on the basic timescale of gene expression responses to external VEGF signals, even if there are other relevant signals and a different set of gene responses in the more complex environment of the embryo.

Another limitation of the timed VEGF exposure experiment is the difficulty to distinguish whether the cells are responding to a gradient or absolute concentration of VEGF. According to the cell-induced gradient hypothesis, we assume cells are internalising VEGF and thus creating a gradient locally around them. To verify this experimentally, one could perhaps utilise a microfluidic set-up in which a concentration gradient can be precisely controlled, but this was beyond the scope of the present investigation.

4.4 Manipulating the chemoattractant distribution *in vivo* and computational experiments

Previous work has shown that neural crest cells in the front portion of a stream can respond to, and migrate towards, ectopic sources of VEGF placed within areas typically inhibiting invasion by neural crest cells (McLennan *et al.*, 2010). We hypothesized that trailing cells receive directional information through contact with (or proximity to) other cells, rather than the chemoattractant gradient. From transplantation studies, we expect these cells to be able to respond to VEGF signals in the absence of other cells to follow, but it is hitherto unclear what the hierarchy of environmental signals vs instructions from migrating neighbours is, and, if so how, trailing cells respond to ectopic sources of VEGF placed within or adjacent to the migratory stream. To address this, our collaborators performed an experiment in which they waited until lead neural crest cells had migrated from the neural tube and then placed ectopic sources of VEGF either adjacent to or within the trailing portion of the stream (Fig. 4.8B, C).

When a clump of cells overexpressing VEGF was placed next to the trailing migratory stream, neural crest cells rerouted towards the VEGF source (Fig. 4.8B, G,

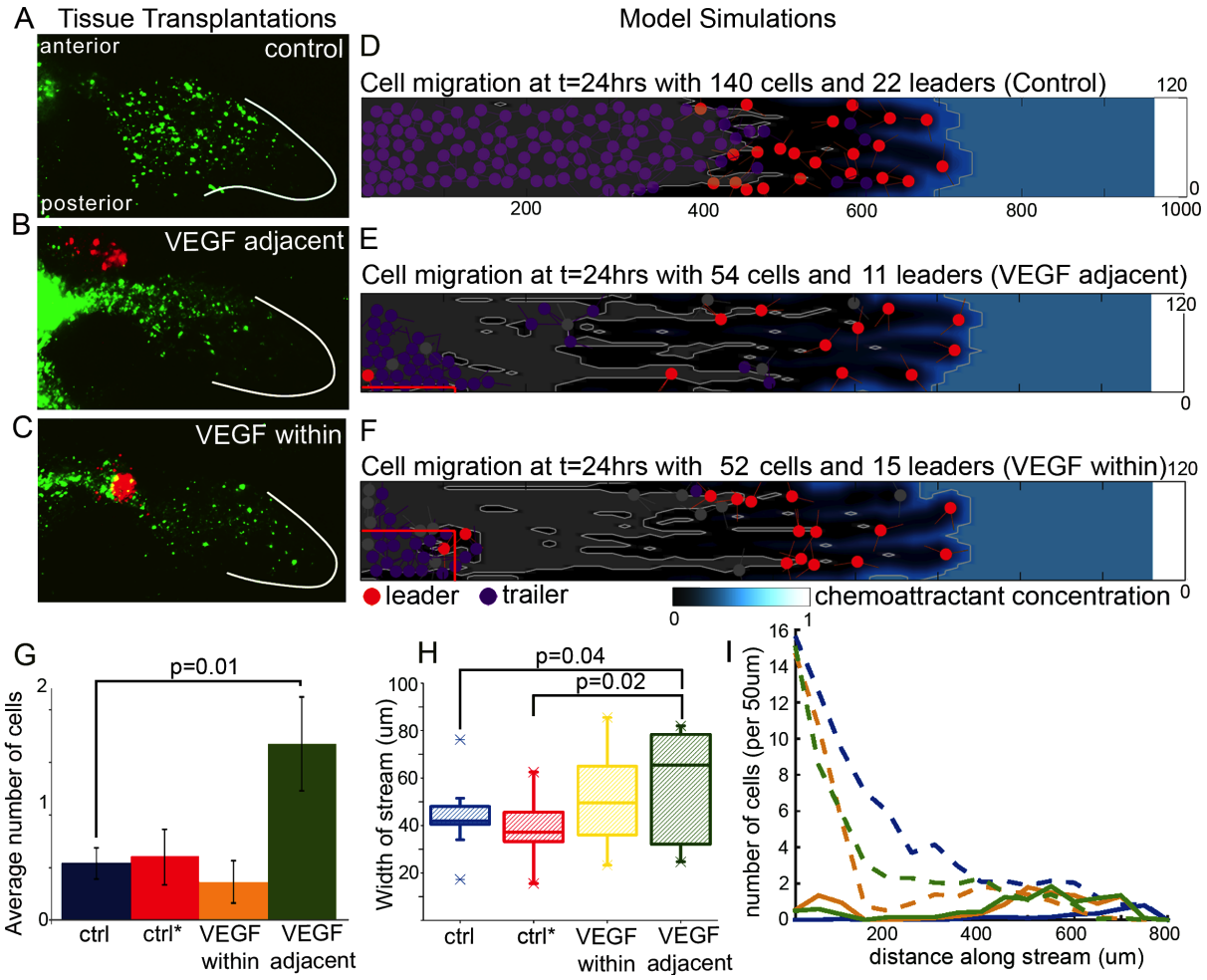

Figure 4.8: Altering the chemoattractant distribution perturbs migration. (A) Cranial neural crest stream (green) *in vivo*. (B) VEGF-expressing cells (red) were transplanted adjacent to trailing portion of the stream (green). (C) Ectopic VEGF cell transplant (red) placed within the trailing portion of the stream (green). (D-F) Representative model simulations of (D) the control experiment and (E,F) increased chemoattractant (CA) production at (E) bottom left edge of domain (marked by red line) and (F) bottom left area (marked by red line) from $t = 12$ hours onwards. (G) Average number of neural crest cells found in area adjacent to r3 (anterior to stream). Ctrl: control transplant (of non-VEGF expressing cells) within stream, $n = 18$ embryos; Ctrl*: control transplant adjacent to stream, $n = 18$; VEGF transplant adjacent to stream, $n = 12$; VEGF within stream, $n = 11$. (H) Width of stream at the transplant. (I) Histogram of cell number vs distance migrated in control and perturbed simulations, averaged over $n = 20$ realisations. Solid lines: leaders; Dashed lines: followers; Blue: Ctrl; Gold: VEGF within; Green: VEGF adjacent. Simulation parameters can be found in Table 3.1, and $\tau_{\mathrm{LF}} = \tau_{\mathrm{FL}} = 8$ minutes. Reproduced from McLennan *et al.* (2015b) (with permission from Elsevier).

H). No cells were attracted to control cells transplanted into the same region (McLennan *et al.*, 2010, 2015b). These trajectories were confirmed through cell tracking in time-lapse imaging (McLennan *et al.*, 2015b), which also showed that cells that did not leave the stream still had positions that clustered near the ectopic VEGF source. As a result, the stream width increased compared to the control transplant.

Similar results were observed when placing the VEGF transplant within the stream of migrating cells (Fig. 4.8C, H): Neural crest cells clustered around the ectopic VEGF source on both the proximal and distal sides of the source, while some tracked cells ahead of the transplant stayed behind and/or reversed their direction of migration (McLennan *et al.*, 2015b). The width of the stream was also increased when placing the transplant within the stream (Fig. 4.8H). This could be due to the transplant presenting a physical barrier to the migrating cells. However, migrating neural crest cells were found inside the transplant (Fig. 4.8C, and McLennan *et al.*, 2015b), suggesting the increase in width is at least in part due to increased local concentration of chemoattractant.

To test whether the observed effects of transplanting ectopic VEGF could be explained by our model with the integrate-and-switch mechanism, we computationally reproduced the tissue transplantation experiments (Fig. 4.8D-F). To represent transplants of ectopic VEGF in computational experiments, we altered the chemoattractant distribution in our model simulations. From $t = 12$ hours (6 hours after the start of migration), the background chemoattractant production was increased in a subregion of the migratory domain. To represent placement of a VEGF source outside of the domain (adjacent to the stream), the chemoattractant production was increased in a thin strip of 1/20th the width of the domain, and for placement within the stream, a region of half the domain-width was chosen. In both cases, the length of the transplant was 1/8th of the domain length, and the absolute length increased with domain growth. The integrate-and-switch parameters were set at $\tau_{\mathrm{LF}} = \tau_{\mathrm{FL}} = 8$ minutes.

In the region of increased chemoattractant production, model simulations showed that a greater proportion of trailing cells switched to become leader cells than in the control simulations (Fig. 4.8E,F). This clustering of cells around the transplants resulted in a break-up of the stream into two separately moving subpopulations (Fig. 4.8E,F), and was consistent across repeated simulations (Fig. 4.8I). Thus, the effects of perturbing the VEGF distribution *in vivo* are consistent with our cell-induced gradient model with VEGF-induced cell state transitions according to the integrate-and-switch mechanism.

4.5 Effect of total population size and density

Having established the consistency of our model for phenotypic plasticity with the experimental observations, we can attempt to make predictions to be tested experimentally in future work. If migrating neural crest cells rely on contact with, or proximity to, their neighbours to obtain directional information in the trailing portion of the stream, then the migration should be affected when cells are more spread out, i.e., at lower population density. We can imagine two possible outcomes: either the streaming migration would become less directed, as communication of directional information (e.g. through contact guidance) becomes more sparse; or the population would compensate by increasing the number of leaders, for example because the required chemoattractant gradient is degraded less at lower density of sinks (cells). Note that this section includes model predictions that have not yet been tested experimentally, in part due to the technical difficulty of the experiment, and hence not used in the associated publication.

Previously we quantified migration outcomes by the number of cells in the domain at $t = 24$ hours, averaged over repeated simulations. If we are to perturb population density, this summary statistic becomes uninformative. We can, however, use the number and/or fraction of cells that are in the leader state as a measure to check whether the collective migration mechanism has compensated for lower population density. Before we do this, let us verify how leader fraction and number depend on our newly introduced parameters of state transition rates, or switching times τ_{LF} and τ_{FL}. We already saw that varying these parameters affects migration efficiency (Fig. 4.3, 4.4) and thus, by definition, the number of cells. We may further expect that the number of cells in a leader state is an increasing function of the lead-follow transition time, τ_{LF}, and a decreasing function of the follow-lead transition time, τ_{FL}. Our intuition is confirmed by simulation results (Fig. 4.9). We can also verify that our choice to parameterise the switching time at $\tau_{\mathrm{LF}} = \tau_{\mathrm{FL}} = 8$ minutes (to allow for translation time, assumed to be on the order of transcription time) gives rise to a leader fraction just above 10%, close to the optimal migration outcome found in Chapter 3.

To explore the effects of perturbing the population density, we can vary the rate at which cells enter the domain in our computational experiment. As not every attempt to insert cells is successful (due to volume exclusion), we cannot control the final cell number in our stochastic simulation precisely. Nevertheless, sweeping over a range of insertion rates (such as every time-step, every other time-step, etc.), results in a

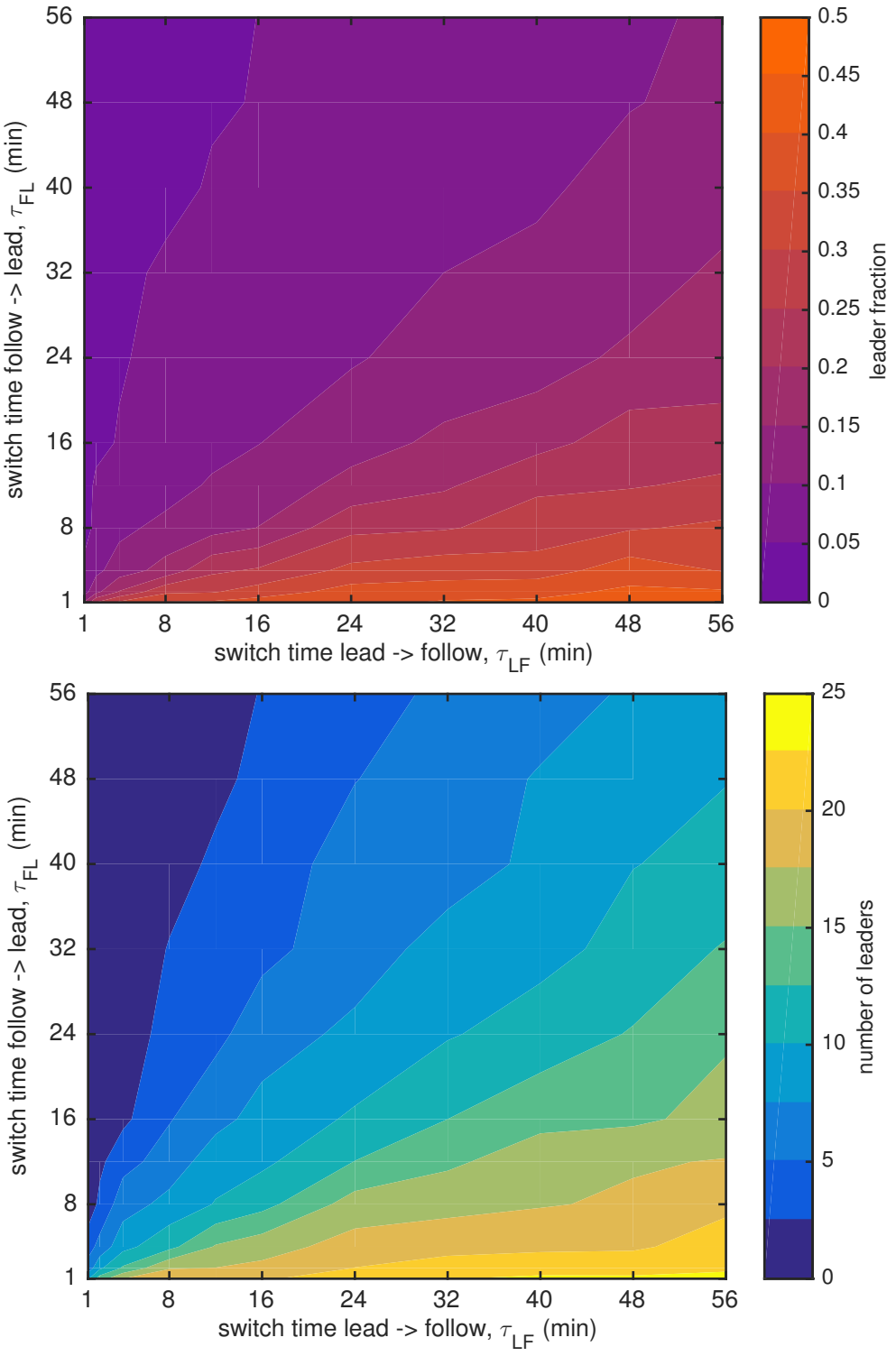

Figure 4.9: Both the fraction and absolute number of cells in a leader state depend on the combination of state switching times. Other simulation parameters can be found in Table 3.1.

range of final cell population sizes for which we can compute the emergent leader number and fraction. The results show an increase in leader fraction with decreasing population size (Fig. 4.10). Perhaps counter-intuitively, the absolute number of cells in a leader state (at $t = 24$ hours) stays constant as a function of total number of cells (Fig. 4.10). *In vivo*, this prediction could potentially be tested by removing part of the neural tube in such a way as to reduce the number of cells delaminating per unit time.

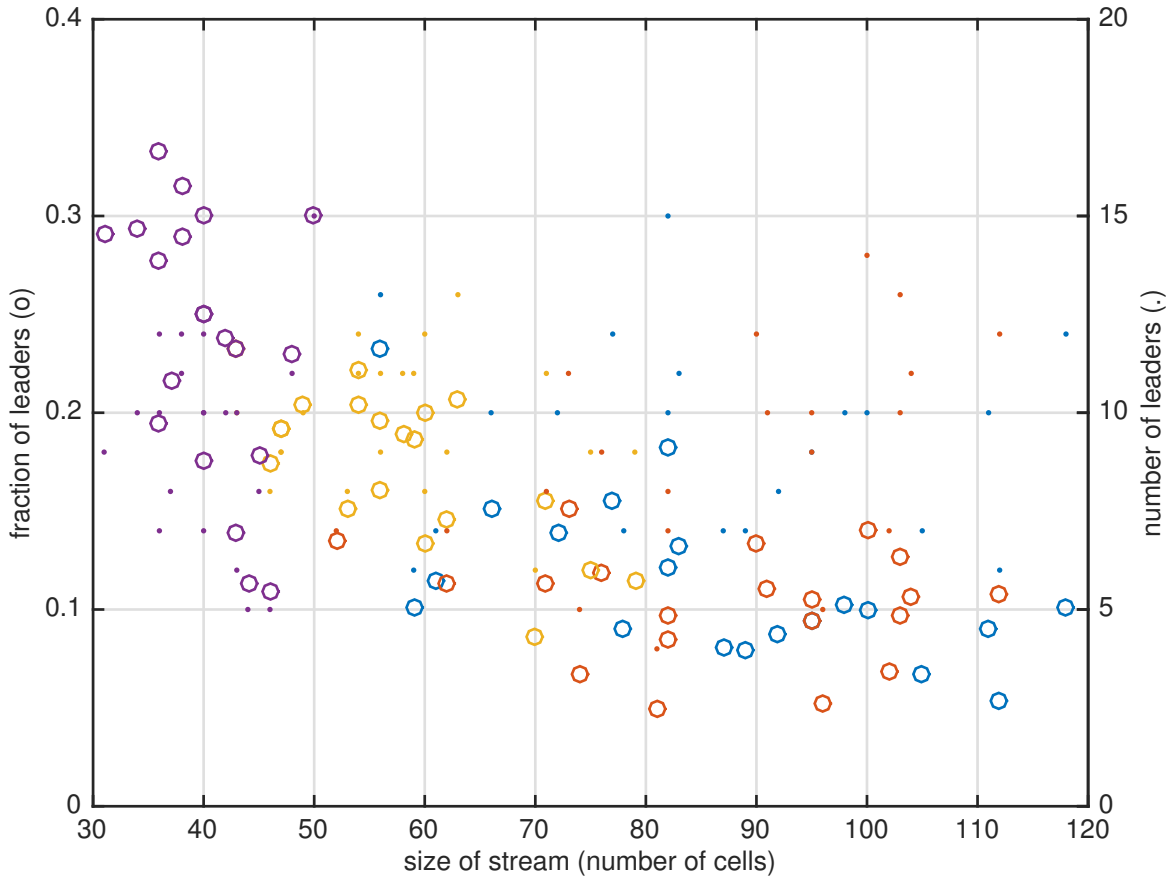

Figure 4.10: The fraction of cells in a leader state (circles) at $t = 24$ hours depends on the total number of cells in the stream, while the absolute number of leaders (dots) is less correlated with stream size. Different colours show data from different cell insertion rates: blue, attempt every to insert a cell every time-step; orange, every third time-step; yellow, every 12 time-steps; purple, every 24 time-steps. Cell number saturates at high insertion rates as the domain becomes densely packed. A control simulation has an attempted insertion rate of every 6 time-steps (not shown).

As the size of the migrating cell population decreases, we observe an increasing fraction of cells in a leader state. This phenomenon is also observed in models of col-

lective behaviour of groups of animals that display leadership behaviour in consensus finding (Couzin *et al.*, 2005), where "the larger the group, the smaller the portion of informed members is needed, in order to guide the group towards a preferred direction" (Vicsek and Zafeiris, 2012).

4.6 Discussion

In this chapter, we explored the role of cell-environment interactions in creating and maintaining the population heterogeneity that guides migration. Specifically, we investigated the hypothesis that the presence of a directional signal in the form of a chemoattractant (VEGF) gradient induces a neural crest cell to be in a leader state. Starting from a minimal model of phenotypic plasticity, which we termed integrate-and-switch mechanism (Section 4.2), we then devised an experiment together with our collaborators to assess the timescales of gene profile responses to a directional signal (Section 4.3). Timed addition and removal of VEGF in neural crest cell culture (Fig. 4.5) showed gene expression changes within minutes (Fig. 4.7) and guided the parameterisation of our new integrate-and-switch mechanism for leader-follower transitions in our computational model. Model simulations further showed that migration efficiency is highest when the timescales of switching into and out of a leader state are equal (Fig. 4.4). Together, these results constrained the choice of timescale in complementary ways: The histogram of gene expression changes after VEGF removal was tightly peaked around four minutes, but not so for changes following readdition of VEGF. But here the model simulations showed lowest overall migration efficiency (and highest variability) for slow follow-lead transition rates (Fig. 4.7), suggesting fast state switching times.

To test our thus implemented model, we perturbed migration and compared simulations with *in vivo* experiments. Transplantation of ectopic VEGF sources altered cell trajectories and gene expression (McLennan *et al.*, 2015b), consistent with perturbation of the chemoattractant distribution in our computational experiments (Fig. 4.8). In accompanying experiments, VEGF was knocked down in either the ectoderm overlaying the trailing portion of the stream (to reduce VEGF production) or the mesoderm (to bind up existing VEGF protein), and there was no effect on trailer neural crest cell migration (McLennan *et al.*, 2015b), confirming our model assumption that VEGF signals are not required for the guidance of trailing neural crest cells, which instead may rely on cell contact, secondary cues secreted by leader cells, extracellular matrix modifications, or unknown microenvironmental signals for

guidance. We conclude that microenvironmental signals including, but not necessarily limited to, VEGF, induce a leader cell state in chick cranial neural crest cells.

Limitations of previous model implementations (McLennan *et al.*, 2012, Dyson, 2013) led us to consider two model features that made migration more realistic and more robust to intrinsic variability (Section 4.1.1), namely: (1) a non-zero timescale of switching between leader and trailer cell states; and (2) hysteresis, or a memory that decays with time, of the signal sensed (the directional cue). Thus, the integrate-and-switch mechanism, as presented here, provided the simplest extension to our existing model that captured the plasticity of neural crest cell behavioural identity and did so robustly. It is important to note that the integrate-and-switch mechanism in fact makes our model of neural crest cell migration less complex (compared to Chapter 3), in the sense that the size of the lead subpopulation does not need to be pre-specified, but emerges from the interactions of the cells with the chemoattractant distribution.

We characterised how the emergent leader subpopulation depends on the dynamics of state transitions (Section 4.5). We found that larger cell groups have a lower leader fraction, a familiar result from the study of collective animal movement. Thus, despite the fairly specialised migration setting with its constrained environment, there is an enticing possibility, speculative as it may be, of universal principles governing collective migration generally, independent of the scale and complexity of its agents.

In summary, our findings identify the importance of VEGF as one of the microenvironmental signals that establish a distinct subpopulation of neural crest cells in a leader state. These data support our cell-induced gradient model in which microenvironmental signals define and direct leading neural crest cells that instruct others to follow (though we note the mechanistic nature of this instruction remains hypothetical). Furthermore, we add to the growing body of evidence for guidance of cell populations through different cell states induced by microenvironmental factors (Rørth, 2012, Haeger *et al.*, 2015), such as in *Drospohila* border cell (Inaki *et al.*, 2012) and zebrafish lateral line migration (Revenu *et al.*, 2014). We have implemented an integrate-and-switch mechanism in our computational model, through which neural crest cells adopt leader and follower states, with non-zero timescale and hysteresis of exposure to a directional signal. So far, this model is consistent with the observed cell persistence and stream cohesion in the chick cranial neural crest. Further detailed analyses of the cell behaviours and gene expression changes in migrating neural crest cells may help to elucidate the mechanistic underpinnings by which cells instruct others to follow and how the leader-to-follower cell state transition is regulated at a molecular level. Going forward, efforts in improving the quality of the data

to distinguish and rule out existing competing hypotheses may be more rewarding than considering more complex models. Exploring further how microenvironmental signals determine cell migratory states has the potential to elucidate many more riddles in developmental biology, such as the example of trunk neural crest cells that, after having reached their target sites, resume a secondary phase of migration and chemotactically interact with growing sympathetic nerves (Kasemeier-Kulesa *et al.*, 2015).

Chapter appendix

Migration profiles under variation of switching times

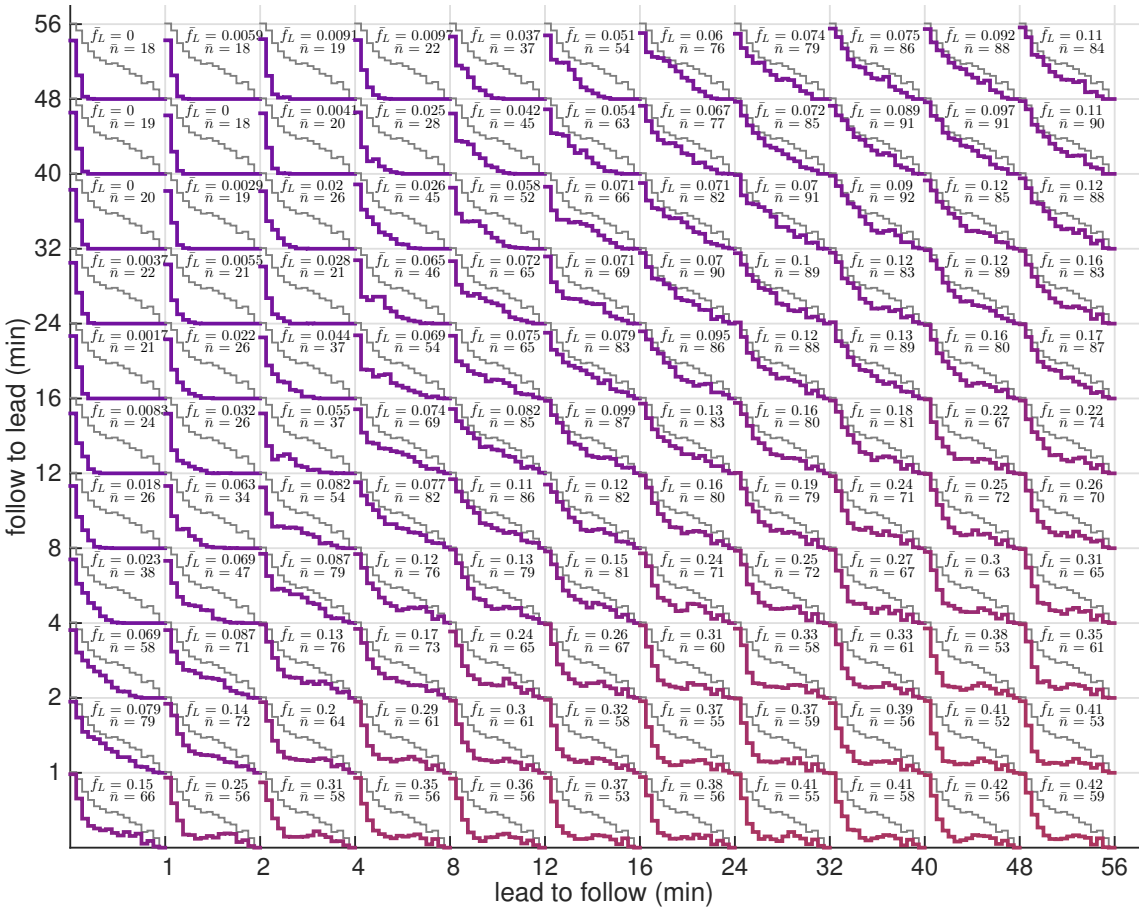

Figure 4.11: Effect of leader-follower switching times on migration outcome. For each parameter combination, the histogram of cell number vs distance migrated is shown (averaged over $n = 20$ realisations), including the average leader fraction $\bar{f}_{\mathrm{L}}$ (which also determines the colour) and number of cells in the stream $\bar{n}$. Grey histograms are guides to the eye and show the non-switching case. Same data as in Fig. 4.3.

Analysis of variance for each gene

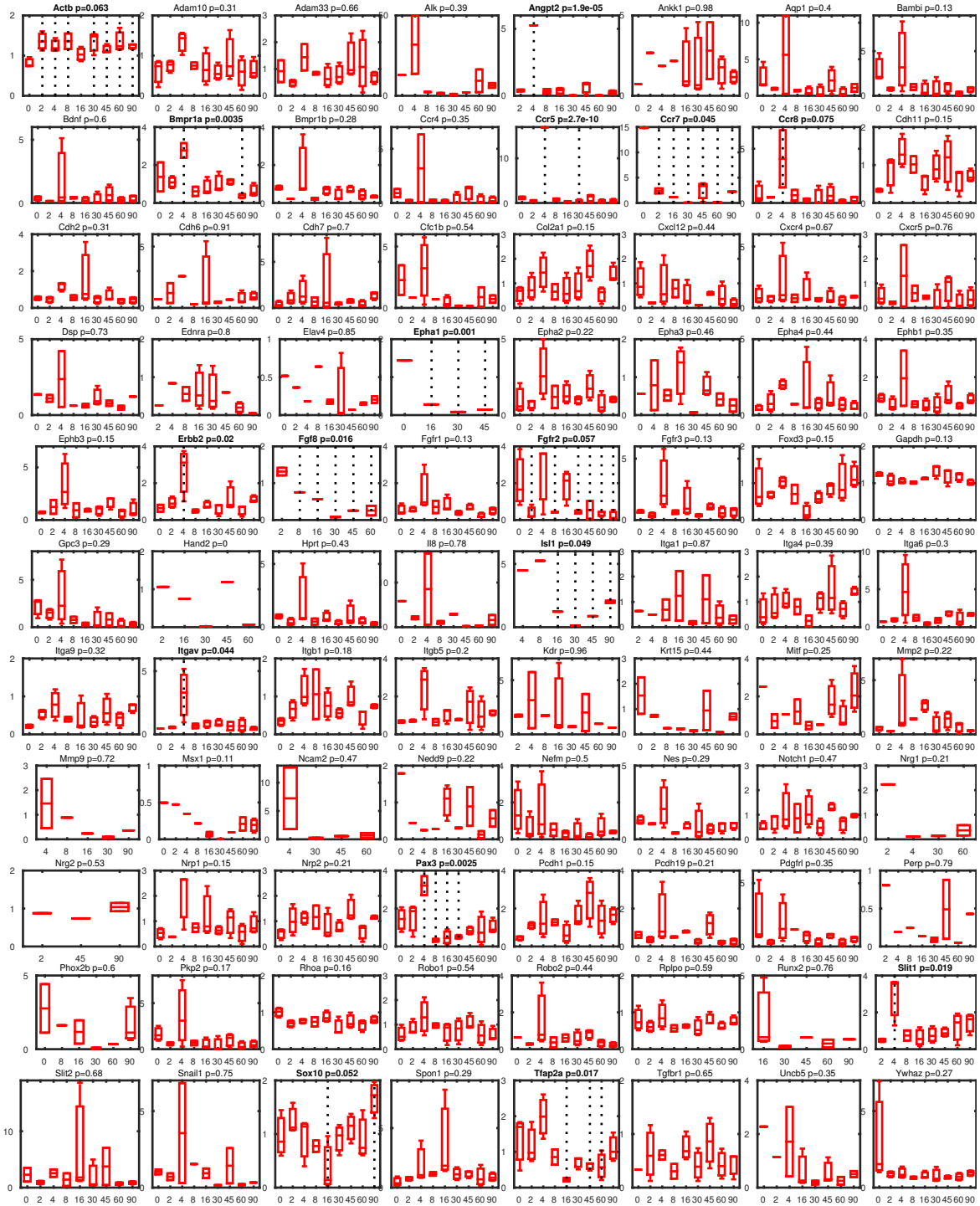

Figure 4.12: ANOVA for each gene measured in response to removal of VEGF (Fig. 4.5). Box plots show expression at each time-point. Differentially expressed genes (at $p < 0.1$) are highlighted in bold. Within these, individual time-points that are different from the first ($p < 0.1$, t-test) are indicated by dashed lines.

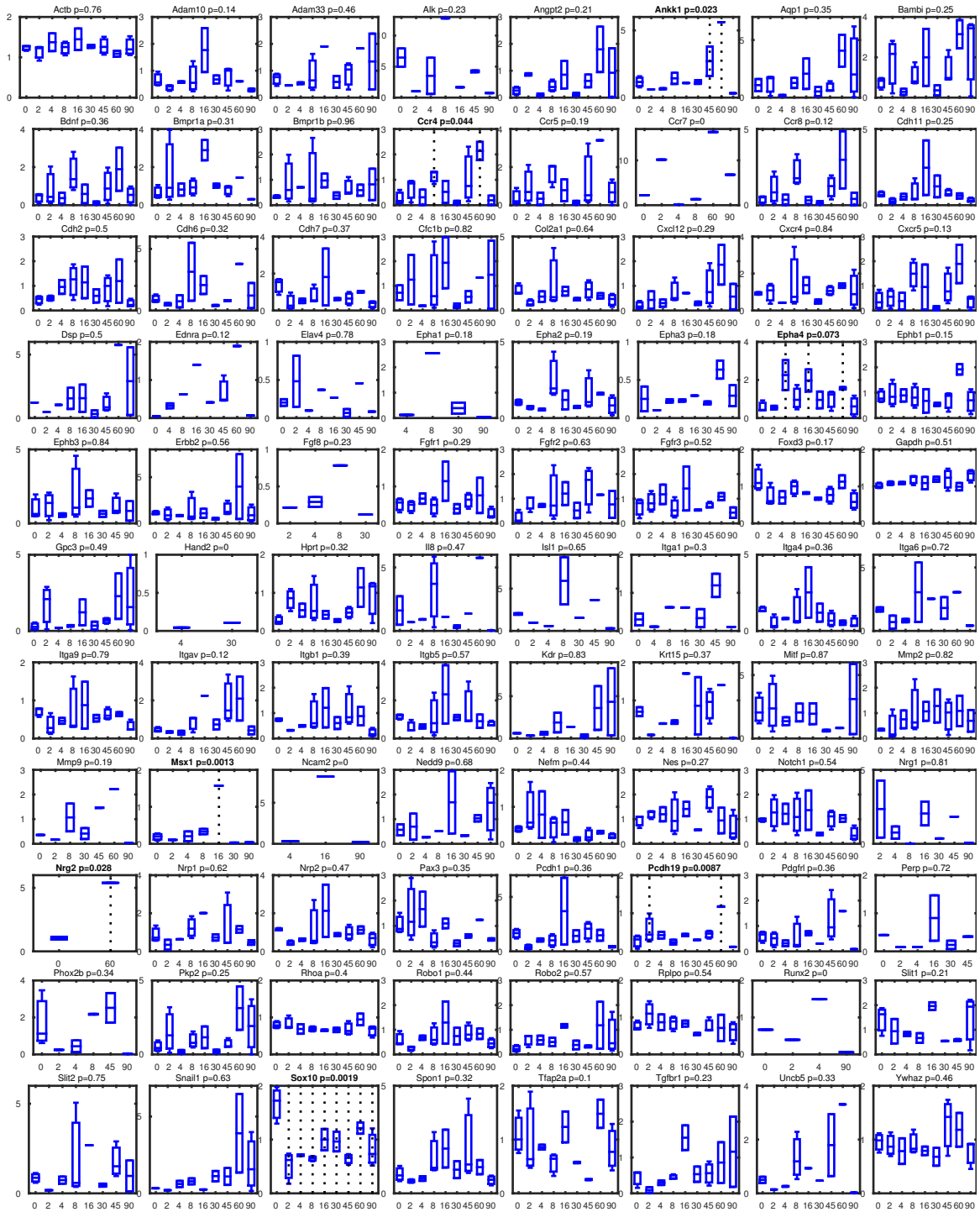

Figure 4.13: ANOVA for each gene measured in response to readdition of VEGF (Fig. 4.5). Box plots show expression at each time-point. Differentially expressed genes (at $p < 0.1$) are highlighted in bold. Within these, individual time-points that are different from the first ($p < 0.1$, t-test) are indicated by dashed lines.

Principal component analysis

Instead of checking the time-course of each (differentially expressed) gene, we can ask whether a combination of genes, i.e., a profile, gives a clearer picture of the timescale of gene expression changes. To this end we use principal component analysis[5] of the time-series of differentially expressed genes. Due to the very limited size of our data set, however, we need to be careful not to over-interpret the principal components, as small time-series can give rise to correlations (between genes) more easily by chance. To check this, we can utilise results from random matrix theory to check for the distribution of eigenvalues of the correlation matrix and the distribution of the components of the eigenvectors (Laloux *et al.*, 1999). These results hold in the limit of infinite matrix size, and although finite size corrections exist, for a very small data set it may be most practical to estimate the distribution of eigenvalues by re-shuffling each time-series many times (Plerou *et al.*, 2002), randomising the expected correlations. Such techniques have been used in models of financial markets (Laloux *et al.*, 1999, Plerou *et al.*, 2002) with incredible (monetary) success, but to our knowledge are rarely used for null-models of correlations in biologically applied PCA (a notable exception being Klein *et al.*, 2015, where we first learnt about these methods).

The statistical checks on our PCA reveal only the first two to three eigenvalues are occurring above chance, but only the first eigenvector's components are distributed non-normally (Fig. 4.15). Inspecting the time-course of the first principal component in each experimental condition (Fig. 4.14), we see that it reproduces the timescales extracted from our more basic summary of response times, but also that it is not suitably different from the mean of the genes to obviously give us any more information (even though the loadings are non-uniform).

[5]Principal component analysis (Pearson, 1901) is an orthogonal transformation of the data into a set of basis vectors called principal components (PCs) such the data have the largest possible variance along the first PC, then the second PC, etc. The PCs are the eigenvectors of the covariance matrix of the data. For alternative answers to the question "What is principal component analysis?", see `https://liorpachter.wordpress.com/2014/05/26/what-is-principal-component-analysis/`

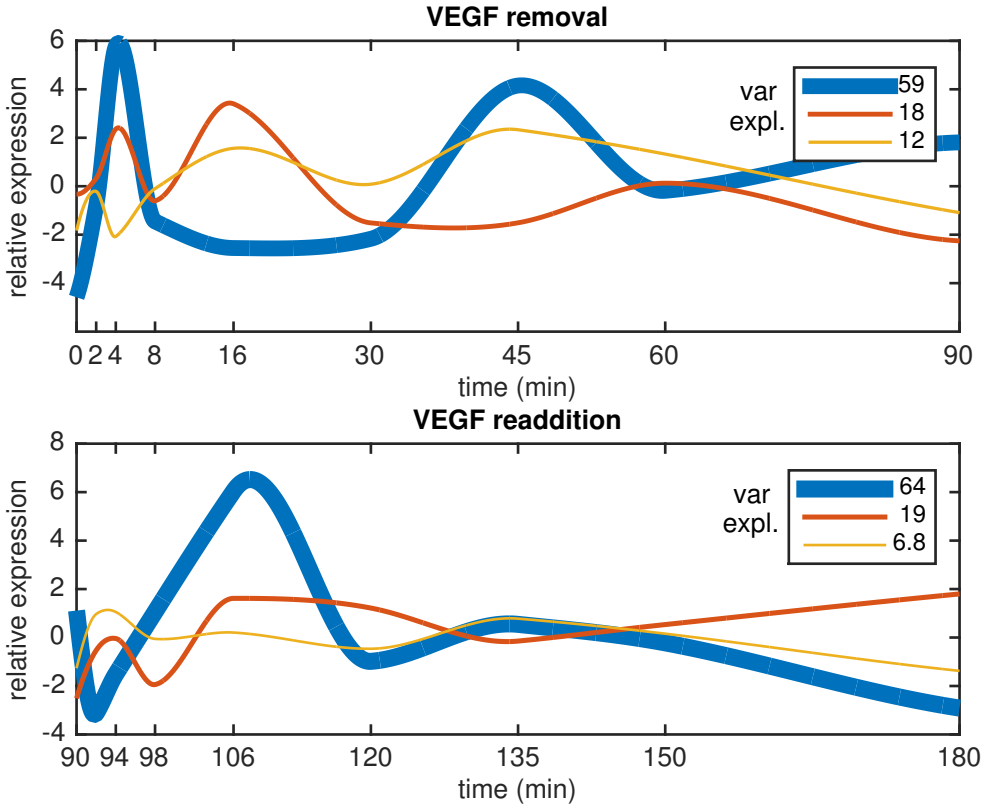

Figure 4.14: First three principal components for genes differentially expressed after initial exposure, removal and readdition of VEGF. Traces have been smoothed by Akima interpolation (Akima, 1970). Line thickness is proportional to the percentage of variance explained by each principal component.

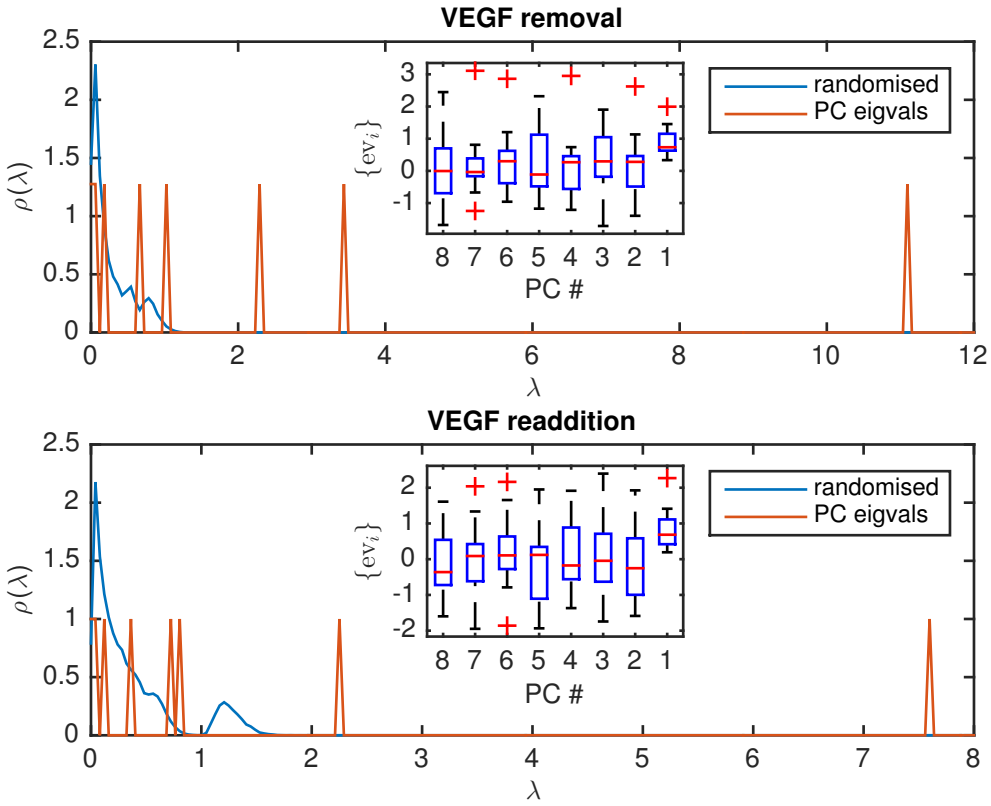

Figure 4.15: Distribution of eigenvalues λ (main plot) and normalised eigenvector components (inset) associated with the PCA (Fig. 4.14) of genes differentially expressed after initial exposure, removal and readdition of VEGF, compared to the null model based on random matrix theory. For the eigenvalues, a randomised distribution was built by shuffling the time-series for each gene 10^4 times (Plerou *et al.*, 2002, Klein *et al.*, 2015). The each eigenvector, $\mathbf{ev}$, of length N, the components, $\{\mathrm{ev}_i\}$, were normalised to $\sum_i \mathrm{ev}_i^2 = N$, and then their distribution was compared to a normal distribution of zero mean and unit variance (Laloux *et al.*, 1999). In both conditions, only the first eigenvector's components were distributed non-normally (Kolmogorov-Smirnov test $p \leq 0.0001$).

Chapter 5

Skin cell self-organisation – a clustering of clusters?

In the previous two chapters, we explored how population heterogeneity and cell-environment interactions contribute to the phenomenology of collective cell migration in neural crest cells. A third theme we set out to explore in this thesis is that of cell-cell interactions. To make progress on this front, it is useful to disentangle emergent behaviour arising from environmental signals and intercellular interactions. An opportunity for this is provided by *in vitro* systems that display realistic tissue-level organisation, such as organoids (Sasai *et al.*, 2012, Gjorevski *et al.*, 2014, Linnemann *et al.*, 2015) or micromass culture (Lee *et al.*, 1998, Havlickova *et al.*, 2009, Lee and Chuong, 2009, Lee *et al.*, 2011). In this chapter, we thus turn to a different biological system to explore mechanisms of cell self-organisation without directional migration guided by the embryonic microenvironment. We continue to work at the cellular scale, and consider signals and interactions between cells. The broad question that we wish to address is: How do cells self-organise into complex tissue structures, and what path do they take to get there?

To this end, we focus on a tissue engineering experiment, comprising a skin reconstitution assay in which skin cells from newborn mice are dissociated, mixed and incubated in culture. These cells then separate into two tissue layers in a way that is reminiscent of tissue organisation *in vivo*, which makes the culture suitable for transplantation. The transplanted skin patch grows new hair, even if transplanted into genetically hairless mice. We aim to understand the initial self-organisation of cells into epidermal and dermal components, described in more detail in Section 5.1, using mathematical descriptions and quantitative data analysis.

The outline of this chapter is as follows: First, we describe details of the experiment in Section 5.1 and introduce the types of data with which we are working.

In Section 5.2, we introduce relevant theory from the literature on aggregation processes. We then apply this description to cell-cluster counts and validate it in three ways: direct fitting of analytical and numerical solutions of Smoluchowski coagulation equations to cell-cluster size distribution data, scaling analysis and collapsing of distribution functions. Finally, in Section 5.3 we summarise the limitations of the data and our theoretical approach, discuss the suitability of alternative descriptions to explain tissue phase-separation, and conclude by commenting on further theoretical work and suggestions for experiments.

External contributions Experimental data in this chapter have been provided by the Chuong Lab at the University of Southern California. All experiments were performed by Mingxing Lei under the guidance of Cheng-Ming Chuong. Automated tracking of microscopy videos was performed by Mingxing Lei with assistance from the author of this thesis.

5.1 Overview of experiment: Skin reconstitution assay

In this section, we describe imaging data on the self-organisation of mouse skin cells into tissue layers and hair roots. Our collaborators conducted experiments in which two types of skin cells (dermal and epidermal) taken from mice were dissociated and mixed, then incubated in culture (see Fig. 5.1). Several stages of reorganisation can be observed, from the initial separation of epidermal cells into clusters that grow over time (Fig. 5.1, six hours to two days), through the formation of internal cavity-like structure within large clusters (Fig. 5.1, day two to three), to the merging of these clusters (Fig. 5.1, day four) into a separate tissue layer (not shown) which forms the outer layer of skin (epidermis). Thus, the tissue reconstitutes itself and forms skin *in vitro*. These cell cultures have the ability to grow hairs upon reimplantation into otherwise genetically nude mice.

This experimental assay demonstrates the potential of self-organisation to drive tissue morphogenesis. Unravelling the mechanisms underlying this self-organisation phenomenon has the potential to inform not only applications in tissue engineering, but also our understanding of the *in vivo* development of these tissue structures. By determining to what extent cells passively follow physical driving forces, versus how much they actively control their properties in response to signals to direct their path through "tissue phase space", we may translate insights from this work to different

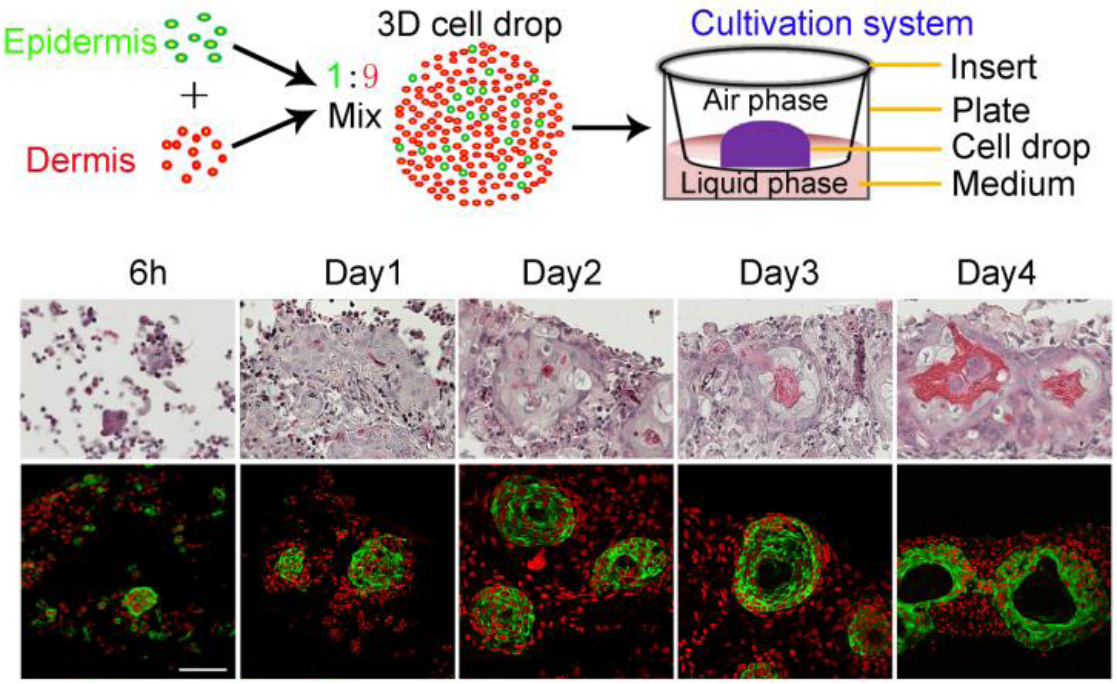

Figure 5.1: Schematic of experimental assay (top), stained histology sections (middle) and fluorescently labelled microscopy images (bottom). Epidermal cells are labelled in green, while red fluorescence marks all cells (epidermal and dermal). Figure adapted by the author from a version created for publication by Mingxing Lei, Chuong Lab (unpublished).

culture conditions, or even to the dynamic conditions of the growing embryo. Thus, we can hope to predict how the efficacy of tissue structure formation can be affected, e.g., by changing the ratio of epidermal to dermal cells or by molecular functional perturbation of cell motility and interactions.

We choose to focus on the clustering of epidermal cells during the first few days after mixing. We observe that clusters of epidermal cells grow and eventually reach a size that appears to be stable, or at least growing more slowly. Our hypothesis is that these clusters initially grow through random collisions and coagulation, before some size-regulatory processes take over. We will refer to the extensive literature on aggregation processes in the physical sciences to draw on for testing this hypothesis. We show that the evolution of the cluster size distributions is consistent with the dynamics of "clustering clusters" (Botet and Jullien, 1984, Kolb, 1984), an aggregation process in which clusters themselves undergo diffusion and merge upon collision. This is in contrast to other coarsening mechanisms, such as diffusion-limited aggregation or Ostwald ripening (Pototsky *et al.*, 2014), in which immobile clusters grow through the absorption and exchange of monomers, respectively, or spinodal decomposition,

where the phase separation occurs everywhere at once.

5.1.1 Cell-cluster size distributions

The theoretical descriptions we are considering make predictions on the changes in the numbers of clusters of a certain size over time. To compare these with cell cluster formation *in vitro*, the frequency of epidermal cell clusters and their sizes during the first three days of the experiment were counted[1] in microscope images by Mingxing Lei from the Chuong Lab and binned into a histogram (Fig. 5.2). At $t = 0$ hours the cells are dissociated and assumed to be only present as single cells (monomeric clusters). The number of large clusters increases with time, while the number of monomers and small clusters decreases. At 48 hours (Fig. 5.2), the frequency distribution exhibits a peak, indicating that the cell clusters may have reached a stable size. The peak shifts to a smaller cluster size at 72 hours. This shift might not represent a decrease in the actual size of the most frequent clusters, but likely is a result of differentiation and death of cells at the centre of clusters (see Fig. 5.1), causing them to lose their fluorescent labelling and drop out of the counts.

As we show in Section 5.11, the emerging peak in the cluster size counts changes the characteristic shape of the distribution. This indicates a change in the aggregation dynamics. Therefore, we initially aim for a description of the first 36 hours of the aggregation process only, and consider what might regulate cluster size in Chapter 6. For the early stages, we hypothesise that the cells cluster like randomly moving, irreversibly coagulating particles. This is undoubtedly a huge simplification (or wrong, like all models; Box, 1976), but we proceed with this approximation to see how far it may be useful. But first, let us pre-emptively check two assumptions we will make use of, that total cell numbers are constant over time (Section 5.1.1.1) and that cells are moving randomly on the timescales of observation (Section 5.1.2).

5.1.1.1 Assumption of constant cell numbers

The models of clustering clusters we use in Section 5.2 assume constant particle (or cell) numbers. This assumption does not hold in the dataset used here (Fig. 5.3), for three reasons. First, we omit clusters of size one and two in the counting data. These merge with larger clusters and thus enter the cluster size count at later times, giving an

[1]Method: The number of cells in aggregates was counted in representative Z-stacks at 40× magnification, and the number of aggregates were counted at 10× magnification. Aggregate sizes were collated in bins of 50 cell width. Aggregate growth through proliferation was observed to be low (approx. 1%) and deemed negligible.

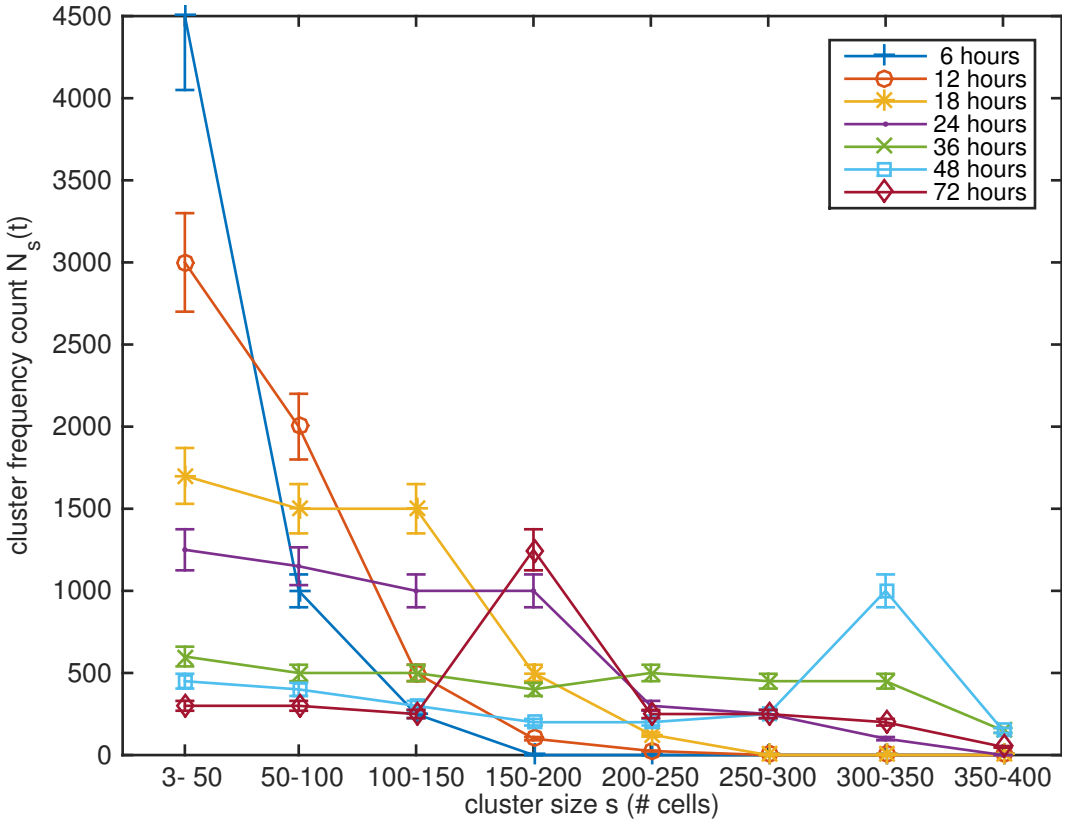

Figure 5.2: Epidermal cell-cluster size distributions, obtained from microscope images by Mingxing Lei, Chuong Lab. We have omitted clusters of size one and two from the analysis, to avoid possible issues due to incomplete labelling, mislabelling or less accurate counting of dissociated cells. Error bars are estimated as 10% counting accuracy.

apparent increase in total cell number. Secondly, visually estimating the cell numbers from microscope images can be especially error-prone for single cells, and the droplet volume in which cells were counted may vary over time. Thirdly, cell numbers may not be exactly constant due to proliferation, apoptosis and differentiation into other cell types, which can cause cells to lose the cell-type specific fluorescent labelling. While cell division was rarely seen in the experimental assay, apoptosis and differentiation was observed particularly at the centre of clusters from 48 hours onwards (Fig. 5.1), which may explain the apparent decrease in cell number from 36 to 72 hours.

One can attempt to fix this by rescaling cluster numbers at different times in proportion to the different cell counts. The number of clusters of size s at time t, $N_s(t)$, then becomes $N_s(t) \times \max_i(N(t_i))/N(t)$, where N is the total cell number, and i indexes the data sets from different time-points (six to 72 hours). This is a grossly simplistic way to address the problem. However, it only affects the results when

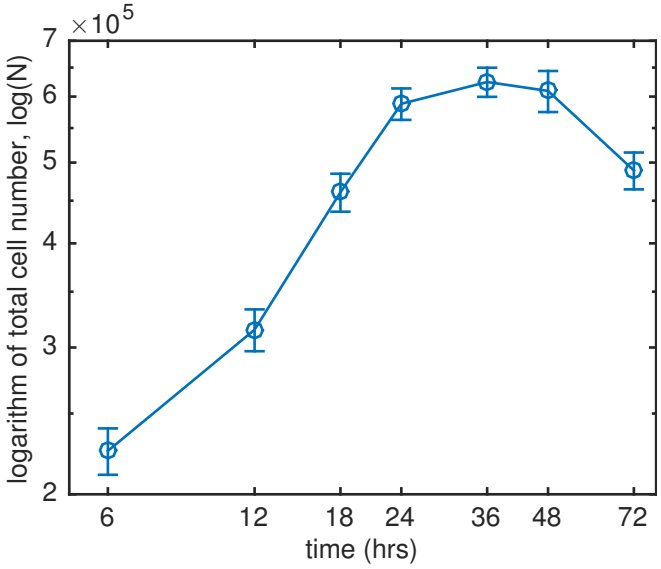

Figure 5.3: Total cell number in estimated cluster size distributions (Fig. 5.2) is not constant. The errors were calculated from estimated 10% cluster count accuracy and a cluster size uncertainty of half bin-width (= 50/2 cells). See chapter appendix for details.

measuring power-law scaling exponents in Section 5.2.2.2, and these are found to be not very sensitive to this normalisation (compare Fig. 5.7 with Fig. 5.8), with a few exceptions. The fraction, n_s, of clusters that are of size s, rather than the absolute frequency counts, N_s, is insensitive to this normalisation. From here on, we work with the frequency counts corrected for total cell number or cluster size probability distributions n_s only.

5.1.2 Video microscopy tracking data

By tracking fluorescently labelled epidermal cells computationally, we can calculate summary statistics to quantify their movement over time. For example, we can calculate their directional autocorrelation to see how quickly cells stray from their direction of movement (Fig. 5.4). We find that, after a few minutes, the directional correlation becomes very low, as if cells are choosing the angle of their next step in a position jump process from a uniform distribution of $\pm\pi/2$, decaying to $\pm 3\pi/4$ after only a few more minutes. As the frame rate of the microscopy data is three to five minutes, this is consistent with our assumption that cells are moving approximately randomly on the timescales of observation.

[3]Due to the fact the interframe interval of the video microscopy data is not consistent (due to different z-heights), different spacings for the lag had to be combined in the visualisation of velocity

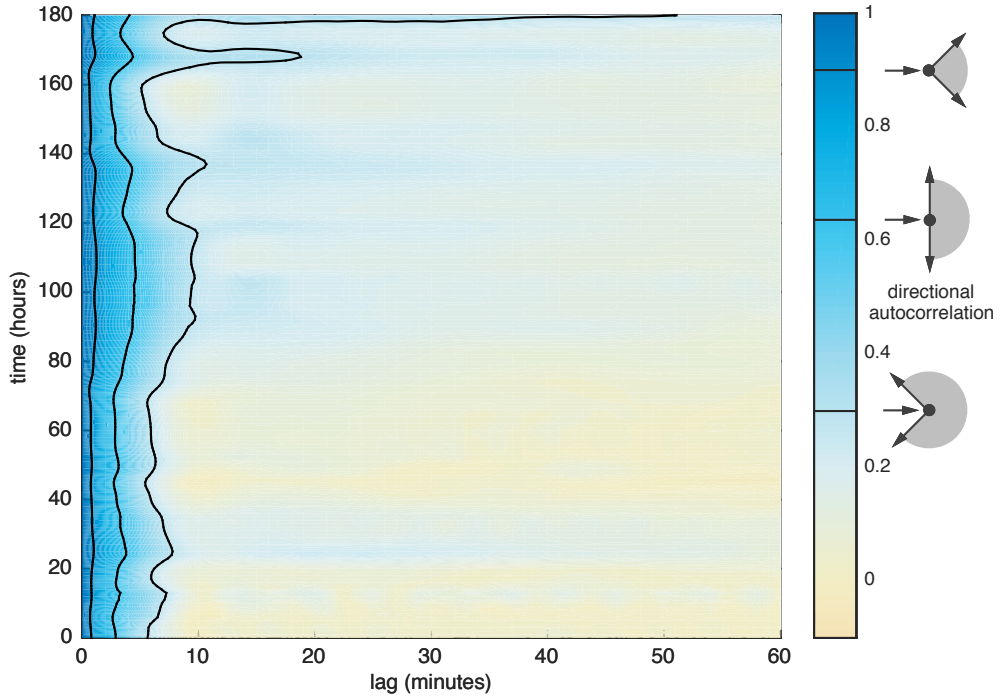

Figure 5.4: Directional autocorrelation of epidermal cells vs lag and experimental time. Tracking data from multiple microscopy videos have been binned every two hours and a smooth surface fitted[3] to the overall data. Median velocities were subtracted at each frame to correct for drift. The highlighted contours show the autocorrelation expected for position jumps with uniform random choice of angles illustrated by the schematics next to the colourbar.

One can analyse a range of other statistics of movement, and we will refer to some of these in Chapter 6. However, while we have sufficient data over the complete experimental time course to analyse temporal statistics such as directional autocorrelation, we found that the number of independently taken samples per time-point was typically insufficient for spatial statistics such as directional cell cross-correlations or radial distribution functions, that is, the number of different spatial configurations of clusters in the data is too low to be representative. Thus, we cannot currently assess to what extent cells might be locally correlated in their positions or movement directions.

Now that we have introduced the types of data with which we are working, and argued that it is suitable to assume a constant number of randomly moving particles,

autocorrelation. Treating the data as scattered (due to the inconsistent bin-sizes), a surface was fitted to the points using bicubic interpolation in MATLAB (using John D'Errico's file exchange contribution `RegularizeData3D` with smoothness parameter 10^{-4}).

let us review the theory of aggregation processes and associated scaling methods before applying this description to the data at hand.

5.2 Aggregation processes and scaling theory

In this section we take multiple, related approaches to show that the cluster-size distribution data are consistent with the hypothesis of clustering through random motion and homotypic adhesion between epidermal cells. We first review the theory of well-mixed, irreversibly aggregating particles in Section 5.2.1, and fit solutions of the Smoluchowski coagulation equations directly to the data. As this approach is feasible only for specific choices of aggregation rate functions, we more generally classify the clustering behaviour in Section 5.2.2, referring to the literature on scaling theory of aggregation processes. Continuing this thread, in Section 5.2.3 we argue that the data exhibit the well-known phenomenon of a universal distribution function. This also leads us to consider what changes in the dynamics might be occurring, which is the topic of Chapter 6.

Interested readers may find a good introduction into the kinetic theory of aggregation processes in Krapivsky *et al.* (2013).

5.2.1 Clustering of clusters

The term "clustering of clusters" (Botet and Jullien, 1984, Kolb, 1984) refers to the model process in which diffusing (or otherwise moving) particles merge into particles of larger size (and/or mass) upon contact, and these larger particles continue to move and merge upon contact with further particles. Thus it describes a substrate-free aggregation process that is appropriate for our purposes. As we will see, this class of models exhibits scale invariance, which we will be able to use to identify evidence for a change in dynamics in the data.

5.2.1.1 Smoluchowski coagulation equations

The theory of aggregating colloidal particles has a long history, dating back to Smoluchowski (1916) and his coagulation equations. In general, these describe the change in the distribution of irreversibly aggregating particles in space and time. We restrict ourselves to the well-mixed case, so that the concentration, c_s, of clusters of size s

evolves according to

$$\frac{\mathrm{d}c_s}{\mathrm{d}t} = \frac{1}{2}\sum_{i=1}^{s-1} K_{i,s-i}c_i c_{s-i} - \sum_{i=1}^{\infty} K_{s,i}c_s c_i. \tag{5.1}$$

Here, $K_{i,j}$ is the kinetic kernel (or coagulation kernel) that gives the rate at which clusters of size i and j aggregate. Since the break-up of clusters is ignored, the number of clusters of size s can only grow by a merging of clusters of size i and $s-i$, and only decrease by a merging of a cluster of size s with a cluster of any size i into a larger cluster. These cases correspond to the first and second terms on the right-hand side of (5.1), respectively. For notational convenience, we have omitted the explicit time dependence of c_s in (5.1).

Instead of concentrations, c_s, we track the fraction of clusters, n_s, that are of a certain size s (with the exception of Section 5.2.2.2). As explained in Section 5.1.1.1, this allows us to more easily ignore apparent changes in total cell number from missing single cell counts and underestimated sizes of larger clusters due to apoptosis and/or differentiation at their centres. Since we consider a closed system (with negligible cell division or death) with monodisperse initial conditions (only clusters of size one) in a constant volume, the switch from cluster concentrations to fractions is unproblematic.

5.2.1.2 Constant kernel solution

The aggregation rate kernels $K_{i,j}$ can take a variety of forms, and analytical solutions to the cluster size distribution are generally only tractable for simple forms of $K_{i,j}$, such as the simplest non-trivial case of $K_{i,j} = K$ for all i, j. This case was treated by Smoluchowski himself (Smoluchowski, 1916, 1917) and the solution for the fraction, n_s, of clusters of size s is given by

$$n_s(t) = \frac{(Kt/2)^{s-1}}{(1+Kt/2)^s}, \tag{5.2}$$

assuming monodisperse initial conditions. Here, we have given the solution for the fraction of clusters, that is, we have divided the number of clusters, $N_s(t)$, of size s by the total number of clusters, N_C, which decreases with time as $N_C(t) = N_0/[1+Kt/2]$. The above solution (5.2) can be obtained in a number of ways (Krapivsky *et al.*, 2013) (the most direct being recursively solving the equations for increasing cluster sizes and spotting the pattern) and verified by substitution.

If we want to evaluate the validity of Eq. (5.2) as a first guess against the experimental data, we need to fit, or otherwise estimate, the value of the constant K. We

want to fit this parameter for all cluster sizes simultaneously, i.e., over the surface spanned by t and s. Since we only have access to the binned size distribution data, this requires some further attention. Let us consider the cluster size distribution binned for a discrete interval of sizes $\{a, b\}$, giving the fraction of clusters, $n_{a-b}(t)$, that are between size a and b (the range denoted by the subscript), expressed as the sum

$$n_{a-b}(t) = \sum_{s=a}^{b} \frac{(Kt/2)^{s-1}}{(1+Kt/2)^s} = \frac{1}{1+Kt/2} \sum_{s=a}^{b} \left(\frac{Kt/2}{1+Kt/2} \right)^{s-1},$$

which we can simplify, by recognising the sum as a geometric series[4], to give

$$n_{a-b}(t) = \left(\frac{Kt/2}{1+Kt/2} \right)^{a-1} - \left(\frac{Kt/2}{1+Kt/2} \right)^{b}, \tag{5.3}$$

which is now in a form more amenable to fitting for a given size interval $\{a, b\}$.

Expression (5.3) was fitted against the binned cluster counts with a least-squares procedure, using the Levenberg-Marquardt algorithm and least absolute residual robustness method, as implemented in MATLAB's `fit` function. The results show decent agreement between the data and the model (root mean squared error $< 5\%$), yet some discrepancies can easily be identified by eye, such as the mismatched peaks of the second (50–99 cells) and third (100–149 cells) cluster size bins (Fig. 5.5). Since there is only a single free parameter, and we understand how varying this parameter changes the shape of the curves, we can be confident that we will not be caught in a local minimum, or at least to be very close to the global minimum. In any case, the precise value of the fitted parameter is of no particular interest, as the fitting procedure is just an automated way to match the shape of the curve to the data. As such, a match can be assessed to be sufficient by inspection. Thus, we do not consider other fitting methods.

Now that we have established the most basic form of the aggregation process as suitable to describe the data, we move to a more physically realistic form of size-dependent aggregation rates $K_{i,j}$. We could also go on to consider a time-dependent kernel $K(t)$, where the overall aggregation rate changes with time, akin to an effective temperature. However, it is unclear what functional forms of time-dependent aggregation rates are biologically plausible. An exhaustive set of tracked cluster-cluster encounters at different time-points could inform our choice of time-dependent aggregation rates, but this is a large experimental effort that is difficult to justify, so we do not consider this further. The most similar approach to this that we have come across

[4]Using the formula $\sum_{s=a}^{b} r^s = (r^a - r^{b+1})/(1-r)$ for $|r| < 1$.

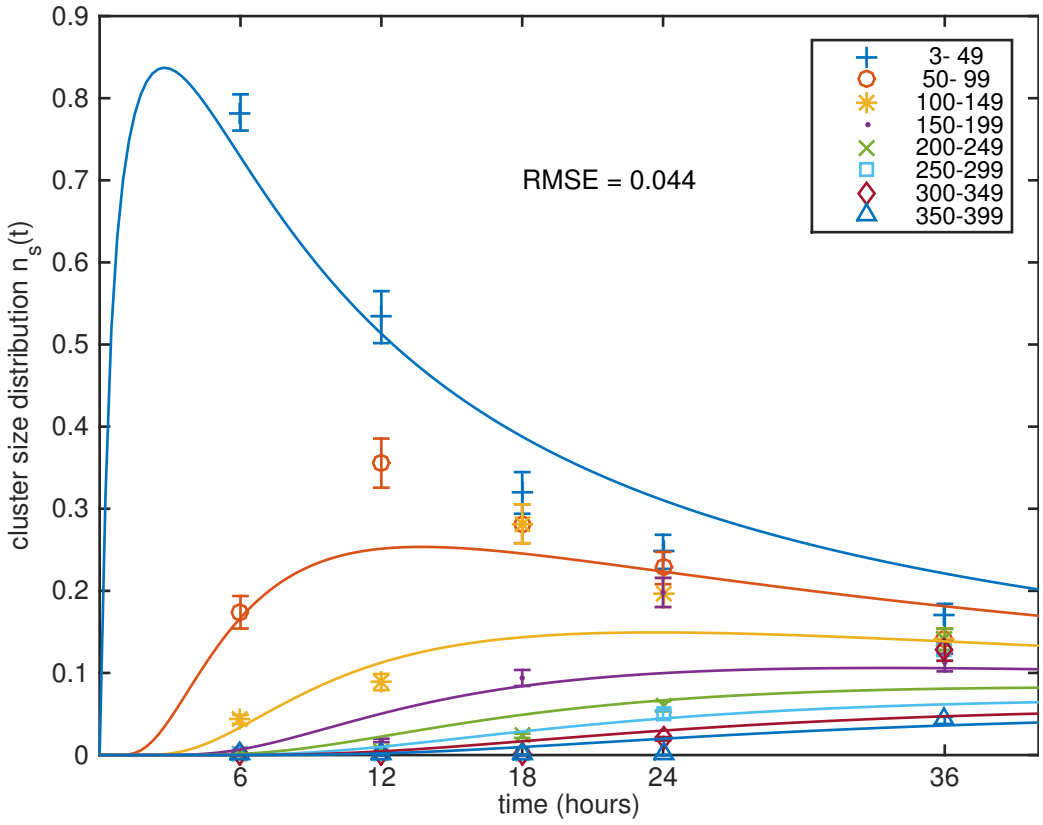

Figure 5.5: Constant kernel solution and cluster size distributions for the first 36 hours. The least-squares value for the fitted parameter is $K = 10.3\,\mathrm{h}^{-1}$ ($\pm 0.2\,\mathrm{h}^{-1}$, 95% confidence bounds). Error bars reflect estimated 10% counting accuracy.

in the literature is to consider the cross-over between different coarsening mechanisms (Leyvraz, 2003).

5.2.1.3 Brownian kernel

Previously, we have assumed a constant aggregation rate independent of the sizes of the aggregating clusters, to make the solution to the coagulation equations analytically tractable. Given a good initial fit of the constant aggregation rate model to the data (Fig. 5.5), we can now ask whether we can improve the match between theory and data with a more physically realistic aggregation rate function, for example, by including effects such as size-dependence of the motility and increased cross section of larger clusters. In systems of particles undergoing Brownian motion, the rates at which clusters encounter each other depends on their diffusivity, D, and radius, r, as these determine the flux and target surface area, respectively (Krapivsky *et al.*, 2013). These effects are taken into account when using the Brownian kernel (5.4),

which in d dimensions is given by

$$\begin{aligned} K_{i,j} &\sim (D_i + D_j)(r_i + r_j) \\ &:= K\left[2 + \left(\frac{i}{j}\right)^{\frac{1}{d}} + \left(\frac{j}{i}\right)^{\frac{1}{d}}\right], \end{aligned} \tag{5.4}$$

where the second line follows from assuming a Stokes-Einstein relation for the diffusivity, $D_i \sim i^{-1/d}$ (discussed in more detail in Section 5.2.2.1). We have ignored the numerical prefactor of 4π obtained from calculating the flux exactly, as the overall rate of aggregation, K, is difficult to estimate for the application at hand and thus has to be fitted anyway (and the constant of proportionality can be absorbed). Let us also make clear that we do not expect the cells to be undergoing true Brownian motion – their motion is assumed to be actively, and not thermally, driven. Therefore we may expect the distribution of a cluster's displacement to deviate from the Gaussian shape. However, our use of the Brownian kernel is motivated by the random direction of such displacements, and the proportionality of aggregation rates with cluster size and motility, as characterised by the measure of diffusivity. We assume this proportionality to be a reasonable consideration for cell displacements stemming from an active movement process.

We are primarily interested in the size-dependence of the aggregation rates and how this affects the evolution of the cluster size distributions. The size-scaling is investigated in more detail in Section 5.2.2. For now, let us solve the aggregation equations (5.1) with the Brownian kernel (5.4) directly and fit these to data. As the Smoluchowski coagulation equations have not been solved analytically for all but a few[5] special cases of the aggregation kernel, and in particular not for the Brownian kernel, we have to proceed numerically.

Numerical solution to aggregation equations with general kernels The Smoluchowski coagulation equations (5.1) are an infinite set of coupled non-linear differential equations. Exact numerical solution is impossible, so we have to make a cut-off for large cluster sizes. This introduces a truncation error, and mass conservation no longer holds. Methods exist to re-introduce an estimate of the truncated terms, notably one algorithm by Odriozola *et al.* (1999) that captures the effect of large clusters by utilising the known scaling behaviour, and furthermore obtains the scaled distribution function (see Section 5.2.3.1) in the process. This approach only

[5]For a review of exact solutions for sum, product and other kernels, and solutions for cross-over between different kernels, see Leyvraz (2003).

works for aggregation kernels with homogeneous scaling, which generally excludes the kernel with crowding effects that we will devise in Chapter 6. To be consistent in the accuracy of our numerical scheme, we choose a simpler method here, but one that remains applicable throughout the rest of this chapter and Chapter 6.

We check convergence of the numerical solutions for the cluster sizes of interest (the range spanned by the data), when including additional cluster sizes beyond this range. We find that the cluster size distributions change very little when including cluster sizes beyond 400 cells (Fig. 5.12, chapter appendix), despite the total number of monomers not being conserved. This is likely due to the fact that we are focussing on short timescales compared to the asymptotic behaviour, and thus the concentrations of larger clusters are low. Given the convergence of our numerical solutions, we see no need to explicitly compensate for the truncation error.

Fit to data The fit of the Brownian kernel aggregation model to the cluster size distribution data (Fig. 5.6) is slightly improved relative to the fit of the constant kernel case (Fig. 5.5, RSME 4.1% vs 4.4%), though the qualitative mismatch between the heights of the peaks remains similar.

Fitting the coagulation equations to the cluster size distribution data with the constant and Brownian kernels provides evidence for modelling the initial stages of skin cell self-organisation as an aggregation process, but with two limitations:

First, there is some mismatch in the peaks of the data and the predicted curves, despite a good overall fit. This could presumably be improved by structurally different aggregation rate functions, but without evidence or mechanistic hypotheses to guide our choice amongst the plethora of other kernels, we would be led to consider general functional forms at the cost of introducing free parameters, which might not be relatable to the data and thus make this approach prone to overfitting. Additionally, the accuracy of the manually obtained data can only be estimated, and without the full, raw data set it is difficult to assess whether a particular mismatch can be contributed to outliers or high variance at a particular time-point. So, rather than trying to find a *particular* choice from a large number of possible aggregation kernels, we can instead consider the agreement of the data with a *class* of models by analysing the scaling of certain coarse-grained features in the data with time and characteristic lengthscales of the system, i.e., the size of clusters. This is the topic of Section 5.2.2.

Secondly, a fundamental limitation of the aggregation process description is that it cannot reproduce the apparent regulation of cluster size from 48 hours onwards. In Chapter 6, we will investigate whether such size-regulation can emerge from simple

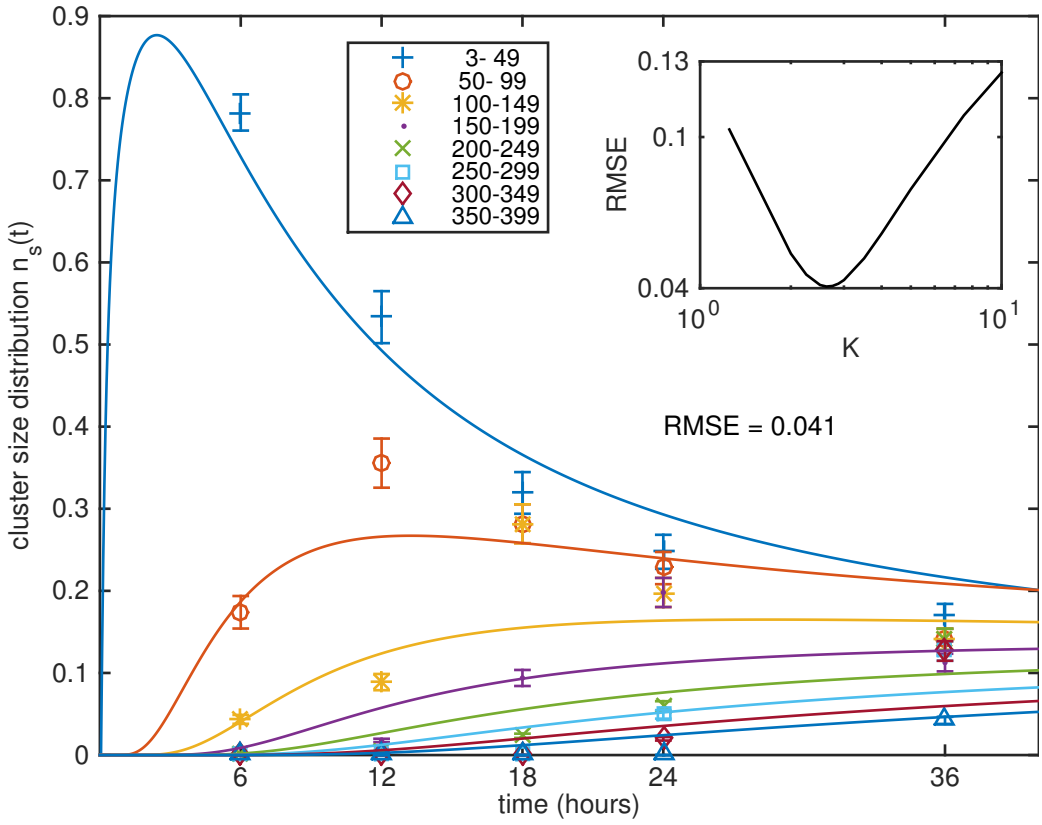

Figure 5.6: Numerical solution to the Smoluchowski equations (5.1) with a Brownian aggregation kernel (5.4) (solid lines) and cluster size distributions for the first 36 hours (see legend). The least-squares value for the fitted parameter was $K = 2.625\,\mathrm{h}^{-1}$ (inset). Error bars reflect estimated 10% counting accuracy.

size-coupling mechanisms, or whether it indeed requires, as hypothesised, a change in the dynamics through some biochemical alteration of cell properties and/or behaviour.

5.2.2 Scaling analysis

The idea behind this approach is to classify the behaviour of a system on a coarse level, irrespective of the microscopic details, by analysing how certain macroscopic descriptions of the system scale with characteristic lengthscales or time. If the scaling is the same as that observed in, or derived from, a general model, it can be said to be in the same class of model (also called "universality class"; Ódor, 2004). This is due to the fact that all processes that give rise to a particular scaling are the same in a suitably abstract sense: they underly the same symmetry constraints, dimensionality, conservation law(s) and exhibit the same collective behaviour (Ódor, 2004). For an alternative summary of the utility of the scaling approach, see Krapivsky *et al.* (2013, Chapter 5.4). Scaling theory has been successfully applied in cell biology

in recent years, for example in clonal analysis (Clayton *et al.*, 2007) and bacterial growth (Iyer-Biswas *et al.*, 2014). Here, we investigate whether clustering epidermal cells have the same scaling behaviour as the diffusing, irreversibly sticky colloidal particles of the hypothesised aggregation process, and thus whether they belong to the same universality class. We show that this is the case, and that therefore we can conclude that the data are consistent with the aggregation hypothesis, regardless of our uncertainty about the exact nature of the cells' motility and adhesive properties.

5.2.2.1 Scaling ansatz

As we saw, the expression for the kinetic kernels, $K_{i,j}$, is often too complicated to allow analytical solutions to the Smoluchowski equations (5.1). In scaling analysis, one classifies solutions "in terms of generic features of the reaction kernel" (Krapivsky *et al.*, 2013), such as its homogeneous scaling, given by

$$K_{ai,aj} = a^{2\omega} K_{i,j}. \tag{5.5}$$

A more general[6] scaling is considered by the secondary ansatz, $K_{i,j} \sim i^{\mu} j^{\nu}; i \ll j$, with $2\omega = \mu + \nu$ (Odriozola *et al.*, 1999).

The above ansatzes make an assumption about how the kinetic coefficients scale when the cluster size is scaled by a factor a (or a and b for independent scaling of the two cluster sizes i and j). For example, if two clusters aggregate at a certain rate, how does this rate change if the clusters are twice as big, or half the size? The answer is characterised by the scaling exponent(s), ω (or μ and ν), with which one can classify the asymptotic solutions to the coagulation equations (5.1). For example, cluster size distributions at long times have peaks for $\mu < 0$, whereas for $\mu > 0$ they are monotonically decreasing (Odriozola *et al.*, 1999). As another example, there is a critical value, ω_c, at which gelation occurs and above which cluster size becomes infinite in a finite time (Meakin (1990): "the average mass can diverge in a finite time"), given by $\omega_c = 1/2$ (Botet and Jullien, 1984). The cases of $\omega > 1$ or $\nu > 1$ are considered unphysical, as the rate of cluster aggregation rises faster than their mass (Odriozola *et al.*, 1999). Thus, the behaviour of a system depends strongly on the numerical values of the scaling exponents, and these have to be determined to classify the model. They can be derived for simple models, such as aggregation under ballistic

[6]Sometimes the secondary ansatz is written as $K_{ai,bj} = a^{\mu} b^{\nu} K_{i,j}$ (Goodisman and Chaiken, 2006). This is more general, but less useful for considering the classification of asymptotic solutions. In more complicated forms of the Smoluchowski equations (5.1), the kinetic kernels could also scale with particle velocity v, as well as size s, i.e., $K_{as_i,as_j;bv_i,bv_j} \sim a^{\omega_s} b^{\omega_v} K_{s_i,s_j;v_i,v_j}$ (Jiang and Leyvraz, 1994).

or diffusive motion, and we make use of this in Section 5.2.2.3, when comparing such derived scaling exponents to empirically observed power-law exponents of the data.

Scaling of constant and Brownian kernels The homogeneous scaling of the constant kernel trivially satisfies $\omega = 0$. For the Brownian kernel, we need to consider the scaling of both the diffusivity, D, and the particle radius, r, with the number of cells in a cluster. From a simple argument using the Stokes-Einstein relation (or Stokes-Einstein-Sutherland relation; Sutherland, 1905, Einstein, 1905) for a spherical particle at low Reynolds number, one would expect $D \sim 1/r \sim s^{-1/d}$ (where d is the dimensionality), and for tightly packed, approximately spherical clusters, $r \sim s^{1/d}$. The homogeneous scaling of the Brownian kernel is then the same as that of the constant kernel ($\omega = 0$), which is part of the justification for studying the tractable constant kernel despite the implausible assumption of size-independent aggregation rates (Krapivsky *et al.*, 2013). The secondary scaling of the Brownian kernel in d dimensions is $K_{ij} \sim i^{-\frac{1}{d}} j^{\frac{1}{d}}$ for $i \ll j$, i.e., it has the scaling exponents $\mu = -1/d$ and $\nu = 1/d$.

5.2.2.2 Empirical power-law scaling of size distributions

Several studies have observed power-law scaling behaviour in the size distributions undergoing a Smoluchowski coagulation process, both empirically in numerical simulations (Vicsek and Family, 1984, Kolb, 1984, Meakin *et al.*, 1985, Sholl and Skodje, 1995, Mattsson *et al.*, 1999) and through predictions from analytical approximations to solutions of the aggregation equations (Botet and Jullien, 1984, Jiang and Leyvraz, 1994, Leyvraz, 2003). To pick one relevant example, Vicsek and Family (1984) and Meakin *et al.* (1985) undertook numerical simulations of clustering particles and observed certain scalings of the cluster size distributions with size and time in the form of power law asymptotes, as well as simple, algebraic expressions that relate the different power-law exponents. Applied to the data from epidermal cell clusters, the results are strikingly similar, hence we closely follow their approach in this section.

For consistency with Vicsek and Family (1984) and Meakin *et al.* (1985) and to aid the comparison[7], we consider the number of clusters, $N_s(t)$, (rather than the fraction $n_s(t)$) and investigate the scaling behaviour with both s and t on a logarithmic scale. This can be described by asymptotes and tangents to the size distributions, with scaling exponents to be measured by fitting a power-law for the appropriate time or

[7]In the notation by Vicsek and Family (1984) and Meakin *et al.* (1985) the exponents α and β are called w and z, respectively.

lengthscales. In agreement with previous studies (Vicsek and Family, 1984, Meakin *et al.*, 1985, Krapivsky *et al.*, 2013), we see a scaling of the mean cluster size, $\bar{s}(t)$, with time (Fig. 5.7(A)) of the form

$$\langle s(t) \rangle \sim t^{\beta}. \tag{5.6}$$

A corresponding scaling occurs for the total number of clusters, $N_C(t) = \sum_s N_s(t)$ (Fig. 5.7(B)), which is just proportional to the inverse of the mean cluster size. This power law can be verified by inspection for the constant kernel solution (5.2), and it can also be derived under the scaling ansatz (Krapivsky *et al.*, 2013).

At large times, t, cluster frequency counts show a common slope for small cluster sizes (Fig. 5.7(C)) with polydispersity[8] exponent τ (Leyvraz, 2003). We can also observe an asymptote for large times with exponent α in the scaling with time (Fig. 5.7(D)). Taken together, these suggest the scaling

$$N_s(t) \sim s^{-\tau} t^{-\alpha}, \tag{5.7}$$

which is what one may expect if the solutions to the Smoluchowski equations are separable into size- and time-dependent parts (Krapivsky *et al.*, 2013). Note that we omit the first time-point when fitting to determine the scaling exponents, as the results from the relevant scaling theory hold at large times only (Vicsek and Family, 1984, Meakin *et al.*, 1985). Cluster size distributions from different time-points are further enveloped by a common tangent that touches the "knee" of each curve as it bends downwards (Fig. 5.7(C)).

We now have to check whether our correction for non-constant total cell numbers (Section 5.1.1.1) affects the scaling in the data. Repeating our analysis on the original (uncorrected) data set, we find that the power-law exponents, β, τ and α are unaffected by the normalisation procedure, whereas ν and the slope of the common tangent change (Fig. 5.8). Nevertheless, the qualitative similarities to the scaling observed in simulations of clustering particles (Vicsek and Family, 1984, Meakin *et al.*, 1985) remains.

5.2.2.3 Scaling of the diffusion coefficient with cluster size

Another important scaling effect to consider is that of the size dependence of the cluster diffusion coefficient. This cannot be observed directly from the cluster size

[8]Polydisperse meaning of a range shapes or sizes, as opposed to monodisperse, where all particles are of the same shape or size.

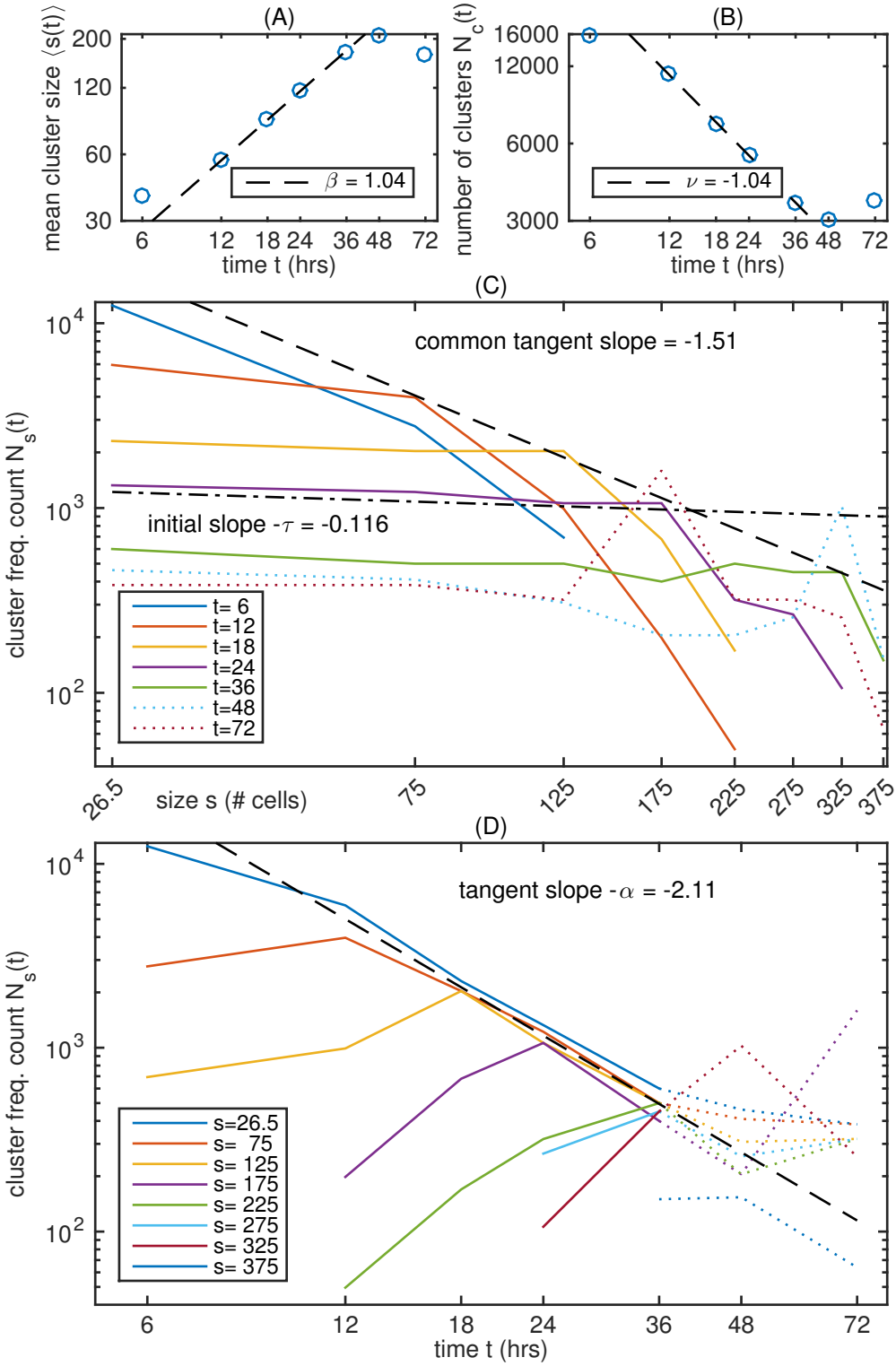

Figure 5.7: Power-law scaling with time in the mean cluster size (A), the number of clusters (B), and with both cluster size (C) and time (D) in the cluster frequency counts. Cluster sizes in (C) are histogram bin centres as provided in the data. Slopes of dashed and dash-dotted lines were obtained from least-squares solutions of power laws (5.6) and (5.7) to relevant data. Dotted lines show time-points not considered.

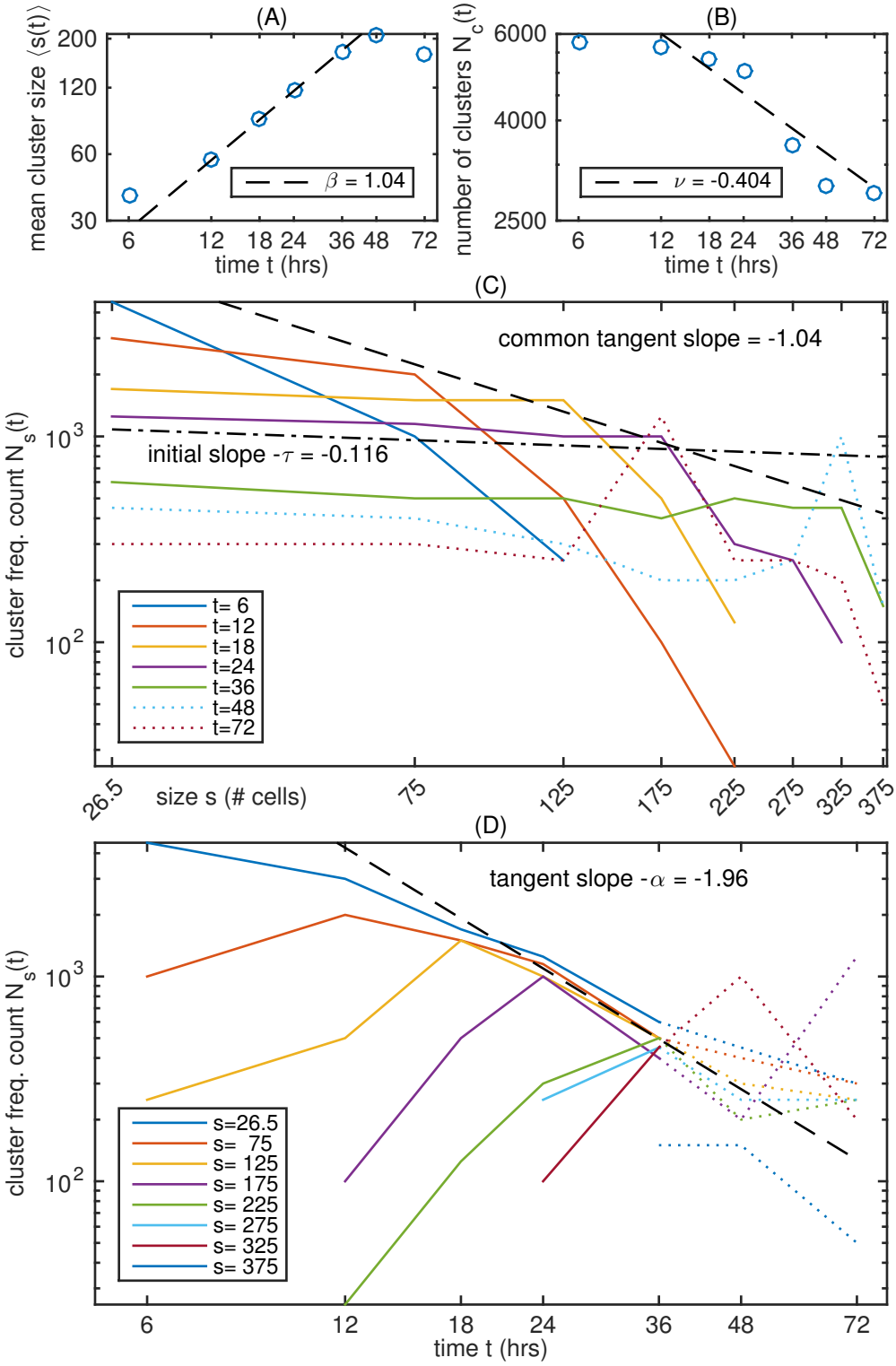

Figure 5.8: Power-law scaling in the size-distribution data. The data shown are the same as in Fig. 5.7, but without correcting for non-constant total cell numbers.

distributions, but critically determines their scaling behaviour (Meakin *et al.*, 1985), as we outline in this section. Assuming that the diffusion coefficient of a cluster scales inversely with its size with an exponent γ, i.e., $D \sim s^{-\gamma}$, an algebraic relationship between γ and β can be derived in a number of ways (Botet and Jullien, 1984, Meakin, 1990, Jiang and Leyvraz, 1994, Sholl and Skodje, 1995, Kandel, 1997). Here, we follow the less formal argument of Sholl and Skodje (1995) for its simplicity, but generalise it to any number of dimensions, which yields the same result as in the other derivations found in the literature.

We start from a scaling of the average cluster spatial scale, $\langle r \rangle$, with time, t, as $\langle r \rangle \sim t^{\beta/d}$, where β is the scaling exponent and d is the dimensionality of space. This is consistent with the observed scaling of average cluster size (Fig. 5.7). Consider now t_1 to be the time for the system to grow from scale $\langle r \rangle = r_0$ to kr_0, and t_2 the time to grow further to $k^2 r_0$. From the scaling relation it follows that $t_2 = k^{d/\beta} t_1$. Requiring self-similarity, the spatial structure of the system at times t_1 and t_2 should be identical if rescaled by a factor of k (Sholl and Skodje, 1995). The mean-square displacement of a cluster of scale r_0 at time t_1, is, according to the size-dependence of the diffusivity, given by $\langle \delta r^2(t_1) \rangle \sim (r_0^d)^{-\gamma} t_1$, where γ describes the scaling of diffusivity with size through $D \sim s^{-\gamma}$ (as above). Informally, we may generalise to a trajectory of fractal dimension d_w (e.g. $d_w = 2$ for diffusion, $d_w = 1$ for ballistic motion) in a space of dimension d to obtain $\langle \delta r^{d_w}(t_1) \rangle \sim (r_0^d)^{-\gamma} t_1$. Similarly, for a cluster of size kr_0 at time t_2, the displacement is given by $\langle \delta (kr)^{d_w}(t_2) \rangle \sim (k^d r_0^d)^{-\gamma} t_2$. Using the self-similarity argument, we can demand $\langle \delta (kr)^{d_w}(t_2) \rangle = k^{d_w} \langle \delta r^{d_w}(t_1) \rangle$. Substituting the expression for the displacements and the relationship between t_1 and t_2, by matching exponents for k we arrive at:

$$\beta = \frac{1}{\frac{d_w}{d} + \gamma}. \tag{5.8}$$

Here we have assumed that the (fractal) dimensionality of the space, or substrate, and that of the cluster[9] are the same, i.e., that clusters are compact. For three-dimensional clusters undergoing a random walk ($d_w = 2$) in a three-dimensional space ($d = 3$), we have

$$\beta = \frac{1}{2/3 + \gamma}. \tag{5.9}$$

From the earlier Stokes-Einstein argument, $D \sim 1/r \sim s^{-1/d}$, and thus $\gamma = 1/3$ for three-dimensional clusters. We found $\beta \approx 1$ from the data (Fig. 5.7), so the relation holds, demonstrating consistency between the model considered, the scaling ansatz

[9]For the case of clusters with fractal dimension d_c, the relations (5.8) and (5.10) generalise to $\beta = 1/(1 - 2\omega)$ and $2\omega = (d - d_w)/d_c - \gamma < 1$, respectively (Botet and Jullien, 1984).

and the observed scaling. Additional independent verification could be obtained by investigating whether the diffusion of clusters does indeed scale in this way experimentally, e.g., by tracking clusters (rather than cells). This goes beyond the data at hand and is thus outside the scope of this thesis.

Relation (5.8) has also been linked (Botet and Jullien, 1984) with the scaling exponents of the kinetic coefficients (5.5) in the Smoluchowski equations (5.1), via

$$2\omega = 1 - \beta^{-1} = 1 - \frac{d_w}{d} - \gamma. \tag{5.10}$$

With $d_w = 2$ and $d = 3$ as before, and $\gamma = 1/3$ (or $\beta \approx 1$, as measured in Fig. 5.7), this would suggest that $\omega = 0$, and thus that the kinetic kernels $K_{i,j}$ are invariant under homogeneous scaling (5.5) with particle size i and j. This is consistent with the constant and Brownian kernels used earlier in Section 5.2.2.1 and for related aggregation processes in the literature (Meakin, 1990, Goodisman and Chaiken, 2006, Krapivsky *et al.*, 2013). Size-invariance of aggregation rates is trivially true for the constant kernel, whereas for the Brownian kernel, the scaling of the diffusion constant, D, with cluster size, i, $D_i \sim i^{-1/d}$, and that of the particle radius, $r_i \sim i^{1/d}$, cancel out when homogeneously scaling i and j by the same constant.

Having compared the scaling in the size-distribution data with numerical studies of similar aggregation processes, we now consider a related phenomenon that clearly visualises the self-similarity and scale invariance, namely the observation of a common distribution in the rescaled data at different time-points.

5.2.3 Universal distribution function

An important consequence of scaling is that certain descriptions of the system become scale-invariant once we rescale relative to the characteristic length- and timescales. Since the scaling ansatz implies that aggregation between small clusters and aggregation between large clusters are statistically similar, the distribution of clusters relative to some characteristic system scale should be invariant in the rescaled system. In other words, we should be able to describe the dynamics fully (at a coarse level) by the change in the characteristic cluster size over time. As a characteristic lengthscale, we may choose the mean cluster size at a given time, $\langle s \rangle = \sum_s s n_s / \sum_s n_s$ (though ratios of other moments M_{n+1}/M_n also work, where $M_n = \sum_s s^n c_s$ is the nth moment of the cluster size distribution; Krapivsky *et al.*, 2013). To rescale the data, we then simply divide the cluster size by the mean cluster size at a given time and plot the resulting distribution. When rescaling the argument of the distribution function in

this way, we need to multiply by the characteristic size to conserve overall probability normalisation[10], i.e.,

$$f_\omega\left(\frac{s}{\langle s\rangle}\right) \sim \langle s\rangle n_s = \frac{N}{N_C^2} N_s. \tag{5.11}$$

Here, $\langle\rangle$ denotes the population average, the subscript on the scaling function f_ω denotes its dependence on the homogeneity exponent and we have additionally stated the rescaling in terms of the raw cluster counts (Section 5.1.1), using the number of clusters, $N_C = \sum_s N_s$, and the number of cells, $N = \sum_s sN_s$. Importantly, f_ω is independent of time. Thus the size distributions at different times should all[11] collapse onto a single curve if rescaled according to equation (5.11). The form of this curve depends on the kinetic kernels, and an exact solution may be intractable, though asymptotic solutions have been derived[12]. Various approximations exist in the literature, but rather than comparing the details of different approximations with explicit functional forms, we instead look for evidence of an underlying distribution function of general form (5.11) in the scaled data as a signature of the aggregation dynamics.

5.2.3.1 Collapsing size distributions

By rescaling the cluster size relative to the average at each time-point, and rescaling the cluster size distributions accordingly to preserve particle number, we test whether the shape of the distribution function is changing over time, or whether it is only scaled by increasing average cluster size and decreasing number of clusters. Applying the scaling as in (5.11) to the data in Fig. 5.2, the data from different time-points collapse onto a common curve. The collapse is less pronounced for 36 hours than for the earlier time-points (Fig. 5.9, 5.10). This might indicate the formation of a peak in the size distribution, which is a qualitative shape change of the distribution function. Indeed, we see peaks in the unscaled distribution at 48 and 72 hours (Fig. 5.2), and

[10] When the distribution function is given in terms of concentrations, we have to multiply by the square size to conserve mass when rescaling.

[11] One might expect that this may depend on the initial distribution of cluster sizes, but here we are only interested in the initial condition where all particles are monomers. In addition, Kandel (1997) has shown that regardless of initial cluster size distributions, a particular scaling function is selected dynamically out of a family of solutions.

[12] Botet and Jullien (1984), for example, derive an approximate solution for large s, given by

$$f_\omega(x) \approx \frac{(1-2\omega)^{(1-2\omega)}}{\Gamma(1-2\omega)} x^{-2\omega} e^{-(1-2\omega)x},$$

where Γ is the gamma function.

at these time-points there is no collapse of the rescaled distribution function (shown only for 48 hours, Fig. 5.9), as can also be seen from the power-law scalings (Fig. 5.7). This indicates a change in the aggregation dynamics, and we comment on possible causes in Section 5.3.

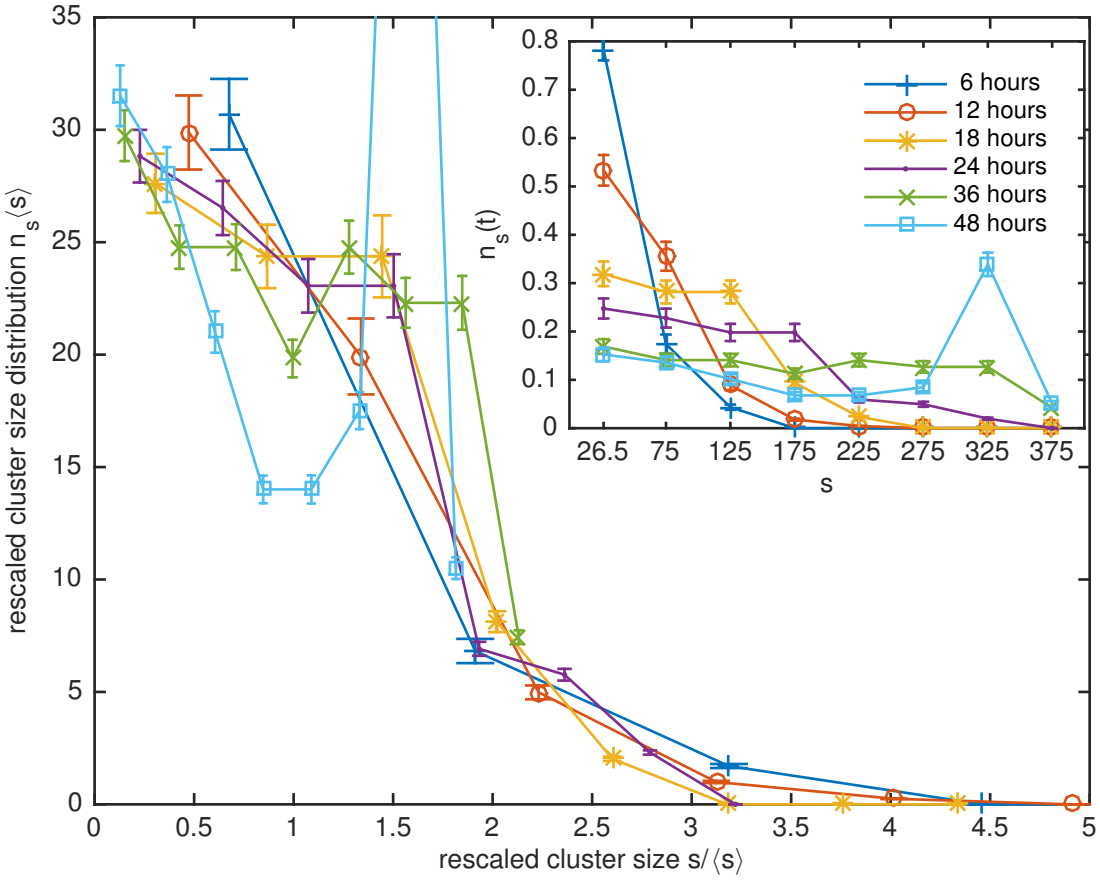

Figure 5.9: Collapsing cluster size distributions according to (5.11). Lack of collapse for the 48 hour curve indicates a change in the cluster growth dynamics. The raw data (without rescaling) show no collapse (inset). Unscaled cluster sizes (inset abscissae) were taken from bin centres.

While collapse of the rescaled cluster size distributions compared to that of the unscaled distributions is evident by visual inspection, it is difficult to quantify without knowing the explicit form of the scaled distribution function, f_ω (5.11). This is intractable for most forms of the kinetic kernels (5.5). Instead, we again take an approach that is free of approximations with explicit functional forms and we simply assess the degree of collapse of the scaled data onto itself. Thus, we can determine to what extent, for a given rescaling, the data lie on a single curve without being constrained by the intricacies of fitting asymptotic approximations. Alternatively,

we could resort to asymptotic solutions of the scaled distribution function from the literature, or solve for an approximate distribution function numerically (Kandel, 1997). For the analytic approximation, we expect from the scaling exponents for the Brownian kernel, $\mu = -1/d$, a distribution function of $\Phi(x \ll 1) \sim \exp(-x^{-\frac{1}{d}+\cdots})$ and $\Phi(x \gg 1) \sim x^{-2\omega}\exp(-cx)$ (where c is a constant, and x any argument, such as the rescaled size variable) (Odriozola *et al.*, 1999, Goodisman and Chaiken, 2006). This could be compared to the rescaled size-distributions (Fig. 5.9), requiring fitting of the cut-offs where $x = s/\langle s\rangle \ll 1$ and $x \gg 1$ cease to be good approximations. As an example, one could fit a distribution $\Phi(x) \sim \exp(-x^{-\frac{1}{d}} - cx)$, for some constant c. Alternatively, one could replace a stretch from, for example, $x = 1/2$ to $x = 2$ with a constant and use $\Phi(x \ll 1)$ and $\Phi(x \gg 1)$ either side, but this is difficult to motivate on theoretical grounds.

5.2.3.2 Quantifying collapse

To quantify the degree to which the rescaled data collapse onto a common curve, we follow an approach similar to that of Bhattacharjee and Seno (2001), with minor modifications. First, we interpolate a set of points (e.g., the scaled size distribution at a particular time) by some function (e.g., piecewise linear), and then calculate the residuals of all sets of points (e.g., the scaled distribution values at all times) to this interpolation. By repeating this for every set of points (e.g., creating an interpolated distribution function at each time-point), we can quantify the collapse of a set of curves through an average of these residuals. Denoting the interpolated values of a set of points p by $\tilde{y}_p$, the residual of collapse is defined by

$$R_c = \langle\langle |y_i - \tilde{y}_p(x_i)|^q\rangle_i\rangle_p^{1/q}, \tag{5.12}$$

where the (x_i, y_i) are all rescaled abscissa-ordinate pairs, q can be any integer (here $q = 1$), and $\langle\ldots\rangle_i$ denotes the average over index i. No extrapolations are made, i.e., abscissae that do not lie in the overlap of the range of two sets are not included in the averages. The choice of interpolating function has to be informed by assumptions about the smoothness or appropriate functional form of the scaling function, and care has to be taken if there are any singularities in the range of interest (Bhattacharjee and Seno, 2001). We have used linear interpolation, but results were similar using shape-preserving piecewise cubic interpolation or cubic splines (as implemented in MATLAB). This residual of collapse, R_c, is sensitive to the overall scale of the ordinates, as it is an average over residuals, which are absolute, rather than relative,

differences. Therefore the residual of collapse can only be used as a measure to compare or optimise different scalings within the same data set (or between data sets of similar range). As can be seen from Fig. 5.10, the collapse of the size distribution data becomes less pronounced the more time-points we include, with a sharp increase in R_c beyond 36 hours.

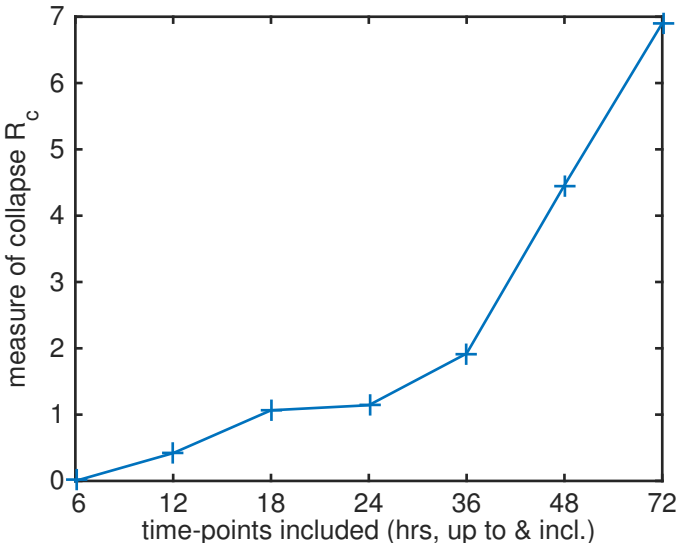

Figure 5.10: Residual of collapse (5.12) sharply increases when including 48 and 72 hour data sets.

We can attempt to further visualise the degree of collapse using a similar idea of interpolating each rescaled distribution and averaging the resulting curves over all data sets (time-points). The results can be seen in Fig. 5.11. While there is a clear improvement in smoothness over the overall interpolation of all data, this approach is potentially lacking as a method of describing the underlying scaling function, especially in regions of steep changes in the re-scaled distribution functions (cf. Fig. 5.11, $s/\langle s\rangle \approx 1.8$). As the spacing between abscissae varies between data sets due to the scaling, steep changes are flattened by the interpolation. Here, knowledge of the scaling function through a numerical solution or an appropriate analytical approximation is more useful to resolve such features.

5.3 Discussion

We have analysed skin cell-cluster size and frequency measurements and compared these data with the aggregation process models of clustering clusters. Our three-pronged approach has shown agreement of the data with a mean-field model (which

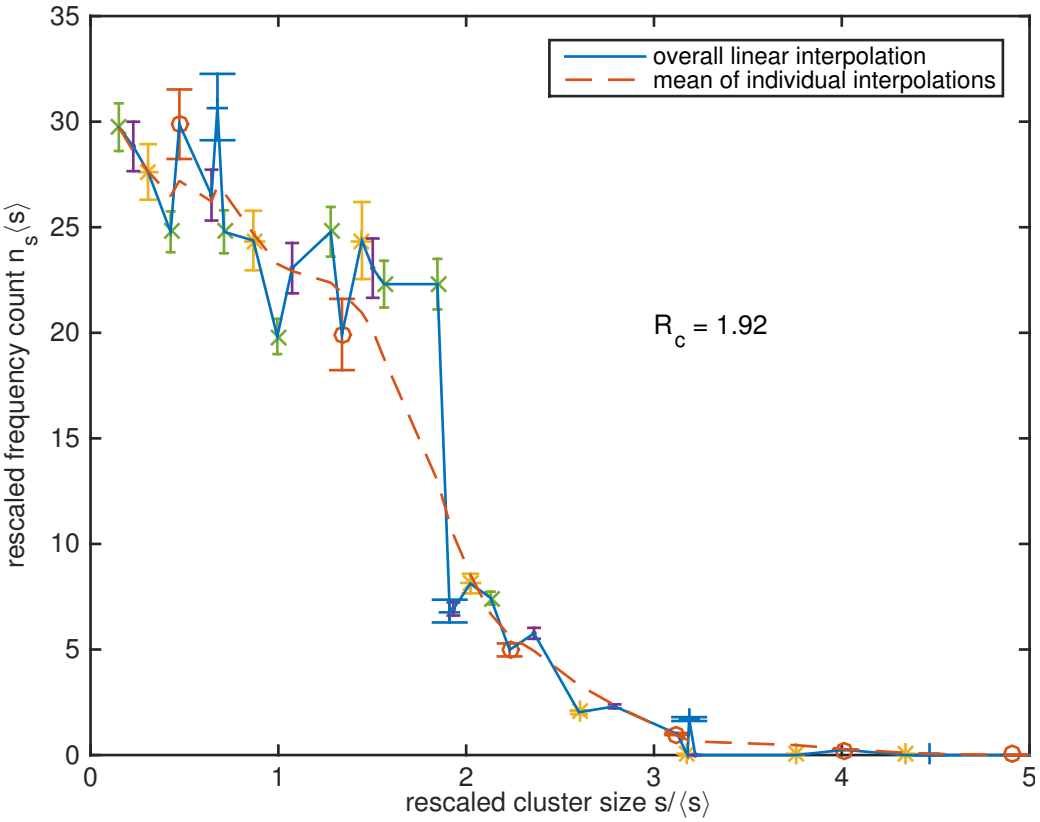

Figure 5.11: Interpolations of collapsed size distributions.

we fitted directly), expected power-law scalings (that are found in spatial simulations of clustering clusters in the literature), and a model-agnostic dynamic scaling hypothesis. First, we directly fitted analytical and numerical solutions to Smoluchowski coagulation equations in the case of constant and Brownian aggregation kernels. We achieved good agreement of the mean-field description with the data, though there may be other aggregation rate functions one could consider that may give similar results. To emphasise the commonality with physical aggregation models further, we have measured the power-law scaling of mean cluster size, number of clusters and cluster frequency counts with cluster size and time, similar to studies by Vicsek and Family (1984), Meakin *et al.* (1985), Jiang and Leyvraz (1994) and Meakin (1990) that simulated aggregation of particles and fluid droplets. Finally, we investigated whether the cluster size distributions would collapse if rescaled by (5.11), as one would expect from the class of models of "clustering clusters", which includes the type of Smoluchowski coagulation taken in the initial approach. This firmly classifies the observations as consistent with the hypothesis of randomly moving epidermal cells that aggregate upon contact.

In this section, we further verify theoretical predictions related to the scaling we observed, discuss the limitations of our approach and point out alternatives and suggest future work.

5.3.1 Scaling relations

The power-law exponents we measured satisfy a scaling relation predicted[13] from the scaling ansatz and number conservation, $\alpha = (2-\tau)\beta$, with $\alpha = 2.11$ (Fig. 5.7; or $\alpha = 1.96$ when not correcting for non-constant cell numbers, Fig. 5.8) and $(2-\tau)\beta = 1.96$. In simulations of clustering clusters, the curves of cluster frequency counts vs cluster size are found to be enveloped by a common tangent of gradient -2 (Meakin *et al.*, 1985). For the skin cell data, we find this gradient to be closer to $-3/2$ (Fig. 5.7; or -1 when not correcting for non-constant cell numbers, Fig. 5.8). The meaning of this discrepancy is unclear. Meakin *et al.* (1985) obtain the slope of the common tangent from the exponent of θ in their scaled distribution function, $N_s(t) \sim s^{-\theta} g(s/t^{\beta})$. In an earlier paper, Vicsek and Family (1984) state that $\theta = 2$ and report this to be independent of spatial dimension. If this is indeed the case, then the discrepancy may be due to the available data spanning insufficiently many orders of magnitude to reliably estimate scaling exponents (Clauset *et al.*, 2009, Stumpf and Porter, 2012). Alternatively, the discrepancy could result from finite concentration effects, as one would only expect the simple scaling to hold in the limit of zero concentration (Meakin *et al.*, 1985). In our review of the literature, we could not find an explanation of the source of the common tangent exponent from theoretical considerations (rather than empirical observations), and this may be an open problem in the understanding of aggregation processes. We do not pursue the discrepancy of the common tangent further. Our main objective was to establish whether the initial stages of skin cell self-organisation could be described by the process of cluster-clustering, which they can. This provides us with a mechanistic understanding of the first part of the skin self-organisation process, as well as clear evidence that the system transitions to different dynamics after two days.

[13] For a scaling of the distribution function of the form $N_s(t) \sim t^{-\alpha} s^{-\tau} f(s/t^{\beta})$ (Vicsek and Family, 1984), where $f(x) \approx 1$ for $x \ll 1$, the number of particles integrates to $N \sim t^{-\alpha+(2-\tau)\beta}$, from which the scaling relation follows by requiring constant particle number. Alternatively, for a scaling of the distribution function of the form $N_s \sim s^{-2} g(s/t^{\beta})$ (Meakin *et al.*, 1985), with $g(x) \sim x^{\delta}$ for $x \ll 1$, and an observed scaling of $N_s \sim t^{-\alpha} s^{-\tau}$, one arrives at the scaling relation by equating exponents for s and t separately, eliminating δ.

5.3.2 Complementary and alternative mechanisms

Observations of cell sorting have often been explained on the basis of differential adhesion (Steinberg, 1962, 2007), or more generally, differential interfacial tension (Brodland, 2002). Under such a framework, one would predict the observed cell separation to result from a model with strong (adhesive) homotypic interactions between epidermal cells, intermediate strength heterotypic interactions between epidermal and dermal cells, and weak homotypic interaction among dermal cells. Here, we have instead opted for a description in the language of kinetic theory. This allowed us to explicitly check predictions about the evolution of the cluster size distribution. Our approach can be seen as the binary limit of taking the epidermal-dermal and homotypic dermal interactions to zero, while making the homotypic epidermal interactions fully and irreversibly adhesive upon contact. Thus, our description represents a simplified case that can be built upon by considering interactions with, and among, the dermal cells.

Alternatively, it is conceivable that segregation of dermal and epidermal cells could happen in the other extremes, where there is no adhesion even between epidermal cells. Weber *et al.* (2015) have observed in numerical simulations that binary mixtures of active particles can de-mix based on the difference in their diffusivities alone. However, this only works for large differences in diffusion constants, which is not supported by the data at hand.

5.3.3 Aggregation processes of active particles

It is not *a priori* evident that the kinetic descriptions of aggregation, which were developed for passive physical systems, are applicable to systems of actively moving particles. While we are not claiming that epidermal cells are diffusing in the thermal sense, we have shown that their persistence is very low (Fig. 5.4). Still, one may object that the resulting scaling exponents need not be the same, and that the observed agreement may be accidental. While an anomalous scaling of aggregation in systems of active Brownian particles has been reported, this was not observed, crucially, in three dimensions (Stenhammar *et al.*, 2014). Thus, we may be in a regime where the active nature of the cell's motility makes no qualitative difference to the coarse-grained, global behaviour.

In recent work, Cremer and Löwen (2014) have studied the scaling of cluster growth for active particles for different cluster movement models. For the case that only particles on the surface of an aggregate (in three dimensions) contribute to

the cluster's movement, and the movement of the individual particles in a cluster is uncorrelated, they found a scaling of

$$s(t) \sim t^{\frac{1}{\frac{2}{3}+2\tilde{\gamma}}},$$

in the diffuse regime, where $\tilde{\gamma}$ determines the reduction of an individual particle's motile force with cluster size through $\mathbf{F}_i \sim s^{-\tilde{\gamma}}$. Our observed linear scaling of cluster size with time ($\beta = 1$, Fig. 5.7) then implies $\tilde{\gamma} = 1/6$. We can identify the scaling of the force with that of the cluster velocity (where, in $d = 3$, Cremer and Löwen (2014) find $v \sim s^{-\tilde{\gamma}}$) through $D \sim \langle v^2 \rangle$ (Green-Kubo relation; Einstein, 1905, Visscher, 1973), and thus $\tilde{\gamma} = \gamma/2$, reconciling the value for $\tilde{\gamma}$ our earlier result on passively diffusing particles, for which $D \sim s^{-\gamma}$ with $\gamma = 1/3$ (Section 5.2.2.3). This gives additional support that in three dimensions, for random walkers, we do not need to worry about the fact that movement is active.

5.3.4 Conclusions

The agreement between the size distributions of epidermal cell aggregates and the solutions to the aggregation equations (with only one free parameter fitted), the scaling of the average cluster size, number of clusters and the power-law dependence of cluster size distributions, as well as the collapse of the rescaled distributions onto a common distribution function, is such that we conclude that epidermal cells in this experimental assay cluster through undirected motion and coagulation for the first 36 hours of the skin reconstitution experiment. Importantly, the scaling observed in the size distribution data independently justifies our use of the Smoluchowski coagulation equations, and excludes other mechanisms of coarsening, such as spinodal decomposition, where the characteristic length scales linearly with time (Jury *et al.*, 1999), or Ostwald ripening, which has a differently shaped distribution function (Yao *et al.*, 1992, Lo and Skodje, 2000).

With an abstract description of cell self-organisation, such as the one we have chosen, one has to critically assess to what degree this simplification is accurate in light of the noisiness commonly associated with biological data. This is of particular concern for the power-law scaling observed in the size distributions. On the one hand, agreement of the data with the scaling theory from the literature is remarkable, considering the approximate nature of the cell count data, apparently violated assumption about constant cell numbers and active movement of epidermal cells in a crowded environment. On the other hand, power laws are known to be suspiciously

easy to find, and their over-interpretation has been prominently criticised (Stumpf and Porter, 2012). However, we have a mechanistic underlying hypothesis with vast theoretical backing in the literature (see references throughout this chapter), which we believe makes our approach viable.

Future work could invest its efforts into a more thorough "principled statistical framework" (Clauset *et al.*, 2009) for estimating power-law behaviours, as data over more orders of magnitude are not available (due to the timescale of the biological process) to lend the scaling measurements more statistical rigour. Such an extension of this work would also benefit from obtaining cluster counts from reliable tracking data in an automated way, and measuring the size-dependence of the cluster velocities or diffusion coefficients.

Additional theoretical investigations could derive appropriate forms of the aggregation kernels for actively moving, soft particles. For the biological application discussed here, though, the additional explanatory power of more realistic aggregation rates is low, given the good agreement we saw with the simpler functional forms we used. However, it may serve as an inspiration for other applications in cellular self-organisation and the theory of aggregation processes.

Our aim was to classify the mechanism of aggregation in the early stages of skin cell self-organisation in the experimental assay described, which we have achieved by suitably coarse-grained data analysis and comparison with a kinetic theory of aggregation. The analysis has provided us with a basic mechanistic understanding of how epidermal cells self-organise through clustering in the process of *in vitro* skin reconstitution. This understanding can now be further tested and refined microscopically, e.g., by perturbing cell motility or adhesion molecules. Experimental efforts will thus most likely lead the way to identify the molecular players involved.

From an overarching theoretical perspective, a next fruitful step may be to consider the remaining stages of the skin reconstitution process, as we have only considered part of the tissue formation process and only one of two cell types. In this chapter, we presented evidence that the dynamics are changing as the size of cell aggregates seems to stabilise. In Chapter 6, we consider crowding by dermal cells as one possible mechanisms for arresting aggregation and regulating the size of epidermal cell clusters.

Chapter appendix

Combination of errors and uncertainty propagation

Errors in the cluster frequency counts were estimated at $\Delta N_s/N_s = 10\%$ based on the significant figures at which the data have been collected. In this chapter appendix, we calculate approximate error estimates for other quantities derived from this raw size distribution data. In our calculations we ignore the uncertainty in the measured cluster size, s, as the data have been collated in bins which we assume to be wide enough to make errors in the cell number negligible. In other words, we assume the probability of a cluster being counted in the wrong size bin to be low. In the calculations that follow, we use conventional error propagation, based on Taylor expansions of functions of random variables. We denote the error in x by Δx.

Error in cell number and average cluster size

Cell numbers were calculated from cluster frequency counts, N_s, and cluster sizes, s, as $N(t) = \sum_s N_s(t)s$. Thus the squared error in $N(t)$ is given by

$$(\Delta N(t))^2 = \sum_s (\Delta N_s)^2 s^2,$$

assuming independent errors in different bins. The squared error in the total number of clusters, $N_C = \sum_s N_s$, is $(\Delta N_C)^2 = \sum_s (\Delta N_s)^2$. Thus the squared relative error in the average cluster size, $\langle s(t)\rangle = N(t)/N_C(t)$, is

$$\left(\frac{\Delta\langle s(t)\rangle}{\langle s(t)\rangle}\right)^2 \approx \left(\frac{\Delta N(t)}{N(t)}\right)^2 + \left(\frac{\Delta N_C(t)}{N_C(t)}\right)^2 - 2\frac{|\Delta N(t)||\Delta N_C(t)|}{N(t)N_C(t)},$$

where the last term stems from the covariance of the errors between the total number of cells, N, and the total number of clusters, N_C.

Error in cluster size distribution

The normalised cluster size distribution is $n_s = N_s/N_C$, with $N_C = \sum_k N_k$. We have dropped the explicit time-dependence to be more concise. As the bin count, N_s, and the sum of all bin counts, N_C, are not independent, propagating the uncertainty takes a little more care. Starting from the partial derivative

$$\frac{\partial n_s}{\partial N_j} = \frac{\delta_{sj}}{N_C} - \frac{n_s}{N_C},$$

and using this in the expansion $\Delta n_s = \sum_j \frac{\partial n_s}{\partial N_j}\Delta N_j$, we can rearrange and divide by n_s to arrive at

$$\frac{\Delta n_s}{n_s} = \frac{\Delta N_s}{N_s} - \sum_j \frac{\Delta N_j}{N_C}.$$

Hence we can calculate the uncertainty in n_s as the (mean) squared relative error,

$$\left(\frac{\Delta n_s}{n_s}\right)^2 = \left(\frac{\Delta N_s}{N_s} - \sum_j \frac{\Delta N_j}{N_C}\right)^2.$$

If we assume the errors in different cluster sizes to be independent, then on average $\Delta N_j \Delta N_s = 0$ for $j \neq s$ (random errors from independent variables are uncorrelated), the cross-term simplifies to $-2\sum_j(\Delta N_j/N_C)(\Delta N_s/N_s) = -2\Delta N_s^2/N_C N_s$, and thus

$$\begin{aligned}\left(\frac{\Delta n_s}{n_s}\right)^2 &= \sum_j \left(\frac{\Delta N_j}{N_C}\right)^2 + \left(\frac{\Delta N_s}{N_s}\right)^2 - \frac{2\Delta N_s^2}{N_C N_s} \\ &= \left(\frac{\Delta N_C}{N_C}\right)^2 + \left(\frac{\Delta N_s}{N_s}\right)^2 (1 - 2n_s).\end{aligned}$$

To verify that the above expression is always positive, note that $n_s \leq 1$, and when $n_s = 1$, then $n_k = 0$ for all $k \neq s$, in which case $N_C = N_s$, and the relative error is zero when it is smallest.

Error in the cluster frequency counts after correcting for non-constant cell numbers

When we correct the cluster frequency counts to take into account non-constant cell numbers, we start with $\tilde{N}_s = N_s/N = N_s/(\sum_j N_j j)$ and proceed in a similar manner as above, expanding $\Delta\tilde{N}_s$ in its components,

$$\begin{aligned}\Delta\tilde{N}_s &= \sum_j \frac{\partial \tilde{N}_s}{\partial N_j}\Delta N_j = \frac{\Delta N_s}{N} - \sum_j \frac{N_s j}{N^2}\Delta N_j \\ &= \tilde{N}_s \left(\frac{\Delta N_s}{N_s} - \sum_j \frac{j}{N}\Delta N_j\right).\end{aligned}$$

Then, making use of the independency of the individual error contributions, we obtain

$$\begin{aligned}\left(\frac{\Delta\tilde{N}_s}{\tilde{N}_s}\right)^2 &= \left(\frac{\Delta N_s}{N_s} - \sum_j \frac{j}{N}\Delta N_j\right)^2 \\ &= \left(\frac{\Delta N_s}{N_s}\right)^2 + \left(\sum_j \frac{j}{N}\Delta N_j\right)^2 - 2\frac{\Delta N_s}{N_s}\sum_j \frac{j}{N}\Delta N_j.\end{aligned}$$

Identifying the second term as $(\Delta N/N)^2$ and rearranging, we finally arrive at

$$\left(\frac{\Delta\tilde{N}_s}{\tilde{N}_s}\right)^2 = \left(\frac{\Delta N}{N}\right)^2 + \left(\frac{\Delta N_s}{N_s}\right)^2 (1 - 2s\tilde{N}_s).$$

We can again verify positivity by recognising that, by definition, $s\tilde{N}_s = sN_s/N \leq 1$, so that $\left(\Delta\tilde{N}_s/\tilde{N}_s\right)^2 \geq (\Delta N/N)^2 - (\Delta N_s/N_s)^2 \geq 0$. We ignore further error propagation for quantities calculated from $\tilde{N}_s$, such as $\langle\tilde{s}\rangle$ or $\tilde{N}_C$, and simply use the above formulae with $\tilde{N}_s$ instead of N_s when correcting for non-constant total cell numbers.

Error in rescaled cluster size distributions

We write the cluster size distribution, n_s, scaled by the mean cluster size, $\langle s\rangle$, as $\bar{n}_s = \langle s\rangle n_s = \sum_j n_j j n_s$. Proceeding as before, we expand

$$\Delta\bar{n}_s = \sum_j \frac{\partial\bar{n}_s}{\partial n_j}\Delta n_j = \sum_j j\Delta n_j n_s + s\Delta n_s n_s,$$

and then calculate the mean squared error, assuming that, on average, $\Delta n_i \Delta n_j = 0$ for $i \neq j$, as

$$\left(\frac{\Delta\bar{n}_s}{\bar{n}_s}\right)^2 = \left(\frac{\sum_j j\Delta n_j + s\Delta n_s}{\sum_j j n_j}\right)^2 = \frac{\sum_j (j\Delta n_j)^2 + 3s^2(\Delta n_s)^2}{\langle s\rangle^2}.$$

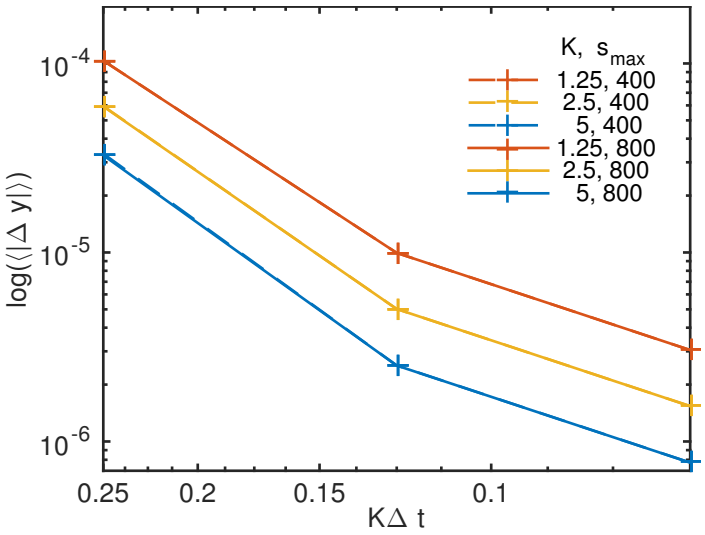

Figure 5.12: Numerical solution to the Smoluchowski equations (5.1) with the Brownian kernel (5.4) for various rates $K = K_{1,1}/4$ (different colours) and size cut-offs, $s_{\max}$. Note that the dashed and solid lines overlap, demonstrating sufficiency of the lower size cut-off. Time-steps were chosen inversely proportional to rates, $\Delta t \sim K^{-1}$ (for stability), and mean absolute difference calculated with respect to a solution generated with $\Delta t_{\min} = K^{-1}2^{-5}$.

Chapter 6

Size-regulation in aggregation processes through crowding

"The devil is in the mesoscale."
Philip Maini, (20.07.2015)

In the previous chapter we described the self-organisation of dissociated mouse skin cells back into functional skin *in vitro*. We found that the clustering of epidermal cells was quantitatively captured by a model describing them as randomly moving, irreversibly aggregating clusters. However, the quality of the match between data and theory decreased drastically at the 48 hour time-point, namely when the clusters of epidermal cells seem to have stopped growing and their size distribution narrowed to a peak. The coagulation model would have predicted the aggregation process to continue (until epidermal and dermal cells have completely separated into two layers), without a characteristic cluster size standing out from the size distribution.

We took this as a clue that, at around 48 hours, the system is transitioning between different dynamics, and hypothesise that the interaction with dermal cells (hitherto ignored in the aggregation model) contributes to the observed size control of epidermal cell aggregates. In this shorter chapter, we explore the idea that dermal cells hinder the movement of epidermal cells through volume exclusion, and do so in a different way for large and small aggregates. Thus, we test how size control can be achieved in aggregation processes through the trapping of larger clusters.

6.1 Crowding effects

Motivation for investigating crowding effects in the motion of clusters can be found in the tracking data of epidermal cells. If we calculate the displacement of cells (which

may be part of a cluster) and normalise for changes in mean and variance, we see non-Gaussian distributions that become more narrow over time (Fig. 6.1). In the case of a particle undergoing thermally driven diffusion, displacement distributions that are narrower than Gaussians provide evidence for trapping, i.e., reduced movement due to volume exclusion. Here, however, cells are assumed to be actively moving and thus their distribution of displacements need not be Gaussian in the first place, so the shape of the distribution does not by itself provide evidence for crowding. Still, the narrowing of the empirical velocity distributions (Fig. 6.1) with time, which is proportional to cluster size (Fig. 5.7), motivates considering crowding effects. We opt not to characterise anomalous diffusion exponents from mean-square-displacement data, as recent work has shown that much larger amounts of data than we have available are required to reliably estimate these exponents (Baker and Simpson, 2015), rendering this an infeasible pursuit.

Another recent study found smaller obstacles are more effective at restricting movement (Ellery *et al.*, 2014). This reinforces our hunch that if dermal cells in any way hinder the movement of epidermal cells through volume exclusion, then larger clusters will be slowed down, or trapped, to a greater extent. This would change the size dependence of the aggregation rates presented in Chapter 5.2.1 in a non-trivial way, and thus volume exclusion holds the potential to account for size regulation of clusters.

To explore this idea more rigorously, let us represent the dermal cells as inert, i.e., non-aggregating, particles that affect the diffusion of the epidermal cells, the aggregating particles, through excluded volume (in this case, hard core repulsion). Other kinds of volume exclusion could be considered, and we discuss this in Section 6.2. Consider now the diffusion of a single epidermal cell in the mixture of epidermal and dermal cells. From the approach of Bruna and Chapman (2012b,a) (using reflective boundary conditions and matched asymptotic expansions), the concentration-dependent "self-diffusion" coefficient of a single tagged particle in a mixture of N_{epi} particles of the same type and N_{der} particles of a different type, in a d-dimensional unit volume can be calculated to be

$$\tilde{D}_{\text{epi}} = D_{\text{epi}} \left(1 - (N_{\text{epi}} - 1)(2r_{\text{epi}})^d \frac{\pi}{d} - N_{\text{der}}(r_{\text{epi}} + r_{\text{der}})^d \frac{2\pi}{d} \frac{D_{\text{epi}}}{D_{\text{epi}} + D_{\text{der}}} \right), \quad (6.1)$$

where $D_{\text{epi}}, D_{\text{der}}$ are the unhindered diffusivities of epidermal and dermal particles, respectively, r_{epi} is the epidermal particle radius and r_{der} the dermal particles radius.

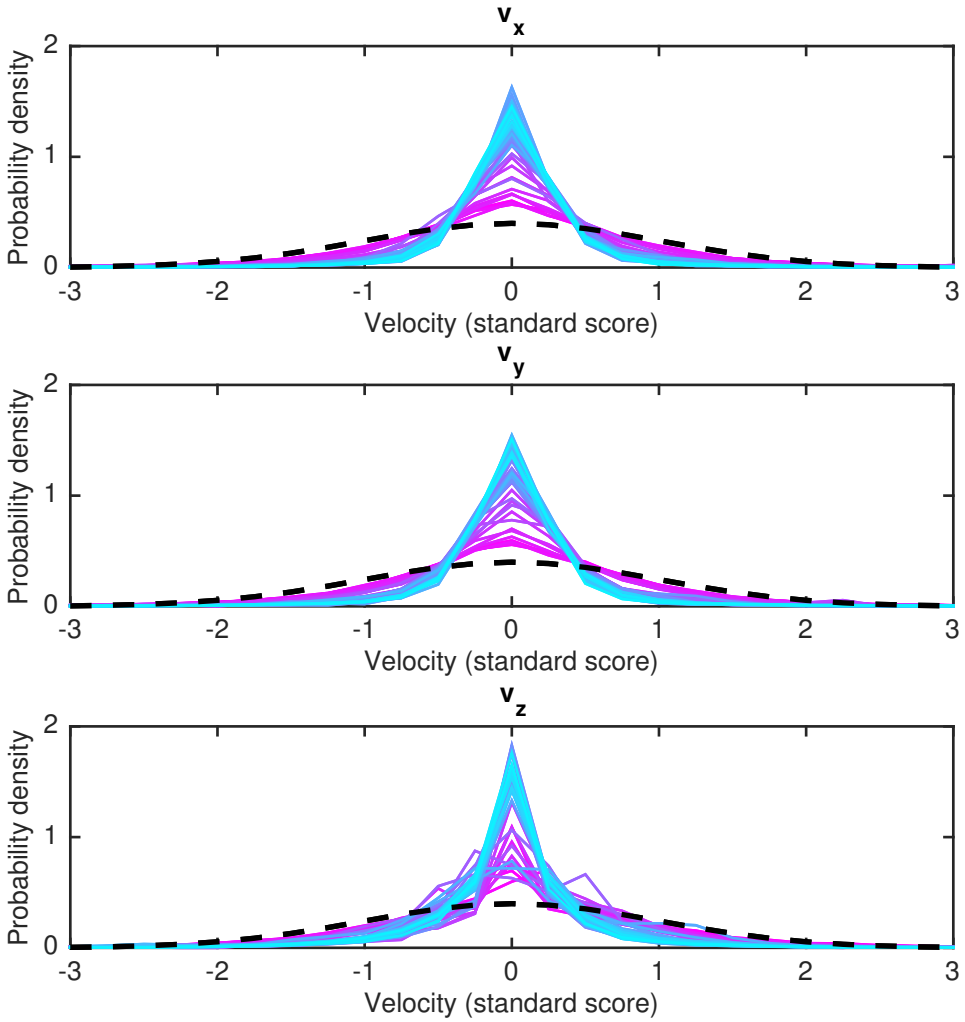

Figure 6.1: Velocity distributions of tracked epidermal cells for the first 72 hours of the experiment, with standard normal distributions (dashed lines) for comparison. Velocities were normalised to standard score, $z = (v - \mu_v)/\sigma_v$, to adjust for changes in median μ_v and variance σ_v over time. Lines are coloured according to time bin, from 0 hours (magenta) to 72 hours (cyan). Note that the spatial resolution of the image data is lower in the z-axis.

We make the assumption that the diffusion of clusters is hindered on timescales shorter than aggregation. In other words, we are considering how crowding by non-aggregating cells hinders the movement of a cell cluster before it meets another aggregating cluster with which to merge. Thus, let us ignore the homotypic interactions (with particles of the same type), by removing the second term on the right-hand side in (6.1), equivalent to setting $N_{\text{epi}} = 1$. This gives

$$\tilde{D}_{\text{epi}} = D_{\text{epi}} \left(1 - N_{\text{der}} (r_{\text{epi}} + r_{\text{der}})^d \frac{2\pi}{d} \frac{D_{\text{epi}}}{D_{\text{epi}} + D_{\text{der}}} \right), \tag{6.2}$$

where we now take r_{epi} to be the radius of a multicellular epidermal cluster, and r_{der} that of a single dermal cell. This expression can now be used to construct a modified version of the Brownian aggregation kernel. As before, we proceed by investigating the size scaling in this new "crowded kernel".

6.1.1 Scaling analysis

If we again assume a Stokes-Einstein relation for the diffusivity of a cluster of s cells, the scaling is, as in Section 5.2.2.1, $D_{\mathrm{epi}} \sim s^{-\frac{1}{d}}$. With $r_{\mathrm{epi}} = r_{s=1}s^{\frac{1}{d}}$, where $r_{s=1}$ is the radius of a single epidermal cell, i.e., a cluster of size one, we obtain $(r_{\mathrm{epi}} + r_{\mathrm{der}})^d = (s^{\frac{1}{d}}\xi + 1)^d r_{\mathrm{der}}^d \sim (s + \mathcal{O}(s^{\frac{d-1}{d}}))r_{\mathrm{der}}^d$ to leading order in s, where $\xi = r_{\mathrm{s=1}}/r_{\mathrm{der}}$ is a constant, which we can assume to be equal to one since dermal and epidermal cells are roughly of the same size. Inserting these expressions into (6.2), and keeping the leading order of s in each term, we arrive at

$$\tilde{D}_{\mathrm{s}} \sim s^{-\frac{1}{d}} \left(1 - \frac{\rho}{2^{d-2}} \frac{s^{1-\frac{1}{d}}}{s^{-\frac{1}{d}} + \phi}\right), \tag{6.3}$$

where we have absorbed numerical factors of proportionality into the constants $\rho = N_{\mathrm{der}} r^d 2^{d-1}\pi/d$, the volume fraction[1] of dermal cells (with $r = r_{\mathrm{der}} = r_{\mathrm{s=1}}$), and $\phi = D_{\mathrm{der}}/D_{s=1}$, the ratio of dermal, D_{der}, and epidermal, $D_{s=1}$, monomer diffusivities. We can readily see that there is a value $s = s_c$ for which $\tilde{D}_{\mathrm{epi}}(s_c) = 0$. From this, we can deduce two things: (1) there is no homogeneous scaling of the form (5.5) that holds for all s; and (2) if both $i \geq s_c$ and $j \geq s_c$, then $K_{ij} = 0$. Thus, we have a situation in which clusters of a certain size stop merging with other clusters of the same or larger size due to hindered diffusion. Note, however, that this does not mean aggregation stops at $s = s_c$, since clusters can still grow through the flux of smaller clusters onto the large, stationary ones. The existence, and form, of a final cluster size distribution with no further aggregation therefore requires more careful consideration. But first, let us verify the two claims we have just made.

[1]Note that the volume fraction which determines the limit of validity of the method by Bruna and Chapman (2012b,a) is calculated slightly differently. There, we need to instead consider the volume fraction unavailable to the diffusing tracer particle, i.e., we would increase the effective radius of obstacles by that of the tracer particle.

6.1.2 The crowded kernel

Inserting (6.3) into the expression for the Brownian kernel, (5.4), we can separate[2] the size-scaling of the crowded kernel, $\tilde{K}_{ij}$, into that of the Brownian kernel, K_{ij} (given by (5.4)), and a term resulting from the crowding, i.e.,

$$\tilde{K}_{ij} \sim K_{ij} - \frac{\rho}{2^{d-2}} \left(\frac{i^{1-\frac{2}{d}}}{i^{-\frac{1}{d}} + \phi} + \frac{j^{1-\frac{2}{d}}}{j^{-\frac{1}{d}} + \phi} \right) (i^{\frac{1}{d}} + j^{\frac{1}{d}}). \tag{6.4}$$

Here we can see that for non-zero volume fractions, $\rho > 0$, of mobile ($\phi > 0$) obstacles, there is no scaling of the form (5.5). In the limit of $D_{s=1} \gg D_{\text{der}}$, i.e., $\phi \to 0$, the homogeneous scaling ansatz for the second term gives $\omega = 1/2$, but the first term has $\omega = 0$ as before, so overall the scaling ansatz does not hold in the limit of very slowly diffusing obstacles either. We only recover scaling for the limiting case of very fast obstacles, $\phi \to \infty$, in which case the crowded kernel reduces back to the Brownian kernel.

6.1.3 Approximating the critical cluster size

In order to investigate the long time behaviour of a system of aggregating particles with the above crowded kernel (6.4), it is useful to consider the limit where the motility of a cluster becomes negligible due to trapping by dermal cells. So, let us find s_c such that $\tilde{D}_{s_c} = 0$. Referring back to (6.3), we can rearrange to get (to leading order in s_c)

$$s_c^{-\frac{1}{d}} + \phi = \frac{\rho}{2^{d-2}} s_c^{1-\frac{1}{d}},$$

which for $\rho \neq 0$ results in the equation

$$s_c^{1-\frac{1}{d}} - \frac{2^{d-2}}{\rho} s_c^{-\frac{1}{d}} - \frac{2^{d-2}\phi}{\rho} = 0,$$

and for the relevant case of $d = 3$,

$$s_c^{\frac{2}{3}} - \frac{2}{\rho} s_c^{-\frac{1}{3}} - \frac{2\phi}{\rho} = 0. \tag{6.5}$$

The critical cluster size s_c thus depends on the ratio of epidermal and dermal diffusivities, ϕ, which we assume to be one, as well as the volume fraction of obstacles, i.e., dermal cells. Solutions to Eq. 6.5 for a range of parameters are plotted in

[2] Alternatively, we can write the crowded kernel as

$$\tilde{K}_{ij} = K_{ij} \left[1 - \frac{\rho}{2^{d-2}} \left(\frac{i^{1-\frac{2}{d}}}{i^{-\frac{1}{d}} + \phi} + \frac{j^{1-\frac{2}{d}}}{j^{-\frac{1}{d}} + \phi} \right) \frac{i^{\frac{1}{d}} j^{\frac{1}{d}}}{i^{\frac{1}{d}} + j^{\frac{1}{d}}} \right].$$

Fig. 6.2. For an order-of-magnitude estimate (our results in this section are approximations for large clusters), consider that in the experiment mentioned in Chapter 5.3, $N_{\mathrm{der}} = 9 \times 10^6$ dermal cells were suspended in a droplet of diameter of 0.8 cm, and a height of 400 μm, i.e., roughly $V = 20\,\mu$l. If cells are approximately spherical, with a radius of $r = 5\,\mu$m, this gives a volume fraction of about $\rho = N_{\mathrm{der}} 4\pi r^3/3V \approx 0.24$, which results in an estimate for the critical cluster size of $s_c \approx 36$ cells (solving[3] Eq. (6.5) in WOLFRAM MATHEMATICA). This may seem unexpectedly low, given the fact that clusters an order of magnitude larger are observed in the data. However, the estimate of the critical cluster size is sensitive to the volume of the cell droplet, which is decreasing as the droplet settles into the culture insert over the first day (fluid permeates through the barrier below the cells). Over the first day, the height of the droplet has been observed to drop from around 900 μm to the aforementioned 400 μm (Lei, personal communication). With this larger value the droplet of cells has a volume of 45 μl, and a volume fraction of $\rho \approx 0.1$, giving $s_c \approx 118$ cells. Based on the observed cluster sizes, this seems like a more realistic estimate of the critical cluster size. Presumably, the later (i.e. lower) value of the estimated volume is more likely to be relevant for cluster size control, the effects of which are only noticeable from day 2, as we showed in Chapter 5.2.1. This puts the prospect of putting strong quantitative bounds on the models in this chapter given the current experimental data into question. Nevertheless, we can proceed to check how this model of aggregation with crowding compares to that studied in Chapter 5.3, and whether it at least captures the phenomenology of size regulation in arrested aggregation that we aimed for.

Note that the accuracy of the result of Bruna and Chapman (2012a) is expected to decrease with increasing volume fractions, but only break-down at $\rho = 0.5$. The error in the approximations involved in this method has been calculated exactly for the case of periodically distributed, immobile obstacles (Bruna and Chapman, 2015), and in three dimensions the expression corresponding to (6.1) was found to be accurate for the whole range of valid volume fractions. Thus, if hard core repulsion is an appropriate way to approximate the cell-cell interactions, then we expect that

[3]The real-valued solution to Eq. (6.5) is given by

$$s_c = \frac{2}{\rho}\left(1 + \frac{2\phi^2}{3^{\frac{1}{3}}\rho\left(\frac{9}{\rho} + \frac{\sqrt{3(27\rho - 8\phi^3)}}{\rho^{\frac{3}{2}}}\right)^{\frac{1}{3}}} + \frac{\phi}{3^{\frac{2}{3}}}\left(\frac{9}{\rho} + \frac{\sqrt{3(27\rho - 8\phi^3)}}{\rho^{\frac{3}{2}}}\right)^{\frac{1}{3}}\right).$$

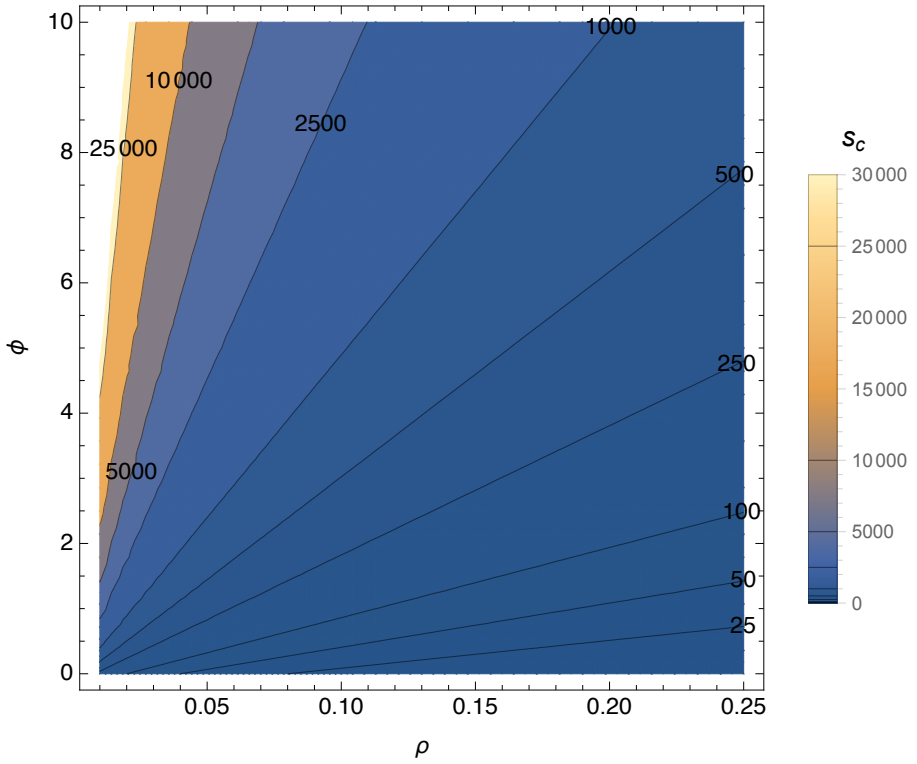

Figure 6.2: The critical cluster size for which $\tilde{D}(s_c) = 0$ (6.3) as a function of the obstacle volume fraction, ρ, and the ratio of monomer diffusivities, ϕ, given by the solutions to $s_c^{\frac{2}{3}} - s_c^{-\frac{1}{3}} 2/\rho - 2\phi/\rho = 0$.

the results quoted in Eq. (6.1) should be an accurate approximation of the reduced diffusivity of cell clusters. The keen reader may wonder how it can be that we consider the case where a cluster stops moving due to crowding effects, even though the work by Bruna and Chapman (2012a) is only valid far from the jamming transition. Here, we are not in a jammed state, as smaller clusters of epidermal cells and single dermal cells are still moving. It is only large enough clusters that may have slowed down sufficiently (if our hypothesis is correct) to effectively stand still. In any case, the limit of zero diffusivity for the critical cluster size s_c should only be seen as a first-order approximation to explore the effect of physically inhibited movement of larger clusters on the aggregation process.

6.1.4 Comparing the Brownian and crowded kernels

With the above approximation of how crowding affects cluster movement at different sizes, up to the limiting case of total inhibition of movement, were are now in a position to check how the trapping affects aggregation rates. Comparing with the

Brownian kernel (Fig. 6.3), we see similar aggregation rates between small and large clusters, but a decrease in the aggregation rates of large clusters with intermediate sized clusters, and no aggregation between clusters above the critical cluster size.

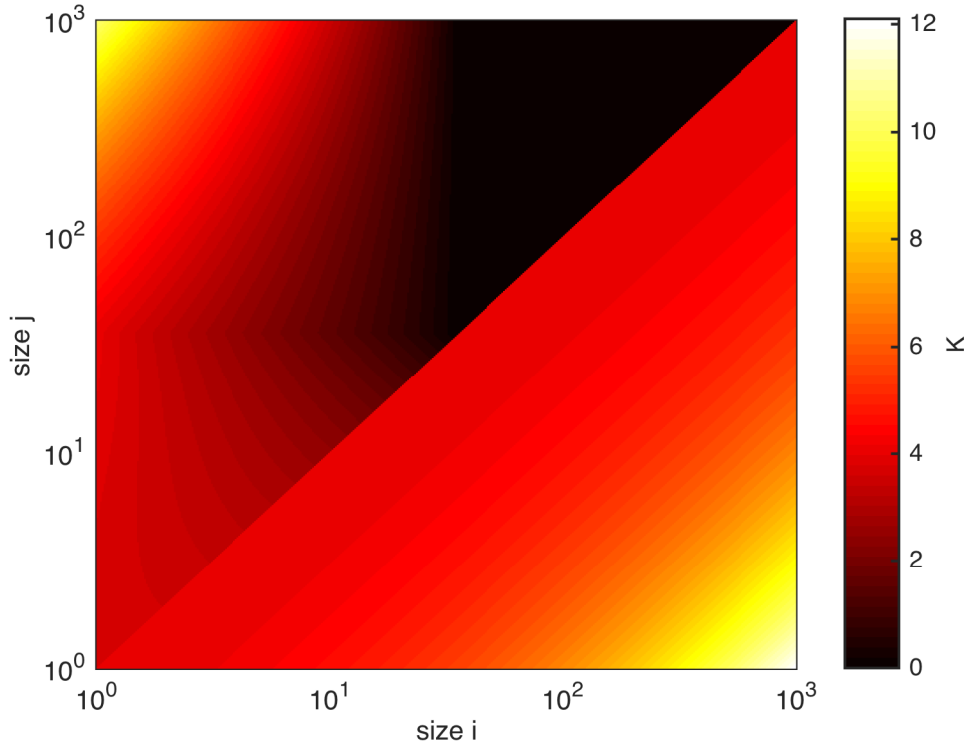

Figure 6.3: The Brownian (5.4) (lower triangle) and crowded (6.4) (upper triangle) aggregation kernels, for $\phi = 1$ and $\rho = 0.24$. Both kernels can be seen to increase aggregation rates between small and large clusters compared to the constant kernel. The crowded kernel, however, slows down aggregation between large aggregates due to inhibited diffusion (see region of $K \to 0$ in right half of upper triangle).

6.1.5 Numerical solution to the aggregation equations with crowding effects

Having constructed a rate kernel for aggregation under crowding by inert particles, we now show that this can indeed impose an upper limit on cluster size in the late stage of aggregation without affecting the ability to match the data on shorter time scales, i.e., within the first 36 hours. Note that we have introduced an additional parameter, the volume fraction of obstacles, ρ. Ideally, this is not a parameter we want to fit, but one to be estimated from the data. However, we might still like to know how the quality of our fit depends on the estimate for ρ. Trying a small number

of values for ρ, we can see that an RMSE as low as with the Brownian kernel can easily be achieved. In fact, we achieve a slightly better fit than with the Brownian kernel, albeit at a lower volume fraction than the estimated one, but it is unsurprising that we can get a "better" fit given the additional parameter.

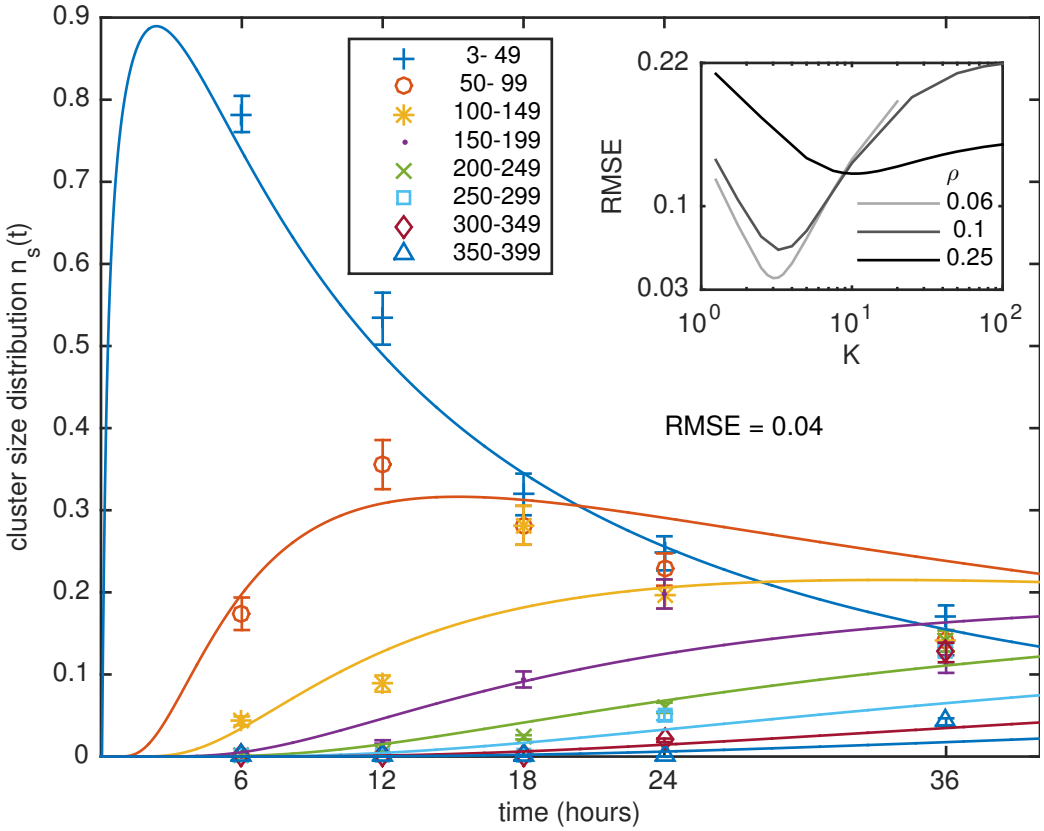

Figure 6.4: Crowded kernel (6.4) solution and cluster size distributions for the first 36 hours. The least-squares value for the fitted parameter was $K = 3.0\,\mathrm{h}^{-1}$ (inset). Error bars reflect estimated 10% counting accuracy.

6.1.5.1 Size control through trapping of large clusters

From the structure of the crowded kernel (Fig. 6.3), we expect that the aggregation process will give rise to a size distribution that, at long times converges on a distribution peaked around some size $s > s_c$, which is exactly the desired effect of size regulation we hoped for. To verify this, we can solve the aggregation equations with crowding numerically for long times (or high aggregation rates). Starting with the best fit solution from Fig. 6.4 and extrapolating to the 48 hour time-point (where we first see evidence for size regulation in the experimental cluster size counts), we see a peak in the distribution (which does not occur for aggregation without crowding),

but at the wrong spatial scale (Fig. 6.5). Also, recall that this solution with $\rho = 0.06$ had a lower volume fraction than the values of $\rho \approx 0.1$ to 0.24 that were estimated for the experiment.

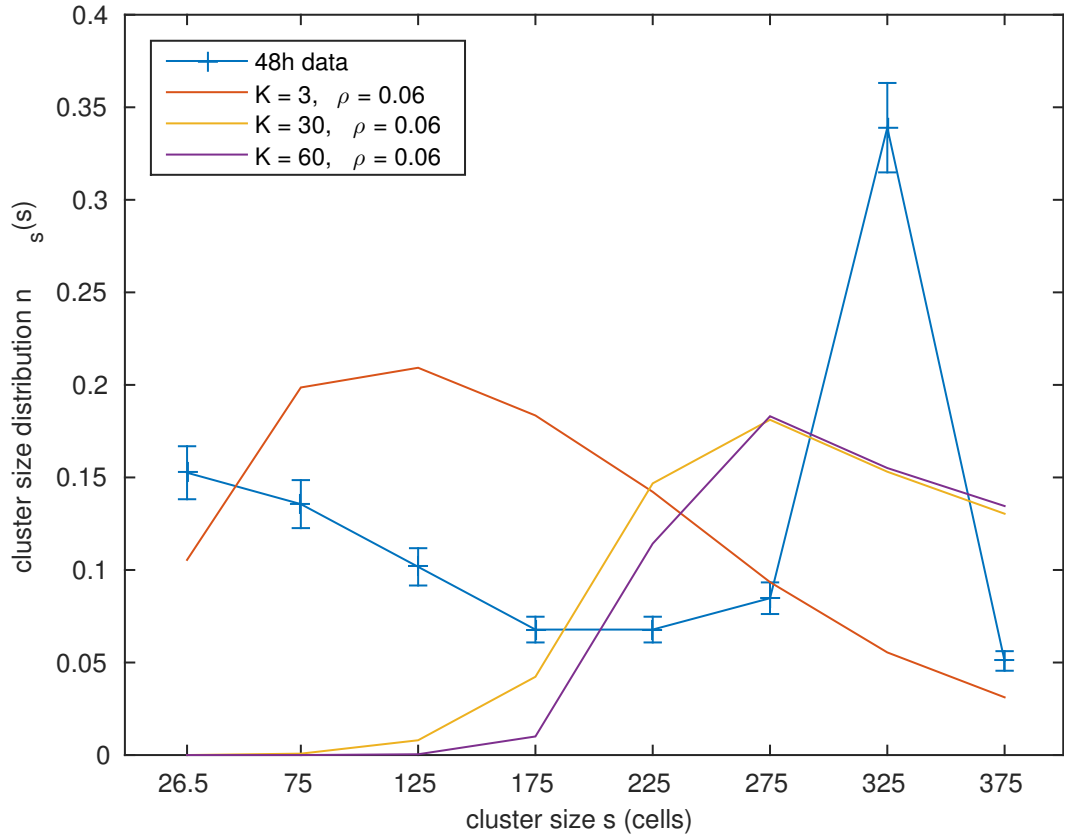

Figure 6.5: Size distributions at $t = 48$ hours, from experimental data, and for the numerical solutions to aggregation with crowding at different aggregation rates (equivalent to different effective times, with higher rates corresponding to later times). The critical cluster size for $\rho = 0.06$ is $s_c \approx 241$.

Going to higher aggregation rates, i.e., longer times, shows that the peak in the size distribution shifts to the right and converges, but not to the experimentally observed distribution (Fig. 6.5). The position of the final peak in the cluster size distribution is a function of the obstacle volume fraction, ρ, and thus can, in principle, be adjusted to match the experimental data. However, we can clearly see that the tails of the distribution are shorter in the model than in the data, and a full match across the whole support of the distribution is unlikely to be achievable. As we mentioned before, considering ρ as a fitting parameter is not our intention, as this should be estimated from prior knowledge.

6.2 Discussion

In this chapter we explored the phenomenon of size regulation in the aggregation processes, pursuing the hypothesis that this might be driven through the trapping of large clusters by inert monomers, which was motivated by our experimental application of mouse skin reconstitution in Chapter 5. Since the movement of large clusters is affected more by the volume exclusion effect, their aggregation rates decrease (Fig. 6.3) with size in a way that eventually arrests their growth (Fig. 6.5).

After verifying that this crowded aggregation model fits the clustering of mouse epidermal skin cells (Fig. 6.4), we attempted to predict the size distributions at late times (Fig. 6.5), where our models without crowding (Chapter 5) ceased to work. Quantitatively, the new model incorporating crowding effects was also unsuccessful. Qualitatively, we achieved exactly the desired effect of size regulation (which does not feature in the dynamics of clustering clusters), if not at the spatial and temporal scales observed in this experimental application. Below we discuss possible reasons for this shortcoming.

6.2.1 Different kinds of volume exclusion

In our description of aggregation with crowding, we considered volume exclusion in the form of hard core repulsion. While cells must certainly obey volume exclusion, it is possible that hard core repulsion is not a good approximation of their interaction, for a number of reasons. The ability of cells to change shape could result in low repulsion at distances below a cell diameter, but higher repulsion at distances smaller than the diameter of a cell nucleus. For example, Binny *et al.* (2015) implement volume exclusion through Gaussian kernels that weight the exclusion interaction between cells as a function of distance. Alternatively, cells could sense their surroundings, e.g., with protrusions, and either move up to an obstacle (but without "bouncing off"), or not attempting to move at all if an obstacle is encountered during sensing. This latter form of volume exclusion and its role in collective cell movement has been studied by Dyson and Baker (2015), who found the same resulting PDEs as Bruna and Chapman (2012b,a) for diffusion of a population of one type of cell, but different non-linearities for multiple populations. At first sight, this calls into question our use of the result by Bruna and Chapman (2012a) for the crowded diffusion of a binary mixture of particles. However, we do not investigate the dispersal of a population of cells (which, in our case, are confined to a well-mixed liquid droplet), but the diffusion of a tracer cluster within the population, which, unlike the dispersal of the

whole population, cannot increase due to crowding effects. In the work by Dyson and Baker (2015), the effects we are interested in, namely the movement of one type of cell being affected by a uniform distribution of another type of cell, is a higher order effect not included in their approximations. It may be of interest for future work to include these higher order effects to see if there is a qualitative difference between these two kinds of volume exclusion, i.e., hard core repulsion and aborted movement, for the problem of size regulation in aggregation processes.

6.2.2 Cell-cell interaction mechanisms

Interaction between epidermal aggregates and dermal cells could be mediated through mutual binding of both cell types to ECM. Indeed, transcriptomics analysis has shown increased collagen and laminin expression from 48 to 96 hours, as well as increased expression of MMP genes (Lei *et al;*, in preparation), which might facilitate cell movement and the merging of aggregates in an increasingly dense matrix environment. In contrast to hard core volume exclusion, the interaction of cells through ECM may be more appropriately modelled by considering viscoelastic effects. The integration of these interactions into models of aggregation processes remains the scope of future work.

It is also conceivable that cells actively change their interaction properties, triggering a change in the dynamics of self-organisation. In the skin reconstitution experiment, cell-cell adhesion molecules (cadherins) are at first rapidly decreasing and then slowly increasing in expression (Lei *et al;*, in preparation). This indicates that the cells' binding characteristics are changing, but to understand in what way, we need to better determine the relative role of different cadherins in this process through functional perturbations. In a recent theoretical study, Redner *et al.* (2013) have charted the phase space of aggregation outcome as a function of attraction between and propulsion of active particles. This suggests the possibility that these might be relevant parameters that control the halting of, and reentry into, phase separation. An extension of this work for two species systems is a potential avenue of pursuit for future work.

In summary, our model of aggregation with crowding effects may not have captured the epidermal cell clustering data quantitatively, suggesting that additional mechanisms also underlie the observed morphological dynamics in mouse skin reconstitution. However, we showed a generally feasible mechanism of size regulation in mixed aggregation processes, which might be relevant for other applications.

Chapter appendix

Convergence and stability of numerical solutions

We solve the aggregation equations with the crowded kernel as we did for the Brownian kernel (Section 5.2.1.3), and again verify convergence when decreasing the time-step by taking the mean absolute difference of abscissae over the whole time and size range of interest with respect to the solution with the smallest time-step. We find convergence for the time-steps chosen, as before, without having to increase the size cut-off, $s_{\max}$, for the infinite system of equations.

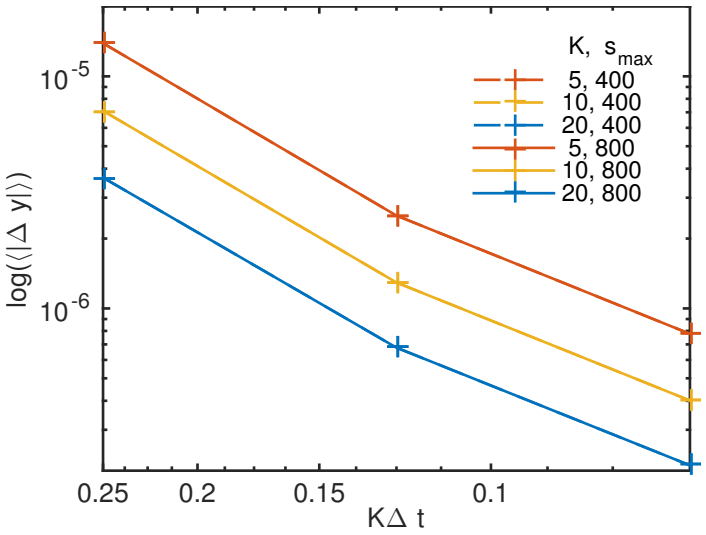

Figure 6.6: Convergence of numerical solution to the Smoluchowski equations (5.1) with the crowded kernel (6.4) for $\phi = 1$, $\rho = 0.25$, various rates $K = K_{1,1}$ (different colours) and size cut-offs $s_{\max}$. Note that the dashed and solid lines overlap, demonstrating apparent sufficiency of the lower size cut-off. Time-steps were chosen inversely proportional to rates, $\Delta t \sim K^{-1}$ (for stability), and mean absolute difference calculated with respect to solution with $\Delta t_{\min} = K^{-1}2^{-5}$.

When considering the long-time behaviour of the size-distributions (Section 6.1.5.1), however, we need to check for convergence differently, for two reasons: (1) At long times (or faster aggregation), a greater mass of particles has concentrated at larger sizes, increasing the error in the size cut-off when s_c is of the same order as $s_{\max}$. (2) In our previous convergence analyses, the low error may have been dominated by early time-points, when most of the mass was concentrated at $s \ll s_{\max}$. If we are interested in the accuracy of the numerical solution for a particular (late stage) time-point, we need to calculate the convergence accordingly (Fig. 6.7). When we do

this for a high aggregation rate (corresponding to long-time behaviour), we find we do have to increase the size cut-off to $s_{\max} = 800$. This was done for Fig. 6.5.

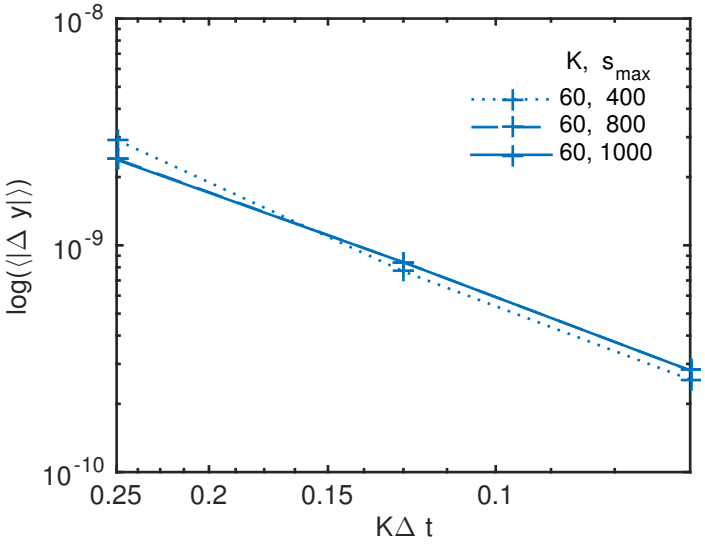

Figure 6.7: Convergence of numerical solution to the Smoluchowski equations (5.1) with the crowded kernel (6.4) for $\phi = 1$, $\rho = 0.06$, rates $K = 60\,\mathrm{h}^{-1}$ and various size cut-offs $s_{\max}$. Note that the dashed and solid lines overlap, demonstrating sufficiency of the intermediate size cut-off. Time-steps were chosen inversely proportional to rates, $\Delta t \sim K^{-1}$ (for stability), and mean absolute difference calculated for the final time-point ($t = 48$ hours) only, with respect to solution with $\Delta t_{\min} = K^{-1}2^{-5}$.

Chapter 7

Conclusion

The central aim of this thesis has been to contribute to the understanding of collective cell behaviour in paradigm experimental models for developmental biology through the use of mathematical and computational approaches. We focussed on two specific experimental systems. First, collective neural crest cell migration in chick embryos, and second, an *in vitro* assay for reconstituting functional mouse skin from dissociated cells. In these systems, we investigated how population heterogeneity, environmental signals and cell-cell interactions facilitate movement and organisation of a cell population as a whole.

7.1 Summary

In Chapter 2, we introduced the relevant biology of cell migration and the neural crest, motivating our choice of model system and arguing the case for wider definition of collective cell migration that includes multicellular streaming. We surveyed the literature on computational models, explaining why we elected to extend the efforts of McLennan *et al.* (2012).

Our modifications and extensions to the modelling framework were the subject of the first part of Chapter 3. Using this improved model we simulated cranial neural crest migration in a cell-induced chemoattractant gradient with leader-follower cell heterogeneity. We found that higher migration efficiency could be achieved with lower number of leaders, predicting that the leader cell phenotype seen *in vivo* may be confined to the most invasive front of the migratory stream. This was confirmed by single-cell gene expression measurements, which led to the identification of a molecular profile associated with these "trailblazer cells". Perturbing this gene expression to hypothetically force trailing cells into a leader state affected migration in a qualitatively similar way to our computational experiments, by reducing the number of

cells but not the distance migrated. Together, these results led us to conclude that chick cranial neural crest cell migration can be guided by just a few cells, narrowly confined to the invasive front (McLennan *et al.*, 2015a). Thus, we have improved our understanding of how heterogeneity in a cell population can help them migrate in an otherwise homogeneous environment.

Following this train of thought into Chapter 4, we interrogated our hypothesis that this leader-follower heterogeneity is established by the presence of the directional signal, in the form of a chemoattractant gradient. This required an extension to our computational model, the integrate-and-switch mechanism, in which cells switch states based on the time of exposure to a gradient, but with hysteresis. To parameterise the timescale of cell state transitions in our model, we helped to design and analyse an experiment to measure gene expression in chick cranial neural crest cells in response to timed exposure and removal of VEGF *in vitro*, the main directional cue of these cells, which revealed expression changes in as short a time as four minutes. This allowed us to use our model in parallel with *in vivo* experiments to alter the chemoattractant distribution along the stream of migrating cells. Simulations and experiments agreed in the way they affected migration through rerouting cells at the back of the stream towards ectopic sources of VEGF. Through close integration of theory and experiment, this work has characterised VEGF as one of the environmental signals that dynamically establish functional heterogeneity in the chick cranial neural crest cell population. We started with a homogeneous population of cells in a homogeneous environment (without any signal gradients), but the interaction between the two creates heterogeneity in both, which crucially enables persistent, directed migration of the cell population.

In Chapter 5 we turned to a different biological system – the formation of mouse skin in culture – to explore the effect of cell-cell interactions on tissue self-organisation in the absence of any external signals. By comparing epidermal cell cluster size counts with solutions to the Smoluchowski coagulation equations, and by characterising the dynamic scaling of these distributions, we showed the first 36 hours of skin reconstitution can be accounted for by a simple aggregation process. By finding where this description eventually breaks down, we provided evidence for a change in dynamics, apparently resulting in size regulation of the cell aggregates. The nature of this regulatory mechanism remains the topic of current biological investigation.

We explored one hypothesis for such size regulation, namely interaction of epidermal aggregates with dermal cells through volume exclusion. This was the topic of Chapter 6. By modifying the aggregation kernels with existing predictions on the

effect of crowding in binary particle mixtures, we proposed a model in which aggregation is arrested through the trapping of large clusters by inert monomers. This qualitatively produced the desired cluster size control, but failed to quantitatively capture both the early and late stage dynamics of epidermal cluster size distributions. This provided evidence that other biological mechanisms must be at play in the self-organisation of mouse skin, and resulted in a new class of aggregation models with other possible applications.

7.2 Open questions and future work

In this thesis we have addressed a number of open problems in biological applications, in close collaboration with experiments to ensure relevance of our results. For the problems we investigated, we achieved as much as we could given the current state of experimental data. Open questions remain, with future work that is outside the scope of this thesis, either because it requires substantial model development or improved quantity and quality of experimental data. Here, we highlight some of the most exciting questions and future projects that were not addressed in this thesis.

7.2.1 Collective cell migration

Advances in our understanding of the mechanisms of collective neural crest cell migration are likely to come from testing the universality of current hypotheses across different axial locations in the body and different model organisms. Specifically, cell interactions seem to range from contact inhibition of locomotion to contact guidance, and we need to understand how this is determined by cell density, microenvironmental properties and the dimensionality of the system. In some species, cell-produced chemokines that facilitate cohesion have been identified (Carmona-Fontaine *et al.*, 2011), while in other systems alternative mechanisms include communication of directional signals through cytoplasmic transfer (McKinney *et al.*, 2011) and trails of breadcrumb-like chemokine deposits (Lim *et al.*, 2015), while modifications of ECM structure to guide trailing cells may also be important (Chauviere *et al.*, 2010). Here, mathematical and computational models have a proven track record of adding to our understanding of the biological systems, but they need to be more strongly constrained by experimental data if we are to increase their complexity to span the range of currently debated hypotheses.

One possible modification of our existing model would be to change the stochastic movement implementation in order to probe the different effects of volume exclusion

with contact guidance vs CiL with CoA (as discussed in Section 2.1.2.3). Instead of sampling a discrete number of directions, in which the cells sense for the presence of a chemoattractant gradient or other cells to decide whether to move, the direction of movement could be sampled from a non-uniform circular distribution, that is biased towards directions of increasing chemoattractant, as well as towards cells within the sensing radius, while excluding directions that would lead to overlap of cell bodies (depending on the type of volume exclusion that is assumed). A similar approach has been taken recently by Irons *et al.* (2016) to construct agent-based lattice-free models of cell migration with chemotaxis and their corresponding continuum models. This is less biologically realistic than filopodial sensing, but may allow more general deductions to be made. If continuum models are derived, however, the correct limits for non-local sensing (taking the limit of cell size and sensing distance independently, as pointed out by Dyson, 2013) remains a technical difficulty that would require modification of the approach by Irons *et al.* (2016). In addition, moment-based techniques may have to be employed to accurately capture pair correlations (Markham *et al.*, 2013, Binny *et al.*, 2015). Another, reversed, form of contact guidance, from follower to leader, is when a cell induces a cell it comes into contact with to move away, an interaction also known as "pushing"(Yates *et al.*, 2015). This can be thought of as an asymmetric form of CiL, that may be more appropriate for the study of chick cranial neural crest migration based on experimental observations. Mathematical models could investigate the effect of contact guidance vs pushing in collective cell migration to shed light on the direction of communication between chick cranial neural crest cells.

Recent work has also revisited the fundamental limits in cellular sensing accuracy to investigate the effects of cell-cell communication (Mugler *et al.*, 2016). This is highly relevant in the context of chick cranial neural crest cell migration, where the mechanism of propagation of directional signals remains hypothetical. Extending the approach of Mugler *et al.* (2016), which includes reporter molecules that are exchanged between cells, to (1) the case of moving groups of cells and (2) situations where only a subset of the population are sensing may give us concrete bounds that potential mechanisms of neural crest cell communication have to obey.

To date, most computational and *in vitro* models of collective cell migration have been two-dimensional. While this is probably sufficient for most studies of epithelia, it may be limiting our understanding of how cell-cell communication and emergent migratory phenotypes depend on the dimensionality of the system. Extensions to canonical models of collective motion compared with three-dimensional culture assays

(Sharma *et al.*, 2015) are currently being developed, and show promise of rectifying the prevalent two-dimensional view of collective cell migration. For applications in developmental biology, however, the *in vivo* quantification of three-dimensional domain geometry, signal distribution, and cell-cell interactions still needs to continue to progress before we can usefully compare experimental observations with the predictions of three-dimensional mathematical models.

7.2.2 Tissue self-organisation

In the self-organised reconstitution of mouse skin, an intriguing question remains: Why do cells undergo a seemingly complex trajectory of different morphological stages on the way to a relatively simple phase separated state? Is this because it is the lowest energy path through tissue phase space, or a side effect of beginning the formation of functional hair-producing structures (for which some mechanisms are already understood; see Jiang *et al.*, 1999, Sick *et al.*, 2006, Baker *et al.*, 2008, Chuong *et al.*, 2013) during the phase separation process? Key factors that drive the transitions between different dynamical stages need to be further characterised to address this. Molecular changes have begun to be identified, but need to be verified in functional perturbations, and here models may aid in the interpretation of counterintuitive experimental outcomes. An alternative mechanism for size control of mixed cell aggregates has been proposed in the formation of enteric ganglia (Rollo *et al.*, 2015), excitingly tying together our study of aggregation process with neural crest biology.

Finally, let us conclude by expressing that we hope to have not only contributed to the understanding of collective cell behaviour in developmental biology and tissue engineering, but also advanced the case for this particular flavour of experiment-focussed, outcome-oriented theoretical biology.

References

Akima, H. 1970. A new method of interpolation and smooth curve fitting based on local procedures. *Journal of the Association for Computing Machinery*, **17**, 589–602. doi:10.1145/321607.321609.

Alarcón, T. and Page, K. M. 2007. Mathematical models of the VEGF receptor and its role in cancer therapy. *Journal of The Royal Society Interface*, **4**, 283–304. doi:10.1098/rsif.2006.0170.

Alarcón, T. and Page, K. M. Mathematical Modeling of the VEGF Receptor. In *Modeling Tumor Vasculature*, 3–35. 2012. ISBN 978-1-4614-0051-6.

Baker, R. E., Gaffney, E. A. and Maini, P. K. 2008. Partial differential equations for self-organization in cellular and developmental biology. *Nonlinearity*, **21**, R251–R290. doi:10.1088/0951-7715/21/11/R05.

Baker, R. E. and Simpson, M. J. 2015. Quantifying transport in crowded biochemical environments. *bioRxiv*. doi:10.1101/014704.

Benish, B. M. 1975. The neurocristopathies: a unifying concept of disease arising in neural crest maldevelopment. *Human pathology*, **6**, 128.

Berg, H. C. and Purcell, E. M. 1977. Physics of chemoreception. *Biophysical Journal*, **20**, 193–219. doi:10.1016/S0006-3495(77)85544-6.

Bhattacharjee, S. M. and Seno, F. 2001. A measure of data collapse for scaling. *Journal of Physics A: Mathematical and General*, **34**, 6375–6380. doi:10.1088/0305-4470/34/33/302.

Binny, R. N., Plank, M. J. and James, A. 2015. Spatial moment dynamics for collective cell movement incorporating a neighbour-dependent directional bias. *Journal of the Royal Society, Interface*, **12**, 20150228.

Botet, R. and Jullien, R. 1984. Size distribution of clusters in irreversible kinetic aggregation. *Journal of Physics A: Mathematical and General*, **17**, 2517–2530.

Box, G. E. P. 1976. Science and Statistics. *Journal of the American Statistical Association*, **71**, 791–799. doi:10.1641/B570910.

Brodland, G. W. 2002. The Differential Interfacial Tension Hypothesis (DITH): A comprehensive theory for the self-rearrangement of embryonic cells and tissues. *Journal of Biomechanical Engineering*, **124**, 188. doi:10.1115/1.1449491.

Bruna, M. and Chapman, S. J. 2012a. Diffusion of multiple species with excluded-volume effects. *Journal of Chemical Physics*, **137**. doi:10.1063/1.4767058.

Bruna, M. and Chapman, S. J. 2012b. Excluded-volume effects in the diffusion of hard spheres. *Physical Review E*, **85**, 24–29. doi:10.1103/PhysRevE.85.011103.

Bruna, M. and Chapman, S. J. 2015. Diffusion in spatially varying porous media. *arXiv*, 1501.06549.

Carmona-Fontaine, C., Matthews, H. K., Kuriyama, S., Moreno, M., Dunn, G. A., Parsons, M., Stern, C. D. and Mayor, R. 2008. Contact inhibition of locomotion in vivo controls neural crest directional migration. *Nature*, **456**, 957–61. doi:10.1038/nature07441.

Carmona-Fontaine, C., Theveneau, E., Tzekou, A., Tada, M., Woods, M., Page, K. M., Parsons, M., Lambris, J. D. and Mayor, R. 2011. Complement fragment C3a controls mutual cell attraction during collective cell migration. *Developmental Cell*, **21**, 1026–37. doi:10.1016/j.devcel.2011.10.012.

Chauviere, A., Preziosi, L. and Byrne, H. 2010. A model of cell migration within the extracellular matrix based on a phenotypic switching mechanism. *Mathematical Medicine and Biology*, **27**, 255–281. doi:10.1093/imammb/dqp021.

Cheeseman, B. L., Zhang, D., Binder, B. J., Newgreen, D. F. and Landman, K. A. 2014. Cell lineage tracing in the developing enteric nervous system: superstars revealed by experiment and simulation. *Journal of The Royal Society Interface*, **11**, 20130815–20130815. doi:10.1098/rsif.2013.0815.

Chuong, C.-M., Yeh, C.-Y., Jiang, T.-X. and Widelitz, R. 2013. Module-based complexity formation: periodic patterning in feathers and hairs. *Wiley Interdisciplinary Reviews. Developmental Biology*, **2**, 97–112. doi:10.1002/wdev.74.

Clauset, A., Shalizi, C. R. and Newman, M. E. J. 2009. Power-Law Distributions in Empirical Data. *SIAM Review*, **51**, 661–703. doi:10.1137/070710111.

Clayton, E., Doupé, D. P., Klein, A. M., Winton, D. J., Simons, B. D. and Jones, P. H. 2007. A single type of progenitor cell maintains normal epidermis. *Nature*, **446**, 185–9. doi:10.1038/nature05574.

Couzin, I. D., Krause, J., Franks, N. R. and Levin, S. A. 2005. Effective leadership and decision-making in animal groups on the move. *Nature*, **433**, 513–6. doi:10.1038/nature03236.

Cremer, P. and Löwen, H. 2014. Scaling of cluster growth for coagulating active particles. *Physical Review E*, **89**, 022307. doi:10.1103/PhysRevE.89.022307.

Dalle Nogare, D., Somers, K., Rao, S., Matsuda, M., Reichman-Fried, M., Raz, E. and Chitnis, A. B. 2014. Leading and trailing cells cooperate in collective migration of the zebrafish posterior lateral line primordium. *Development*, **141**, 3188–3196. doi:10.1242/dev.106690.

Davis, J. R., Huang, C.-Y., Zanet, J., Harrison, S., Rosten, E., Cox, S., Soong, D. Y., Dunn, G. A. and Stramer, B. M. 2012. Emergence of embryonic pattern through contact inhibition of locomotion. *Development*, **139**, 4555–60. doi:10.1242/dev.082248.

Donà, E., Barry, J. D., Valentin, G., Quirin, C., Khmelinskii, A., Kunze, A., Durdu, S., Newton, L. R., Fernandez-Minan, A., Huber, W., Knop, M. and Gilmour, D. 2013. Directional tissue migration through a self-generated chemokine gradient. *Nature*, **503**, 285–289. doi:10.1038/nature12635.

Dumortier, J. G., Martin, S., Meyer, D., Rosa, F. M. and David, N. B. 2012. Collective mesendoderm migration relies on an intrinsic directionality signal transmitted through cell contacts. *Proceedings of the National Academy of Sciences*, **109**. doi:10.1073/pnas.1205870109.

Dusenbery, D. B. 1987. Theoretical range over which bacteria and nematodeslocate plant roots using carbon dioxide. *Journal of Chemical Ecology*, **13**, 1617–1624.

Dyson, L. *Models of Cranial Neural Crest Cell Migration.* PhD thesis, University of Oxford, 2013.

Dyson, L. and Baker, R. E. 2015. The importance of volume exclusion in modelling cellular migration. *Journal of Mathematical Biology*, **71**, 691–711. doi:10.1007/s00285-014-0829-0.

Dyson, L., Maini, P. K. and Baker, R. E. 2012. Macroscopic limits of individual-based models for motile cell populations with volume exclusion. *Physical Review E*, **86**, 031903. doi:10.1103/PhysRevE.86.031903.

Eichmann, A. and Simons, M. 2012. VEGF signaling inside vascular endothelial cells and beyond. *Current Opinion in Cell Biology*, **24**, 188–93. doi:10.1016/j.ceb.2012.02.002.

Einstein, A. 1905. Über die von der molekularkinetischen Theorie der Wärme geforderte Bewegung von in ruhenden Flüssigkeiten suspendierten Teilchen. *Annalen der Physik*, **322**, 549–560. doi:10.1002/andp.19053220806.

Ellery, A. J., Simpson, M. J., McCue, S. W. and Baker, R. E. 2014. Characterizing transport through a crowded environment with different obstacle sizes. *Journal of Chemical Physics*, **140**. doi:10.1063/1.4864000.

Endres, R. G. and Wingreen, N. S. 2008. Accuracy of direct gradient sensing by single cells. *Proceedings of the National Academy of Sciences*, **105**, 15749–54. doi:10.1073/pnas.0804688105.

Freter, S., Fleenor, S. J., Freter, R., Liu, K. J. and Begbie, J. 2013. Cranial neural crest cells form corridors prefiguring sensory neuroblast migration. *Development*, **140**, 3595–600. doi:10.1242/dev.091033.

Friedl, P. 2004. Prespecification and plasticity: shifting mechanisms of cell migration. *Current Opinion in Cell Biology*, **16**, 14–23. doi:10.1016/j.ceb.2003.11.001.

Friedl, P., Locker, J., Sahai, E. and Segall, J. E. 2012. Classifying collective cancer cell invasion. *Nature Cell Biology*, **14**, 777–783. doi:10.1038/ncb2548.

Gjorevski, N., Ranga, A. and Lutolf, M. P. 2014. Bioengineering approaches to guide stem cell-based organogenesis. *Development*, **141**, 1794–804. doi:10.1242/dev.101048.

Goodhill, G. J. and Urbach, J. S. 1999. Theoretical analysis of gradient detection by growth cones. *Journal of Neurobiology*, **41**, 230–241.

Goodisman, J. and Chaiken, J. 2006. Scaling and the Smoluchowski equations. *Journal of Chemical Physics*, **125**, 074304. doi:10.1063/1.2218836.

Haeger, A., Wolf, K., Zegers, M. M. and Friedl, P. 2015. Collective cell migration: guidance principles and hierarchies. *Trends in Cell Biology*, **25**, 556–566. doi:10.1016/j.tcb.2015.06.003.

Hall, B. K. 2000. The neural crest as a fourth germ layer and vertebrates as quadroblastic not triploblastic. *Evolution and Development*, **2**, 3–5. doi:10.1046/j.1525-142X.2000.00032.x.

Hamburger, V. and Hamilton, H. L. 1951. A series of normal stages in the development of the chick embryo. *Journal of Morphology*, **88**, 49–92. doi:10.1002/jmor.1050880104.

Havlickova, B., Bíró, T., Mescalchin, A., Tschirschmann, M., Mollenkopf, H., Bettermann, A., Pertile, P., Lauster, R., Bodó, E. and Paus, R. 2009. A human folliculoid microsphere assay for exploring epithelial-mesenchymal interactions in the human hair follicle. *Journal of Investigative Dermatology*, **129**, 972–983. doi:10.1038/jid.2008.315.

Hellemans, J., Mortier, G., De Paepe, A., Speleman, F. and Vandesompele, J. 2007. qBase relative quantification framework and software for management and automated analysis of real-time quantitative PCR data. *Genome Biology*, **8**, R19. doi:10.1186/gb-2007-8-2-r19.

Hendrix, M. J. C., Seftor, E. A., Seftor, R. E. B., Kasemeier-Kulesa, J. C., Kulesa, P. M. and Postovit, L.-M. 2007. Reprogramming metastatic tumour cells with embryonic microenvironments. *Nature Reviews Cancer*, **7**, 246–55. doi:10.1038/nrc2108.

Inaki, M., Vishnu, S., Cliffe, A. and Rørth, P. 2012. Effective guidance of collective migration based on differences in cell states. *Proceedings of the National Academy of Sciences*, **109**, 2027–32. doi:10.1073/pnas.1115260109.

Irons, C., Plank, M. J. and Simpson, M. J. 2016. Lattice-free models of directed cell motility. *Physica A: Statistical Mechanics and its Applications*, **442**, 110–121. doi:10.1016/j.physa.2015.08.049.

Iyer-Biswas, S., Crooks, G. E., Scherer, N. F. and Dinner, A. R. 2014. Universality in stochastic exponential growth. *Physical Review Letters*, **113**, 028101. doi:10.1103/PhysRevLett.113.028101.

Jain, H. V. and Jackson, T. L. 2013. A hybrid model of the role of VEGF binding in endothelial cell migration and capillary formation. *Frontiers in Oncology*, **3**, 102. doi:10.3389/fonc.2013.00102.

Jiang, T.-X., Jung, H. S., Widelitz, R. B. and Chuong, C.-M. 1999. Self-organization of periodic patterns by dissociated feather mesenchymal cells and the regulation of size, number and spacing of primordia. *Development*, **126**, 4997–5009.

Jiang, Y. and Leyvraz, F. 1994. Kinetic properties of ballistic aggregation. *Physical Review E*, **50**, 2148–2155.

Jury, S. I., Bladon, P., Krishna, S. and Cates, M. E. 1999. Tests of dynamical scaling in three-dimensional spinodal decomposition. *Physical Review E*, **59**, R2535–R2538. doi:10.1103/PhysRevE.59.R2535.

Kaizu, K., de Ronde, W., Paijmans, J., Takahashi, K., Tostevin, F. and ten Wolde, P. R. 2014. The Berg-Purcell limit revisited. *Biophysical Journal*, **106**, 976–985. doi:10.1016/j.bpj.2013.12.030.

Kandel, D. 1997. Selection of the scaling solution in a cluster coalescence model. *Physical Review Letters*, **79**, 4238–4241. doi:10.1103/PhysRevLett.79.4238.

Kasemeier-Kulesa, J. C., Morrison, J. A., Lefcort, F. and Kulesa, P. M. 2015. TrkB/BDNF signalling patterns the sympathetic nervous system. *Nature Communications*, **6**, 8281. doi:10.1038/ncomms9281.

Kasemeier-Kulesa, J. C., Teddy, J. M., Postovit, L.-M., Seftor, E. A., Seftor, R. E. B., Hendrix, M. J. C. and Kulesa, P. M. 2008. Reprogramming multipotent tumor cells with the embryonic neural crest microenvironment. *Developmental Dynamics*, **237**, 2657–66. doi:10.1002/dvdy.21613.

Keller, E. F. and Segel, L. A. 1970a. Conflict between Positive and Negative Feedback as an Explanation for the Initiation of Aggregation in Slime Mould Amoebae. *Nature*, **227**, 1365–1366. doi:10.1038/2271365a0.

Keller, E. F. and Segel, L. A. 1970b. Initiation of slime mold aggregation viewed as an instability. *Journal of Theoretical Biology*, **26**, 399–415. doi:10.1016/0022-5193(70)90092-5.

Keller, E. F. and Segel, L. A. 1971a. Model for chemotaxis. *Journal of Theoretical Biology*, **30**, 225–234. doi:10.1016/0022-5193(71)90050-6.

Keller, E. F. and Segel, L. A. 1971b. Traveling bands of chemotactic bacteria: A theoretical analysis. *Journal of Theoretical Biology*, **30**, 235–248. doi:10.1016/0022-5193(71)90051-8.

Khalil, A. A. and Friedl, P. 2010. Determinants of leader cells in collective cell migration. *Integrative Biology*, **2**, 568–74. doi:10.1039/c0ib00052c.

Klein, A. M., Mazutis, L., Akartuna, I., Tallapragada, N., Veres, A., Li, V., Peshkin, L., Weitz, D. A. and Kirschner, M. W. 2015. Droplet barcoding for single-cell transcriptomics applied to embryonic stem cells. *Cell*, **161**, 1187–1201. doi:10.1016/j.cell.2015.04.044.

Koch, S., van Meeteren, L. a., Morin, E., Testini, C., Weström, S., Björkelund, H., Le Jan, S., Adler, J., Berger, P. and Claesson-Welsh, L. 2014. NRP1 presented in trans to the endothelium arrests VEGFR2 endocytosis, preventing angiogenic signaling and tumor initiation. *Developmental Cell*, **28**, 633–46. doi:10.1016/j.devcel.2014.02.010.

Kolb, M. 1984. Unified description of static and dynamic scaling for kinetic cluster formation. *Physical Review Letters*, **53**, 1653–1656.

Krapivsky, P. L., Redner, S. and Ben-Naim, E., 2013. *A kinetic view of statistical physics*. Cambridge University Press. ISBN 9780521851039.

Kulesa, P. M., Bailey, C. M., Kasemeier-Kulesa, J. C. and McLennan, R. 2010. Cranial neural crest migration: new rules for an old road. *Developmental Biology*, **344**, 543–54. doi:10.1016/j.ydbio.2010.04.010.

Kulesa, P. M., Ellies, D. L. and Trainor, P. A. 2004. Comparative analysis of neural crest cell death, migration, and function during vertebrate embryogenesis. *Developmental Dynamics*, **229**, 14–29. doi:10.1002/dvdy.10485.

Kulesa, P. M. and Fraser, S. E. 1998. Neural crest cell dynamics revealed by time-lapse video microscopy of whole embryo chick explant cultures. *Developmental Biology*, **204**, 327–44. doi:10.1006/dbio.1998.9082.

Kulesa, P. M., Kasemeier-Kulesa, J. C., Teddy, J. M., Margaryan, N. V., Seftor, E. A., Seftor, R. E. B. and Hendrix, M. J. C. 2006. Reprogramming metastatic melanoma cells to assume a neural crest cell-like phenotype in an embryonic microenvironment. *Proceedings of the National Academy of Sciences*, **103**, 3752–7. doi:10.1073/pnas.0506977103.

Kulesa, P. M. and McLennan, R. 2015. Neural crest migration: trailblazing ahead. *F1000Prime Reports*, **7**, 1–7. doi:10.12703/P7-02.

Kulesa, P. M., Teddy, J. M., Stark, D. A., Smith, S. E. and McLennan, R. 2008. Neural crest invasion is a spatially-ordered progression into the head with higher cell proliferation at the migratory front as revealed by the photoactivatable protein, KikGR. *Developmental Biology*, **316**, 275–87. doi:10.1016/j.ydbio.2008.01.029.

Laloux, L., Cizeau, P., Bouchaud, J.-P. and Potters, M. 1999. Noise dressing of financial correlation matrices. *Physical Review Letters*, **83**, 1467–1470. doi:10.1103/PhysRevLett.83.1467.

Landman, K. A., Fernando, A. E., Zhang, D. and Newgreen, D. F. 2011. Building stable chains with motile agents: Insights into the morphology of enteric neural crest cell migration. *Journal of Theoretical Biology*, **276**, 250–68. doi:10.1016/j.jtbi.2011.01.043.

Lee, L. F. and Chuong, C.-M. 2009. Building complex tissues: High-throughput screening for molecules required in hair engineering. *Journal of Investigative Dermatology*, **129**, 815–817. doi:10.1038/jid.2008.434.

Lee, L. F., Jiang, T. X., Garner, W. and Chuong, C.-M. 2011. A simplified procedure to reconstitute hair-producing skin. *Tissue Engineering Part C: Methods*, **17**, 391–400. doi:10.1089/ten.tec.2010.0477.

Lee, R. T. H., Nagai, H., Nakaya, Y., Sheng, G., Trainor, P. A., Weston, J. A. and Thiery, J. P. 2013. Cell delamination in the mesencephalic neural fold and its implication for the origin of ectomesenchyme. *Development*, **140**, 4890–4902. doi:10.1242/dev.094680.

Lee, Y. S., Stott, N. S., Jiang, T. X., Widelitz, R. B. and Chuong, C. M. 1998. Early events during precartilage condensation in limb bud micromass cultures. *Cells and Materials*, **8**, 19–32.

Leyvraz, F. 2003. Scaling theory and exactly solved models in the kinetics of irreversible aggregation. *Physics Reports*, **383**, 95–212. doi:10.1016/S0370-1573(03)00241-2.

Lim, K., Hyun, Y.-M., Lambert-Emo, K., Capece, T., Bae, S., Miller, R., Topham, D. J. and Kim, M. 2015. Neutrophil trails guide influenza-specific CD8+ T cells in the airways. *Science*, **349**. doi:10.1126/science.aaa4352.

Linnemann, J. R., Miura, H., Meixner, L. K., Irmler, M., Kloos, U. J., Hirschi, B., Bartsch, H. S., Sass, S., Beckers, J., Theis, F. J., Gabka, C., Sotlar, K. and Scheel, C. H. 2015. Quantification of regenerative potential in primary human mammary epithelial cells. *Development*, **142**, 1–13. doi:10.1242/dev.123554.

Lo, A. and Skodje, R. T. 2000. Kinetic and Monte Carlo models of thin film coarsening: Cross over from diffusion-coalescence to Ostwald growth modes. *Journal of Chemical Physics*, **112**, 1966. doi:10.1063/1.480756.

Mac Gabhann, F., Ji, J. W. and Popel, A. S. 2006. Computational model of vascular endothelial growth factor spatial distribution in muscle and pro-angiogenic cell therapy. *PLOS Computational Biology*, **2**, e127. doi:10.1371/journal.pcbi.0020127.

Mac Gabhann, F. and Popel, A. S. 2005. Differential binding of VEGF isoforms to VEGF receptor 2 in the presence of neuropilin-1: a computational model. *American Journal of Physiology. Heart and Circulatory Physiology*, **288**, H2851–60. doi:10.1152/ajpheart.01218.2004.

Markham, D. C., Simpson, M. J., Maini, P. K., Gaffney, E. A. and Baker, R. E. 2013. Incorporating spatial correlations into multispecies mean-field models. *Physical Review E*, **88**, 052713. doi:10.1103/PhysRevE.88.052713.

Mattsson, T. R., Mills, G. and Metiu, H. 1999. A new method for simulating the late stages of island coarsening in thin film growth: The role of island diffusion and evaporation. *Journal of Chemical Physics*, **110**, 12151. doi:10.1063/1.479152.

McKinney, M. C., Fukatsu, K., Morrison, J., McLennan, R., Bronner, M. E. and Kulesa, P. M. 2013. Evidence for dynamic rearrangements but lack of fate or

position restrictions in premigratory avian trunk neural crest. *Development*, **140**, 820–30. doi:10.1242/dev.083725.

McKinney, M. C., Stark, D. A., Teddy, J. M. and Kulesa, P. M. 2011. Neural crest cell communication involves an exchange of cytoplasmic material through cellular bridges revealed by photoconversion of KikGR. *Developmental Dynamics*, **240**, 1391–401. doi:10.1002/dvdy.22612.

McLennan, R., Dyson, L., Prather, K. W., Morrison, J. A., Baker, R. E., Maini, P. K. and Kulesa, P. M. 2012. Multiscale mechanisms of cell migration during development: theory and experiment. *Development*, **139**, 2935–44. doi:10.1242/dev.081471.

McLennan, R. and Kulesa, P. M. 2007. In vivo analysis reveals a critical role for neuropilin-1 in cranial neural crest cell migration in chick. *Developmental Biology*, **301**, 227–39. doi:10.1016/j.ydbio.2006.08.019.

McLennan, R. and Kulesa, P. M. 2010. Neuropilin-1 interacts with the second branchial arch microenvironment to mediate chick neural crest cell dynamics. *Developmental Dynamics*, **239**, 1664–73. doi:10.1002/dvdy.22303.

McLennan, R., Schumacher, L. J., Morrison, J. A., Teddy, J. M., Ridenour, D. A., Box, A. C., Semerad, C. L., Li, H., McDowell, W., Kay, D., Maini, P. K., Baker, R. E. and Kulesa, P. M. 2015a. Neural crest migration is driven by a few trailblazer cells with a unique molecular signature narrowly confined to the invasive front. *Development*, **142**, 2014–2025. doi:10.1242/dev.117507.

McLennan, R., Schumacher, L. J., Morrison, J. A., Teddy, J. M., Ridenour, D. A., Box, A. C., Semerad, C. L., Li, H., McDowell, W., Kay, D., Maini, P. K., Baker, R. E. and Kulesa, P. M. 2015b. VEGF signals induce trailblazer cell identity that drives neural crest migration. *Developmental Biology*, **407**, 12–25. doi:10.1016/j.ydbio.2015.08.011.

McLennan, R., Teddy, J. M., Kasemeier-Kulesa, J. C., Romine, M. H. and Kulesa, P. M. 2010. Vascular endothelial growth factor (VEGF) regulates cranial neural crest migration in vivo. *Developmental Biology*, **339**, 114–125. doi:10.1016/j.ydbio.2009.12.022.

Meakin, P. 1990. Diffusion-limited droplet coalescence. *Physica A: Statistical Mechanics and its Applications*, **165**, 1–18. doi:10.1016/0378-4371(90)90238-N.

Meakin, P., Vicsek, T. and Family, F. 1985. Dynamic cluster-size distribution in cluster-cluster aggregation: Effects of cluster diffusivity. *Physical Review B*, **31**, 564–569.

Mugler, A., Levchenko, A. and Nemenman, I. 2016. Limits to the precision of gradient sensing with spatial communication and temporal integration. *Proceedings of the National Academy of Sciences*, **113**, E689–E695. doi:10.1073/pnas.1509597112.

Muinonen-Martin, A. J., Susanto, O., Zhang, Q., Smethurst, E., Faller, W. J., Veltman, D. M., Kalna, G., Lindsay, C., Bennett, D. C., Sansom, O. J., Herd, R., Jones, R., Machesky, L. M., Wakelam, M. J. O., Knecht, D. a. and Insall, R. H. 2014. Melanoma cells break down LPA to establish local gradients that drive chemotactic dispersal. *PLOS Biology*, **12**, e1001966. doi:10.1371/journal.pbio.1001966.

Müller, P., Rogers, K. W., Yu, S. R., Brand, M. and Schier, A. F. 2013. Morphogen transport. *Development*, **140**, 1621–38. doi:10.1242/dev.083519.

Ódor, G. 2004. Universality classes in nonequilibrium lattice systems. *Reviews of Modern Physics*, **76**, 663–724. doi:10.1103/RevModPhys.76.663.

Odriozola, G., Schmitt, A., Callejas-Fernandez, J., Martinez-Garca, R. and Hidalgo-Alvarez, R. 1999. Dynamic scaling concepts applied to numerical solutions of Smoluchowski's rate equation. *The Journal of Chemical Physics*, **111**, 7657. doi:10.1063/1.480092.

Pearson, K. 1901. On lines and planes of closest fit to systems of points in space. *Philosophical Magazine Series 6*, **2**, 559–572. doi:10.1080/14786440109462720.

Plerou, V., Gopikrishnan, P., Rosenow, B., Amaral, L., Guhr, T. and Stanley, H. 2002. Random matrix approach to cross correlations in financial data. *Physical Review E*, **65**, 066126. doi:10.1103/PhysRevE.65.066126.

Pototsky, A., Thiele, U. and Archer, A. J. 2014. Coarsening modes of clusters of aggregating particles. *Physical Review E*, **89**, 032144. doi:10.1103/PhysRevE.89.032144.

Pryor, S. E., Massa, V., Savery, D., Andre, P., Yang, Y., Greene, N. D. E. and Copp, A. J. 2014. Vangl-dependent planar cell polarity signalling is not required for neural crest migration in mammals. *Development*, **141**, 3153–3158. doi:10.1242/dev.111427.

Redner, G. S., Baskaran, A. and Hagan, M. F. 2013. Reentrant phase behavior in active colloids with attraction. *Physical Review E*, **88**, 012305. doi:10.1103/PhysRevE.88.012305.

Revenu, C., Streichan, S. J., Donà, E., Lecaudey, V., Hufnagel, L. and Gilmour, D. 2014. Quantitative cell polarity imaging defines leader-to-follower transitions during collective migration and the key role of microtubule-dependent adherens junction formation. *Development*, **141**, 1282–1291. doi:10.1242/dev.101675.

Ridenour, D. A., McLennan, R., Teddy, J. M., Semerad, C. L., Haug, J. S. and Kulesa, P. M. 2014. The neural crest cell cycle is related to phases of migration in the head. *Development*, **141**, 1095–103. doi:10.1242/dev.098855.

Rogers, K. W. and Schier, A. F. 2011. Morphogen gradients: from generation to interpretation. *Annual Review of Cell and Developmental Biology*, **27**, 377–407. doi:10.1146/annurev-cellbio-092910-154148.

Rollo, B. N., Zhang, D., Simkin, J. E., Menheniott, T. R. and Newgreen, D. F. 2015. Why are enteric ganglia so small? Role of differential adhesion of enteric neurons and enteric neural crest cells. *F1000Research*, **113**. doi:10.12688/f1000research.6370.1.

Rørth, P. 2012. Fellow travellers: emergent properties of collective cell migration. *EMBO reports*, **13**, 984–991. doi:10.1038/embor.2012.149.

Rupp, P. A. and Kulesa, P. M. 2007. A role for RhoA in the two-phase migratory pattern of post-otic neural crest cells. *Developmental Biology*, **311**, 159–71. doi:10.1016/j.ydbio.2007.08.027.

Sasai, Y., Eiraku, M. and Suga, H. 2012. In vitro organogenesis in three dimensions: self-organising stem cells. *Development*, **139**, 4111–4121. doi:10.1242/dev.079590.

Séguis, J. C., Burrage, K., Erban, R. and Kay, D. 2012. Simulation of cell movement through evolving environment: a fictitious domain approach. *eprints.maths.ox.ac.uk*.

Sharma, Y., Vargas, D. A., Pegoraro, A. F., Lepzelter, D., Weitz, D. A. and Zaman, M. H. 2015. Collective motion of mammalian cell cohorts in 3D. *Integrative Biology*, **7**, 1526–1533. doi:10.1039/C5IB00208G.

Sholl, D. S. and Skodje, R. T. 1995. Diffusion of clusters of atoms and vacancies on surfaces and the dynamics of diffusion-driven coarsening. *Physical Review Letters*, **75**, 3158–3161.

Sick, S., Reinker, S., Timmer, J. and Schlake, T. 2006. WNT and DKK determine hair follicle spacing through a reaction-diffusion mechanism. *Science*, **314**, 1447–50. doi:10.1126/science.1130088.

Simons, M. 2012. An inside view: VEGF receptor trafficking and signaling. *Physiology*, **27**, 213–22. doi:10.1152/physiol.00016.2012.

Simpson, M. J., Zhang, D. C., Mariani, M., Landman, K. A. and Newgreen, D. F. 2007. Cell proliferation drives neural crest cell invasion of the intestine. *Developmental Biology*, **302**, 553–68. doi:10.1016/j.ydbio.2006.10.017.

Smadbeck, P. and Stumpf, M. P. 2015. Coalescent models for developmental biology and the spatio-temporal dynamics of growing tissues. *bioRxiv*. doi:10.1101/022251.

Smoluchowski, M. 1916. Three lectures on diffusion, Brownian movement and coagulation of colloidal particles. *Physikalische Zeitschrift*, **17**, 585–599.

Smoluchowski, M. 1917. Grundriß der Koagulationskinetik kolloider Lösungen. *Colloid & Polymer Science*, **1168**, 98–104.

Steinberg, M. S. 1962. On the mechanism of tissue reconstruction by dissociated cells, I. Population kinetics, differential adhesiveness, and the absence of directed migration. *Proceedings of the National Academy of Sciences*, **48**, 1577–1582.

Steinberg, M. S. 2007. Differential adhesion in morphogenesis: a modern view. *Current Opinion in Genetics & Development*, **17**, 281–6. doi:10.1016/j.gde.2007.05.002.

Stenhammar, J., Marenduzzo, D., Allen, R. J. and Cates, M. E. 2014. Phase behaviour of active Brownian particles: the role of dimensionality. *Soft matter*, **10**, 1489–99. doi:10.1039/c3sm52813h.

Streichan, S. J., Valentin, G., Gilmour, D. and Hufnagel, L. 2011. Collective cell migration guided by dynamically maintained gradients. *Physical Biology*, **8**, 045004. doi:10.1088/1478-3975/8/4/045004.

Stumpf, M. P. H. and Porter, M. A. 2012. Critical truths about power laws. *Science*, **335**, 665–6. doi:10.1126/science.1216142.

Sutherland, W. 1905. A dynamical theory of diffusion for non-electrolytes and the molecular mass of albumin. *Philosophical Magazine*, **9**, 781–785. doi:10.1080/14786440509463331.

Teddy, J. M. and Kulesa, P. M. 2004. In vivo evidence for short-and long-range cell communication in cranial neural crest cells. *Development*, **131**, 6141–51. doi:10.1242/dev.01534.

ten Wolde, P. R., Becker, N. B., Ouldridge, T. E. and Mugler, A. 2015. Fundamental Limits to Cellular Sensing. *arXiv*, 1505.06577.

Theveneau, E., Marchant, L., Kuriyama, S., Gull, M., Moepps, B., Parsons, M. and Mayor, R. 2010. Collective chemotaxis requires contact-dependent cell polarity. *Developmental Cell*, **19**, 39–53. doi:10.1016/j.devcel.2010.06.012.

Theveneau, E. and Mayor, R. 2011. Collective cell migration of the cephalic neural crest: The art of integrating information. *genesis*, **49**, 164–176. doi:10.1002/dvg.20700.

Theveneau, E., Steventon, B., Scarpa, E., Garcia, S., Trepat, X., Streit, A. and Mayor, R. 2013. Chase-and-run between adjacent cell populations promotes directional collective migration. *Nature Cell Biology*, **15**, 1–12. doi:10.1038/ncb2772.

Vempati, P., Popel, A. S. and Mac Gabhann, F. 2011. Formation of VEGF isoform-specific spatial distributions governing angiogenesis: computational analysis. *BMC Systems Biology*, **5**, 59. doi:10.1186/1752-0509-5-59.

Vicsek, T. and Family, F. 1984. Dynamic scaling for aggregation of clusters. *Physical Review Letters*, **52**, 1669–1672.

Vicsek, T. and Zafeiris, A. 2012. Collective motion. *Physics Reports*, **517**, 71–140. doi:10.1016/j.physrep.2012.03.004.

Visscher, W. 1973. Self-diffusion, the Green-Kubo formulas, and the long tail of the velocity-autocorrelation function. *Physical Review A*, **7**, 5–7.

Weber, S. N., Weber, C. a. and Frey, E. 2015. Binary mixtures of particles with different diffusivities demix. *arXiv*, 1505.00525.

Woods, M. L., Carmona-Fontaine, C., Barnes, C. P., Couzin, I. D., Mayor, R. and Page, K. M. 2014. Directional collective cell migration emerges as a property of cell interactions. *PLOS ONE*, **9**, e104969. doi:10.1371/journal.pone.0104969.

Wynn, M. L., Kulesa, P. M. and Schnell, S. 2012. Computational modelling of cell chain migration reveals mechanisms that sustain follow-the-leader behaviour. *Journal of the Royal Society, Interface*, **9**, 1576–88. doi:10.1098/rsif.2011.0726.

Wynn, M. L., Rupp, P., Trainor, P. A., Schnell, S. and Kulesa, P. M. 2013. Follow-the-leader cell migration requires biased cell-cell contact and local microenvironmental signals. *Physical Biology*, **10**, 035003. doi:10.1088/1478-3975/10/3/035003.

Yao, J. H., Elder, K. R., Guo, H. and Grant, M. 1992. Ostwald ripening in two and three dimensions. *Physical Review B*, **45**, 8173–8176. doi:10.1103/PhysRevB.45.8173.

Yates, C. A., Parker, A. and Baker, R. E. 2015. Incorporating pushing in exclusion-process models of cell migration. *Physical Review E*, **91**, 1–12. doi:10.1103/PhysRevE.91.052711.

Yen, P., Finley, S. D., Engel-Stefanini, M. O. and Popel, A. S. 2011. A two-compartment model of VEGF distribution in the mouse. *PLOS ONE*, **6**, e27514. doi:10.1371/journal.pone.0027514.

Yoon, C. and Kim, Y.-J. 2015. Bacterial chemotaxis without gradient-sensing. *Journal of Mathematical Biology*, **70**, 1359–1380. doi:10.1007/s00285-014-0790-y.

Young, H. M., Bergner, A. J., Simpson, M. J., McKeown, S. J., Hao, M. M., Anderson, C. R. and Enomoto, H. 2014. Colonizing while migrating: how do individual enteric neural crest cells behave? *BMC Biology*, **12**, 23. doi:10.1186/1741-7007-12-23.